

Dissertation submitted to the  
Combined Faculties for the Natural Sciences and Mathematics  
of the Ruperto-Carola University of Heidelberg, Germany  
for the Degree of Doctor of Natural Sciences

presented by

M.Sc. Paula González Avalos  
born in México City, México





Oral examination date:

25.01.2013

Referees:

Prof. Dr. Roland Eils

Prof. Dr. Harald Herrmann-Lerdon



*Para Amado,  
infinita fuente de inspiración, motivación y perseverancia.*

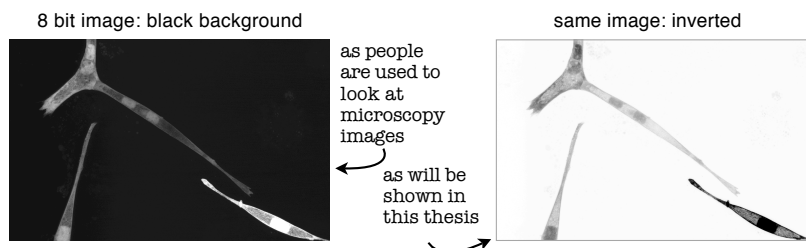
---

## **Collaborations and author contributions**

This work is the outcome of strong theoretical and experimental collaborations between scientists of different disciplines. Contributions from others are mentioned in the text and extra highlighted with a margin note at the relevant methods and results sections.

## **A note about the microscopy images**

Due to aesthetic and ink awareness reasons, all microscopy images are shown in a color inverted format with white background.





# Acknowledgements

I want to thank my *supervisors*: Prof. Roland Eils, for giving me the opportunity to work in his highly interdisciplinary group, having access to both technological resources and interesting creative minds; Dr. Evgeny Gladilin, for introducing me to the ups and downs of the cell mechanics field, for providing me with the numerical tools necessary to analyze my data and for giving me the freedom to work in my own ways; Dr. Michaela Reichenzeller, for bringing me by all the bases of the experimental work; Dr. Joel Beaudouin, for all the help with the microscopy, the support and guidance during the seminars and above all, for setting a real example on excellent scientific thinking; and my TAC members Prof. Dr. Harald Herrmann and Dr. Karsten Rippe, for their relevant yearly advice on the direction of the project. Many thanks also to the HBIGS graduate school, Corinna Sprengart, Karlheinz Groß and specially the amazing Manuela Schäfer, for all the *administrative and technical assistance*: vielen vielen Dank!

The second part of this project would not have been made possible without the help of my *collaboration partner* Marlies Mürnseer, with whom I performed all the hepatocyte stretching experiments, turning long microscopy nights into a valuable friendship. I also appreciate the help of my *lab colleagues*: Clarissa, Johanna, Stefan and Sabine for all the help in the lab and the advice in the seminars; Nina and Jürgen for coffee and siRNAs; and specially my *fellow voyager*, Martí, for stepping with me into interstellar space in the quest of awesomeness, discoveries and adventures beyond limits.

I also have to thank my *friends* for believing in me, standing by me and keeping me more or less sane during this intense time with coffees, dinners, parties, smoothies, E-mails, laughs and hugs. Some of you were here: Elena, Mónica, Marta, Aina, Mercedes, Silvana, Alejandro, Michael, Frauke; some kept close despite the distance: Flavia, Christian, Annette; some were everywhere as *bff*, thesis coach, co-hibernante and uwr teammate: Simone; some others even share my flat: Eva and Roman - so to all of you: thank you for being there. Also thanks to you, Renate, because regardless of the conditions - in calmed as in turbulent times - you kept on being the wind beneath my wings.

Last but not least, I want to thank my *family*: My brother, Ever, who's not only my main ally in life but also directly contributed to the finishing of this work by saving his sister in distress teaching her his powerful math and Matlab skills. And my parents, who have been strong (¡no seamos debiles!), kind, loving and supportive while her daughter is thousands of kilometers away fulfilling her crazy scientific ambitions: ¡Muchas gracias!



# Abstract

Cells and tissues are constantly exposed to mechanical forces. Understanding how these forces act on cells to regulate essential processes like development, differentiation, tissue homeostasis and how their alteration is related to disease requires the characterization of their mechanical properties. Several methods have been developed to study mechanical properties of cells and nuclei. However, most of the established methods are not compatible with culturing of cells in 3D substrates, a factor which plays an essential role in defining the structural and mechanical behavior of cells naturally existing in 3D environments. In this work, image and model based methods have been developed to approach this problem and enable the characterization of the cells mechanical phenotype in 3D.

On a first step, a previously developed method to measure the compressibility of the nuclear interior was enhanced to enable statistical significant measurements of nuclei to perform comparative analyses between phenotypes. Optimization of both the experimental, as well as the image processing methods led to a robust framework that served to measure an increase in nuclear compressibility in nuclei of LMNA<sup>-/-</sup> mouse embryonic fibroblasts. This study served as a proof of principle for this contact free method, which in a subsequent step was adapted to work for cells embedded in 3D substrates.

Aiming to develop a method, in which specific forces could be applied and relate to cellular deformations, the second part of this work was centered in the development of the 3D substrate stretcher. This involved identifying and implementing the needs of the experimental and image analysis framework to ensure the required environment for the cells, while at the same time enabling the acquisition of suitable data for the mechanical analysis. The resulting experimental and analysis framework enables for the first time application and quantification of strains on cells embedded in 3D substrates.

Motivation of the 3D-culture based methods was the analysis of epithelial-mesenchymal transition (EMT) in hepatocytes. These epithelial cells undergoing dedifferentiation upon treatment with TGF- $\beta$  serve not only as a preminent example of the need of 3D cell cultures in the characterization of mechanical properties, but also as a model of malignant transformation in fibrotic diseases and cancer. Quantification of previously unobserved morphological and structural properties led to the mechanical phenotyping of these cells, where a decrease in the compressibility of the nuclear interior, an enhanced resistance to deformation and a better anchorage of the nuclei inside the cells was observed after EMT.





# Zusammenfassung

Mechanische Kräfte spielen eine wichtige Rolle in vielen essentiellen zellulären Prozessen wie Entwicklung, Differenzierung oder Gewebemöostase. Um zu verstehen wie diese Kräfte regulatorisch wirken, muss man zelluläre und intrazelluläre mechanische Eigenschaften messen. Existierende Ansätze zur Ermittlung der mechanischen Eigenschaften der Zelle und des Zellkerns basieren oft auf direkter Kraftanwendung auf die zu untersuchenden Strukturen und sind deshalb nicht kompatibel mit der Kultivierung von Zellen in 3D-Substraten. Da die mechanische Umgebung der Zellen ein wichtiger Faktor in die Regulation von Mechanik und Struktur der Zelle ist, wurden in dieser Arbeit Bild- und Modell-basierte Methoden entwickelt, um mechanische Eigenschaften von Zellkernen und Zellen eingebettet in 3D-Substrate analysieren zu können.

In einem ersten Schritt wurde eine bereits existierende Methode zur Messung der Zellkernkompressibilität erweitert und optimiert, um statistisch signifikante vergleichende Studien zwischen Zellphänotypen durchführen zu können. Durch Verbesserungen experimenteller und bildverarbeitender Methoden wurde ein robustes Framework etabliert, mit dem eine Zunahme der Zellkernkompressibilität in  $LMNA^{-/-}$  Fibroblasten im Vergleich zu Wildtypzellen gemessen wurde. Da die kontaktfreie Methode auf Wirkstoff-induzierter Deformation der Zellkerne beruht, konnte sie auf die Arbeit mit Zellen in 3D-Substraten angepasst werden.

Mit dem Ziel eine Methode zu entwickeln, in der bekannte und kontrollierte Kräfte und Deformationen auf Zellen ausgeübt werden können und diese zu zellulären Deformationen in Beziehung zu setzen, wurde im zweiten Teil dieser Arbeit der 3D-Substrat-Stretcher entwickelt. Das neu entwickelte Experimental- und Analyse-Framework ermöglicht zum ersten Mal die Ausübung und Quantifizierung von Deformationen auf Zellen, die in einem 3D-Substrat eingebettet sind.

Ziel der 3D-Zellkultur-basierten Methoden war die mechanische Analyse von Epithelial-mesenchymale Transition in Hepatozyten. Diese epithelialen Zellen, die nach der Behandlung mit TGF-beta einen Dedifferenzierungsprozess durchlaufen, gelten als Modellsystem für die maligne Transformation in fibrotischen Erkrankungen und Krebs. Mit den entwickelten Tools wurden bisher unbeobachtete morphologische Eigenschaften quantifiziert, eine Verminderung der Kompressibilität des Zellkerninneren nach Dedifferenzierung gemessen und eine erhöhte Widerstandsfähigkeit gegen Deformation festgestellt.



# Contents

<b>Acknowledgements</b>	<b>iii</b>
<b>Abstract</b>	<b>v</b>
<b>Zusammenfassung</b>	<b>vii</b>
<b>Abbreviations</b>	<b>xiii</b>
<b>1 Introduction</b>	<b>1</b>
On the role of forces in cellular biology . . . . .	1
1.1 An introduction to mechanical properties . . . . .	3
1.1.1 Mechanical properties in biology . . . . .	3
1.1.2 Calculation of mechanical properties . . . . .	6
1.2 The cell's mechanical phenotype . . . . .	8
1.2.1 Structures defining cellular mechanics . . . . .	8
1.2.2 The cell's mechanical environment . . . . .	14
1.2.3 Altered mechanical properties in disease . . . . .	15
1.3 State of the art . . . . .	17
1.3.1 Approaches to measure cellular mechanical properties . . .	17
1.3.2 Experimental approaches to study nuclear mechanics . . . .	21
<b>Aim</b>	<b>25</b>
Aims and goals of this work . . . . .	25
<b>2 Methods</b>	<b>27</b>
2.1 Cell Culture . . . . .	28
2.2 Microscopy . . . . .	30
2.3 Nuclear rounding for Nuclear compressibility . . . . .	31
2.4 3D Substrate Stretcher . . . . .	32
2.5 Image processing pipelines . . . . .	33
2.6 Image and model based mechanical modeling . . . . .	38
2.6.1 Calculation of nuclear compressibility . . . . .	38

2.6.2	Calculation and description of strains in the 3D stretcher . .	40
2.7	Materials . . . . .	43
<b>3</b>	<b>Results</b>	<b>45</b>
3.1	Nuclear compressibility: optimization of the framework . . . . .	46
3.1.1	Reducing error sources with image processing . . . . .	48
3.1.2	Influence of the amount of image gradient in the calculation of $\nu$ . . . . .	49
3.1.3	Suboptimal geometry of the nuclear patterns . . . . .	49
3.1.4	Correct geometry of image gradients improves the calculation of $\nu$ . . . . .	51
3.1.5	Bleaching patterns on the nuclei improves accuracy . . . . .	51
3.1.6	Adapting the nuclear compressibility framework for 3D . .	53
3.2	The 3D substrate stretcher . . . . .	55
3.2.1	Going 3D . . . . .	56
3.2.2	Live 4D imaging in the 3D stretcher . . . . .	57
3.2.3	Cellular and nuclear surface reconstructions . . . . .	61
3.2.4	Description of 3D substrate deformation . . . . .	61
3.2.5	Mapping substrate strain on cellular structures . . . . .	67
3.2.6	Geometrical interpolation of cell and nucleus . . . . .	68
3.3	Mechanical phenotyping of wt vs. LMNA <sup>-/-</sup> MEFs . . . . .	70
3.3.1	No nuclear morphological differences . . . . .	71
3.3.2	Increase of nuclear compressibility in LMNA <sup>-/-</sup> MEFs . . .	71
3.3.3	No nuclear viscosity differences . . . . .	72
3.4	Mechanical phenotyping of hepatocyte EMT . . . . .	73
3.4.1	pmHCs need a 3D substrate to preserve epithelial polarity .	73
3.4.2	Changes in cellular and nuclear morphology in EMT . . . .	75
3.4.3	Changes in cytoskeleton organization in EMT . . . . .	75
3.4.4	Decrease of nuclear compressibility after EMT . . . . .	77
3.4.5	pmHC EMT on the 3D stretcher . . . . .	79
<b>4</b>	<b>Discussion</b>	<b>83</b>
4.1	On the methods developed & the cell mechanics field . . . . .	83
4.1.1	The Nuclear compressibility framework in context . . . . .	83
4.1.2	The 3D substrate stretcher framework in context . . . . .	84

---

4.1.3	Mechanical properties should be analyzed in 3D . . . . .	85
4.1.4	Image & model based methods enable measurements in 3D	87
4.1.5	Importance of the local characterization of substrate strain	88
4.1.6	"All models are wrong but some are useful" . . . . .	89
4.2	On the insight learned from the comparative studies . . . . .	90
4.2.1	Nuclear compressibility in LMNA mutants . . . . .	90
4.2.2	Differences in mechanical behavior in pmHC EMT . . . . .	92
	<b>Related publications</b>	<b>95</b>
	<b>References</b>	<b>96</b>
	<b>Appendix 1: Example of ImageJ Plugin</b>	<b>109</b>
	<b>Appendix 2: Examples of Matlab Scripts</b>	<b>115</b>
	<b>List of Figures</b>	<b>123</b>
	<b>List of Tables</b>	<b>125</b>



# Abbreviations

<b>2D</b>	Two-dimensional
<b>3D</b>	Three-dimensional
<b>AAV</b>	Adeno-associated virus
<b>AFM</b>	Atomic force microscopy
<b>BIN</b>	Ballistic injection nanorheology
<b>ECM</b>	Extracellular matrix
<b>EGFP</b>	Enhanced green fluorescent protein
<b>EMT</b>	Epithelial-mesenchymal transition
<b>FEM</b>	Finite element method
<b>FRAP</b>	Fluorescence recovery after photobleaching
<b>GFP</b>	Green fluorescent protein
<b>INM</b>	Inner nuclear membrane
<b>LINC</b>	Linkers of the nucleoskeleton to the cytoskeleton
<b>LMNA</b>	Lamin A/C gene
<b>LSCM</b>	Laser scanning confocal microscope
<b>MEF</b>	Mouse embryonic fibroblast
<b>ONM</b>	Outer nuclear membrane
<b>paGFP</b>	Photoactivatable green fluorescent protein
<b>pmHC</b>	Primary mouse hepatocyte
<b>TGF-<math>\beta</math></b>	Transforming growth factor $\beta$
<b>wt</b>	Wild type





# 1

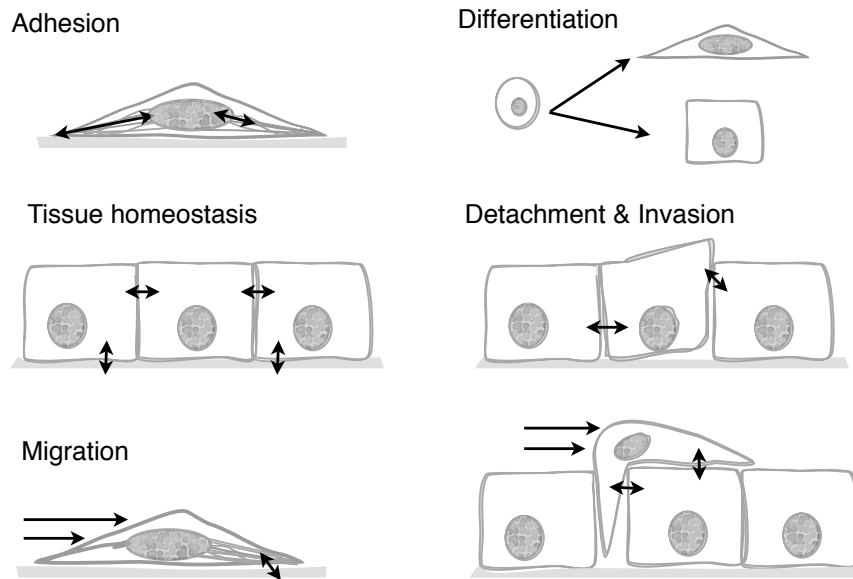
## Introduction

### On the role of forces in cellular biology

*"Every body persists in its state of being at rest or of moving uniformly straight forward, except insofar as it is compelled to change its state by force impressed." Sir Isaac Newton, 1687*

Newton's laws of motion defined the physics of classical mechanics describing the reaction of bodies towards forces. Over 300 years later we are just beginning to understand how mechanical forces affect and define essential biological processes at the cellular level.

Cells in organisms have developed and evolved to react to the forces constantly exhibited on them (**Fig. 1.1**). Starting with the formation of multicellular organisms, the mechanical environment of cells defines their behavior and fate during development [Chowdhury et al., 2009]. Matrix stiffness and force transduced through cell-to-cell contacts dictate stem cell fate [Engler et al., 2006]. During embryonic tissue formation, mechanical cues are as important as their biochemical and genetical counterparts in the process of structural remodeling that gives rise to multicellular structures with specialized forms and unique physical properties [Mammoto and Ingber, 2010]. Once the tissue is formed, mechanical forces keep control over cell orientation by restricting their axis of symmetry during division through physical deformation. Multicellular layers in tissues resist compressive, tensile and fluid shear stress through the formation of a mechanical continuum of cells enforced by tight cell to cell contacts [Asnacios and Hamant, 2012]. Interestingly, cells embedded in polarized 3D tissue structures are not only more resistant to mechanical forces but also to chemical perturbations [Dufort et al., 2011].



**Figure 1.1: Forces in cellular biology.** Mechanical forces (depicted here as black arrows) play an important role in regulating cellular structure and function. Even in apparent static processes like cell adhesion or tissue homeostasis, forces exerted into and between cells regulate their shape and orientation towards each other. During more obvious dynamical processes like migration, cells have to sense and exert force to their substrate in order to pull themselves forward. Mechanical properties of the extracellular matrix are key parameters defining stem cell fate and embryonic development and alterations in these properties are associated with malignant phenotypes.

Cells have different mechanical requirements depending on their biological functions: blood cells need to be able to resist shear stresses; bone and muscle cells have to provide a resistant mechanical scaffold for the body and to ensure movement; heart and lung cells have to cope with the constant movement of their compressive tissues. To be able to cope with these different mechanical environments, cells have developed specific mechanical properties through dynamic rearrangement of load-bearing intra cellular structures like the cytoskeleton and the nucleus in response to the external forces they sense [Hoffman et al., 2011].

Forces and the mechanical environment also play an important role during disease progression, where cells lack certain structural components or alter the mechanical properties of the extracellular matrix and intracellular structures losing the ability to cope with the requirements of the environment [Jaalouk and Lammending, 2009]. Arteriosclerosis [Cheng et al., 2006], osteoporosis [Klein-Nulend et al., 2003], asthma and lung dysfunction [Affonce and Lutchen, 2006], premature aging [Verstraeten et al., 2008] and cancer [Yu et al., 2011] are examples of

diseases associated with alterations of cellular mechanical properties and mechanotransduction.

The way in which cells sense and react to forces is defined by their mechanical properties. Because of their regulatory role and their alterations in disease, the characterization of cellular mechanical properties has become an interesting research target in general and the main topic of this thesis, in particular. The following introduction aims to give an understanding of the context and the current state of the art on which this work has been developed. Sec. 1.1 starts with the definition of common concepts used to measure the mechanical response of materials, with an emphasis in the dimension ranges of mechanical properties found in biological materials. Afterwards, sec. 1.2 outlines the factors related to defining the mechanical phenotype of a cell: the structures involved in defining them internally (sec. 1.2.1), how they are affected externally by the environment (sec. 1.2.2), and how they are found to be altered in disease (sec. 1.2.3). Finally, sec. 1.3.1 gives a critical overview of the approaches developed so far to measure cellular and nuclear mechanical properties, listing not only the measures achieved with them but also their advantages and shortcomings, leading directly to the aims of this work.

## 1.1 An introduction to mechanical properties

### 1.1.1 Mechanical properties in biology

Mechanical properties describe a material's reaction to force. When force is applied to a deformable object, mechanical properties are the parameters quantifying the way in which the geometry of the material changes or deforms in response to the applied force. There are several material properties relating different aspects of the deformation to the force applied. In general they either refer to:

- The **magnitude** of the deformation in response to a certain force e.g. *stiffness* for solid materials and *viscosity* for liquids.
- The specific **geometry** of the deformation e.g. *compressibility* as expressed by the Poisson's ratio.
- **Threshold** measures based on either the magnitude or the geometry and

put in respect to the material's limits e.g. ability to undergo irreversible deformations (*plasticity*), maximum stress a material can withstand (*strength*)

Canonical mechanical parameters describing the deformation of solid materials are stiffness and compressibility. In the case of fluids viscosity is the defining parameter.

### **Stiffness**

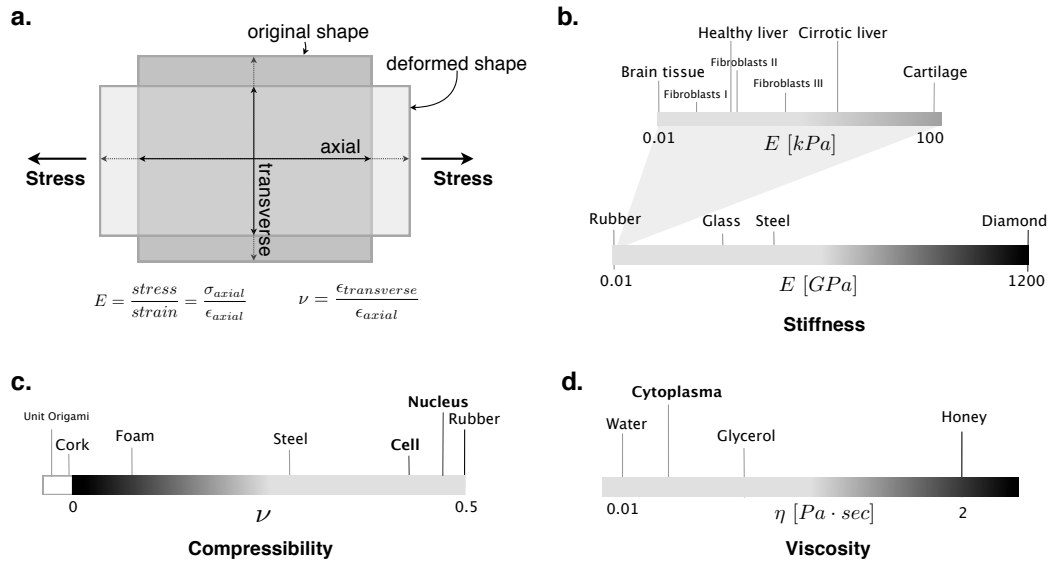
In practical terms, the stiffness of a material quantifies the magnitude of deformation (strain) i.e. the percentage of change in dimension in response to the applied force (stress). The Young's modulus ( $E$ ), also commonly called elastic modulus or modulus of elasticity, describes the material stiffness and can be defined as the ratio between *stress* (= the force per unit area) and *strain* (= the deformation of the object - a dimensionless quantity).

The Young's modulus is the most common of the elastic moduli, it describes the strain/stress relationship for the deformation along the axis at which the force is applied (**Fig. 1.2 a**). The shear modulus ( $\mu$ ) describes the same strain/stress relationship for shear stress and it is relevant in biology because it is part of the derivation of viscosity [Levental et al., 2006].

Stiffer materials deform less under the same applied force. Biological materials belong to the class of so called soft materials, that are easily deformed by thermal stresses or thermal fluctuations. The resistance of soft biological materials to deformation may be a hundred times less than hard materials, such as metals. Their elastic moduli range from on the order of 100 Pa for the softer brain tissue to 100 000 Pa for cartilage (**Fig. 1.2 b**) [Levental et al., 2006].

### **Viscosity**

Similar to stiffness, but for fluids, viscosity is a measure of the resistance of a fluid to deformation under stress. It can be interpreted as the *thickness* of a fluid. Thus, water is a thin fluid, with a lower viscosity than honey which is thick. The less viscous the fluid is, the greater its ease of movement (fluidity). In biology, this measure is not only important to characterized fluids (e.g. blood, cytoplasm) but also because most soft biological materials exhibit a viscoelastic behavior, combining viscous and elastic elements [Janmey et al., 2007].



**Figure 1.2: Geometrical meaning and scales of relevant mechanical properties for biology**  
**a.** Schematic representation of the deformation of a 2D material when a uniaxial force is applied. Strain is quantified by the change in shape. Stiffness, as measured by the Young's modulus  $[E]$ , relates the axial strain to the force (stress) applied. The Poisson's ratio  $\nu$  describes the relative transverse strain, divided by the relative axial strain of the object undergoing a deformation. **b.** Biological materials are soft materials. Their Young Moduli range from  $0.01 \text{ kPa}$  for brain tissue to a hundred  $\text{kPa}$  for cartilage [Levental et al., 2006]. Stiffness measurements for cells and intracellular organelles lay between  $0.1 - 10 \text{ kPa}$  - however the measured values vary widely even for the same type of cells, as exemplified here with three different values for fibroblasts (I-III) (s. Table 1.1. for more details and references) **c.** Compressibility is measured by the Poisson's ratio  $\nu$ . Most compressible materials contract laterally when stretched and expand laterally when compressed and thus have a positive  $\nu$  that lays between 0 and 0.5. Few rare materials exhibit a negative Poisson's ratio and actually expand transversally when compressed [Schenk and Guest, 2011, Trickey et al., 2006, Lakes, 1987]. **d.** Biological fluids have a low dynamic viscosity e.g. the cells cytoplasm has been measured to be about 5 times more viscous than water. [Luby-Phelps, 2000].

Purely elastic behavior describes the deformation of an ideal solid, which immediately deforms to a certain extent when a force is applied, stays in the deformed deformation as long as the force is present and returns to its original shape when the force is removed. An ideal liquid, on the other hand, deforms without limit for as long as the stress is applied and then remains in the deformed state when it is removed. In this case, it is the *rate* of the deformation (the time derivative of strain  $\frac{d\sigma}{dt}$ ) which is related to the force magnitude ( $\sigma$ ) by the proportionality constant: ( $\eta$ )

$$\sigma = \eta \cdot \frac{d\sigma}{dt} \quad (1.1)$$

Viscous deformation is therefore a time dependent quantity. The SI unit of viscosity is  $\text{Pa} \cdot \text{sec}$ . With a value of  $2\text{-}10 \text{ mPa} \cdot \text{sec}$ , the cells cytoplasm has been measured to be five times more viscous than water [Luby-Phelps, 2000] (**Fig. 1.2 d**).

### Compressibility

A material's compressibility describes in a first stance the change in volume of an object after a force is applied. Geometrically, it can be interpreted as the relative contraction strain  $\epsilon_{transverse}$  (transverse strain, normal to the applied stress) divided by the relative extension strain  $\epsilon_{axial}$  (axial strain, in the direction of the applied stress) that an object undergoes when force is applied to it (**Fig. 1.2 a**):

$$\nu = \frac{\epsilon_{transverse}}{\epsilon_{axial}} \quad (1.2)$$

The Poisson's ratio  $\nu$  ranges from values between 0 and 0.5. The lower the Poisson's ratio the more compressible the material. Because of their high amount of water, biological materials have high poisson's ratio's laying in incompressible or very low compressible range (**Fig. 1.2 d**) [Boal, 2002].

### 1.1.2 Calculation of mechanical properties in continuum mechanics

Calculations in mechanics to determine mechanical properties are all based on describing the geometrical change in shape of an object i.e. its deformation in response to a given applied force [Boal, 2002]. Mathematically, the description of deformations is based on analyzing the difference in positions of points  $x_i$  within an object, described by a displacement vector  $u_i$  :

$$u_i = x'_i - x_i \quad (1.3)$$

which, in the case of a deformation, is not uniform over the surface of the object. A constant displacement  $u_i$  of all positions  $x_i$  represents a translation. The local variation in  $x_i$  of direction and magnitude of  $u_i$  provides a description of how the elements of the object move with respect to each other during the deformation.

To apply this point-based geometry concept to physical bodies, tensors are employed to define the properties of a physical system over a continuum of points. Two tensors build the basics of elasticity theory: the *strain* and the *stress* tensors.

The *strain tensor* describes the deformation of an infinitesimal volume element. It is defined as:

$$u_{ij} = \frac{1}{2} \left( \frac{\partial u_i}{\partial x_j} + \frac{\partial u_j}{\partial x_i} + \frac{\partial u_l}{\partial x_i} \frac{\partial u_l}{\partial x_j} \right) \quad (1.4)$$

For small deformations the terms  $\frac{\partial u_i}{\partial x_j}$  are small in comparison to 1, and the quadratic term  $\frac{\partial u_l}{\partial x_i} \frac{\partial u_l}{\partial x_j}$  can be neglected. Thus, the *strain tensor* can be linearized to:

$$u_{ij} = \frac{1}{2} \left( \frac{\partial u_i}{\partial x_j} + \frac{\partial u_j}{\partial x_i} \right) \quad (1.5)$$

The *stress tensor*  $\sigma_{ij}$  describes the internal forces (stresses) arising in response to external forces. In static equilibrium, the sum of external  $f_i$  and internal forces vanishes:

$$\frac{\partial \sigma_{ij}}{\partial x_j} + f_i = 0 \quad (1.6)$$

In a linear approximation, the relationship between the *strain* and the *stress* tensors is given by the generalized Hooke's law:

$$\sigma_{ij} = C_{ijkl} u_{kl} \quad (1.7)$$

where  $C_{ijkl}$  is the rank 4 tensor of elastic constants. Because of the four indices, in principle there are  $3^4 = 81$  components of  $C_{ijkl}$  in three dimensions. However, for isotropic, homogeneous materials  $C_{ijkl}$  contains only two independent constants: the Young's modulus ( $E$ ) and the Poisson's ratio ( $\nu$ ). With this consideration, the *strain-stress* relationship can be written explicitly as:

$$\sigma_{ij} = \frac{E}{1+\nu} \left( u_{ij} + \frac{\nu}{1-2\nu} u_{ll} \delta_{ij} \right) \quad (1.8)$$

Consequently, the Young's modulus ( $E$ ) describing the material's stiffness and the Poisson's ratio ( $\nu$ ) describing the material compressibility play a role of canonical parameters to describe the material properties of a given material.

## 1.2 The cell's mechanical phenotype

The field of cell mechanics is a relative new and very interdisciplinary research field. The fact that diverse research approaches arise from groups specialized in very heterogenous areas (e.g. cytoskeleton and cell migration cell biology, material research physics, computational mechanical modeling) has resulted in a lack of unifying general concepts to refer to. This section aims at giving an overview of the factors determining and affecting a cell's mechanical phenotype.

Here I introduce the term **mechanical phenotype**, which will refer to *the collective set of observable features describing how a cell reacts to force*. This includes the measurable mechanical properties of the cell and cellular components (stiffness, viscosity, compressibility, etc), but also the cell's reaction to forces (rearrangements of cytoskeleton components, resistance to force) or to changes to the mechanical properties of the environment. Following factors play a role in defining the cell's mechanical phenotype and will be outlined in this section: the internal structures that define cellular mechanics (sec. 1.2.1), the the physical environment in which the cells are embedded (sec. 1.2.2) and the alterations in mechanical behavior of the cells in disease (sec. 1.2.2).

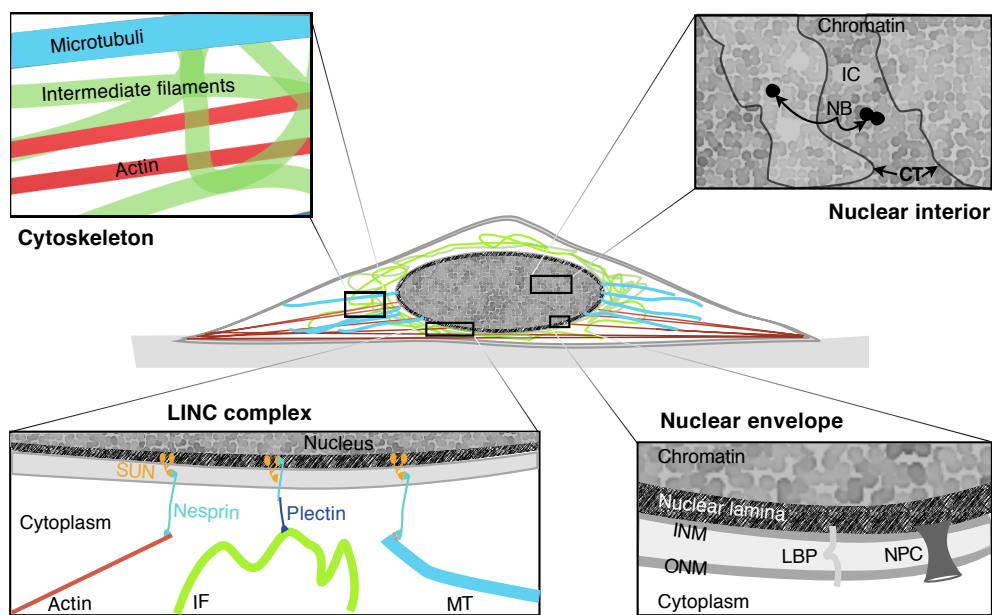
### 1.2.1 Structures defining cellular mechanics

The mechanical behavior of the whole cell is the result of the integrated interactions and the mechanical properties of the individual components of which it consists. The main players in defining the material properties of a eukaryotic cell are 1. the nucleus 2. the different cytoskeleton filaments and 3. the LINC complex (**Fig. 1.3**).

#### The Nucleus

The cell nucleus is, with an average size of 10-20  $\mu\text{m}$ , the largest organelle in animal cells. Evolved in eukaryotic cells, it functions as a storage site for most of the DNA and facilitates the reactions of essential processes like replication, transcription and splicing through its functional architecture [Dundr and Misteli, 2001]. But far from being just a spatial barrier leading to compartmentalization, the mechanical properties of the cell nucleus have to provide mechanical stability against shearing forces to ensure the integrity of the genome [Dahl et al., 2004]. Both the nuclear





**Figure 1.3: Structures defining the mechanical properties of the cell.** Overview of the structures involved in forming the cellular mechanical continuum. The **nucleus** is the biggest and stiffest structure in eukaryotic cells, in its interior chromatin is organized in chromosome territories (CT) with interchromosomal space (IC) in between. Nuclear bodies (NB) are aggregations of specific proteins. The nuclear envelope consists of an inner nuclear membrane (INM) and an outer nuclear membrane (ONM) spanned by nuclear pores (NPC) and lamin binding proteins (LBP). The nuclear lamina lies underneath the membranes. The LINC complex connects the nuclear lamina with the cytoskeleton filaments. More detailed information about these structures is found in this section.

interior as well as the proteins in the nuclear envelope determine the mechanical behavior of the nucleus.

**Nuclear interior** The molecular mechanisms of individual processes taking place inside the cell nucleus have been studied extensively, but far less is known on how all these reactions are spatially integrated and temporally coordinated within the 3D meshwork of the nucleus. Although the existence of a nuclear scaffold or mesh arranging different nuclear components has been controversial [Pederson, 2000], it is known that the interior of the cell nucleus is highly organized with several morphologically distinguishable intranuclear structures (**Fig. 1.3**). Through its association with histone proteins, the DNA is greatly condensed in the nucleus into chromosomes, which during interphase occupy distinct nuclear volumes called chromosome territories (CT) [Cremer et al., 2006]. Chromatin

free space, the so called interchromatin space (IC), contains macromolecular complexes that are required for replication, transcription, splicing and repair [Cremer and Cremer, 2001]. Different compaction levels in variable chromosome parts contribute to a complex organization and topography within the territories. These arrangements of lightly packaged (euchromatin) and tightly packaged (heterochromatin) DNA segments together with the distinct non-random localization of the chromosome territories inside the nucleus is thought to play an important role in the regulation of the genome by activating or silencing transcription or specific genes, or by enabling gene-gene interactions [Fraser and Bickmore, 2007].

Besides the chromosomes, several nuclear substructures are observed in the interior of the nucleus. Despite the absence of enclosing membranes, these so called nuclear bodies constitute enclosed spaces that can be morphologically identified by microscopy [Lamond and Sleeman, 2003]. Each of these bodies arises from the accumulation of specific proteins at distinct nuclear spaces. The nucleoli are the biggest and most notorious among the nuclear substructures. They assemble around the tandemly repeated ribosomal DNA genes, coordinating all processing and assembly steps required for ribosome-subunit biogenesis [Boisvert et al., 2007]. Other nuclear bodies are cajal bodies, small spherical structures present in 1-5 copies per nucleus with a size of 0.1-1  $\mu\text{m}$  and containing several macromolecules involved in transcription and processing of RNA [Gall, 2000]; nuclear speckles, appearing as irregular structures in various sizes and enriched in pre-messenger RNA splicing factors [Lamond and Spector, 2003]; and PML bodies, named by their major structural component the PML protein and present as 10-30 copies per nucleus in sizes ranging from 0.3-1  $\mu\text{m}$  [Dellaire and Bazett-Jones, 2004].

**Nuclear envelope & the nuclear lamina** The nuclear envelope separates the nuclear interior or nucleoplasm from the cytoplasmic compartments of the cell. It consists of two concentric membranes, the inner- (INM) and the outer nuclear membranes (ONM), separated by a luminal space and periodically connected by nuclear pore complexes (s. **Fig. 1.3**). The outer nuclear membrane is continuous with the endoplasmic reticulum and is covered with ribosomes. Underneath the inner nuclear membrane lies the nuclear lamina [Burke and Stewart, 2002]. Toward the inner side of the nucleus, several membrane proteins are embedded in the inner nuclear membrane binding to lamin polymers. These lamin-binding proteins to-

gether with the network of lamin polymers build the nuclear lamina, a thin protein meshwork which is also associated with the underlying chromatin [Crisp and Burke, 2008].

Lamins are the major components of the nuclear lamina. They are type V intermediate-filament proteins, a family of proteins characterized by a central coiled-coil 'rod' domain that polymerize into stable filaments and which have been grouped into five types on the basis of amino-acid sequence identity [Herrmann et al., 2007]. Lamin proteins are further grouped as A- and B type lamins on the basis of their biochemical properties. B type-lamins are encoded by two different genes (LMNB1, LMNB2). They are essential for cell viability and are therefore found in every cell type. In contrast, both A type lamins (lamin A and C) are derived from one single gene (LMNA) by alternative splicing and are expressed only in differentiated somatic cells with different degrees of expression across cell types [Gruenbaum et al., 2005].

Apart from other important cellular functions, such as chromatin- and nuclear envelope organization as well as regulation of gene expression [Dechat et al., 2008], Lamins are known to provide a structural framework for the nucleus [Lammerding et al., 2006]. The lamina has been described as a 'tensegrity element' (i.e. providing tensional integrity), which protects the nucleus from physical damage by determining shape, size and strength of the nucleus [Hutchison, 2002]. Experiments on lamin A knockout (LMNA<sup>-/-</sup>) mouse fibroblasts have identified lamins A and C as the primary contributors of nuclear stiffness [Lammerding et al., 2006]. Another feature of lamins is the regulation of the interactions between the nuclear lamina and the cytoskeleton components (e.g. actin and microtubules) as they are believed to co-exist in a mechanical continuum that plays an important role in mechanotransduction [Hutchison and Worman, 2004]. Experiments where fibroblast nuclei of LMNA<sup>-/-</sup> mice showed attenuating signaling compared to normal mice after exposure to mechanical stress support this hypothesis [Lammerding, 2004].

### **The Cytoskeleton**

The cytoskeleton is a dynamic and interconnected network of filaments in the cytoplasm with several functions. On the one hand, it serves as a scaffold, spatially organizing the cell and connecting it physically and biochemically with the cell

exterior. On the other hand, it generates coordinated forces that enable the cell to maintain or change its shape, migrate and divide. Central to this work is its role in rendering mechanical resistance to the cell. There are three classes of cytoskeletal filaments and they are distinguished by their mechanical properties, their polarity, the dynamics of their assembly and the motors and proteins with which they associate. Interactions of these main filaments with several classes of regulatory proteins gives the system the functional versatility that defines it. Additionally, as a result of the dynamic nature of the filaments and their several interaction with other proteins, cytoskeletal structures have the important property of being at once robust and easily reconfigured [Fletcher and Mullins, 2010].

**Actin** - also sometimes referred as microfilaments - are formed by polar assembly of the actin subunit. With only 7 nm in diameter, they are the thinnest of the cytoskeleton filaments. However, thorough association with regulatory proteins they form most of the highly organized stiff structures necessary for all processes involving force generation and mechanical support. The branched networks underlying the leading edge of motile cells, filopodial protrusions and stress fibers are examples of the structures formed by assembly and disassembly of actin filaments in response to signaling cues [Naumanen et al., 2008]. The interaction of myosin motors on actin fibers is the main source of mechanical force generation in the cell. Mechanical properties of actin filaments change depending of the structures they are forming, and the proteins they are interacting with [Gardel et al., 2004]. However, experiments proving local cellular stiffness, as well as studies with actin disrupting drugs, have shown that actin filaments are the main contributors of cellular stiffness [Costa et al., 2006].

**Intermediate filaments** In contrast to actin and microtubules, intermediate filaments comprise a whole family of proteins characterized by the same domain organization. They are classified into five types on the basis of their sequence identity and tissue distribution. Four of these types (I+II: keratins, III: vimentin, desmin a.o., IV: neurofilaments proteins, nestin, a.o.) are cytoplasmatic proteins, while the fifth type, comprised by nuclear lamins (s. sec. 1.2.1) are found in the nucleus. Intermediate filament proteins are also differentially expressed across differentiated cells, making them useful cell differentiation markers [Herrmann et al., 2007]. In the cytoplasm, intermediate filaments form networks surround-

ing or 'caging' the nucleus that play an important role in stabilizing the shape of cells [Goldman et al., 1996] and positioning cellular organelles like the nucleus [Dupin et al., 2011] and the mitochondria [Nekrasova et al., 2011]. These networks are cross-linked to each other as well as to actin and microtubules by plectin proteins [Wiche, 1998] and are therefore important mediators of cytoskeletal crosstalk [Chang and Goldman, 2004]. They also play an important role in cellular mechanics by providing mechanical resistance in particular to tensile forces. There are cell types that assemble intermediate filaments in response to mechanical stress [Stroka et al., 2012]. As stress-stiffening polymers they are particularly important for large cellular deformations [Herrmann et al., 2009].

**Microtubules** are the thickest and stiffest of all polymers. They radiate through the cell from the nucleus forming a network of tracks that serves as a highway for intracellular trafficking. During mitosis, they are in charge of segregating chromosomes through the formation of the mitotic spindle. Their involvement in such complex functions is enabled by their amazing assembly dynamics, a process called dynamical instability: phases of slow growth and rapid shrinkage [Kersemakers et al., 2006]. Although their role in cellular mechanics is mostly overshadowed by these important cellular functions, microtubules are important in the resistance of high compressive loads [Brangwynne et al., 2006].

### The LINC Complex

A physical connection between the cytoskeleton and the nucleus, linking the cell into a whole mechanical continuum from the cell adhesion sites and into the nucleus, had long been hypothesized. In recent years, many of the key proteins connecting actin, microtubule and intermediate filaments to proteins in the nuclear envelope have been characterized and collectively called the LINC complex (as in **l**inkers of the **n**ucleoskeleton to the **c**ytoskeleto) [Méjat and Misteli, 2010]. The LINC complex consist of proteins (SUN-domain transmembrane proteins) in the inner nuclear membrane (ONM) that from one side bind to the nuclear lamina and from the other side connect to KASH-domain proteins (Nesprins). KASH-domain proteins are located in the outer nuclear membrane (ONM) and connect to the different cytoskeleton filaments on the cytoplasmic side (s. **Fig. 1.3**). In this way, LINC proteins build a physical bridge between the nuclear lamina and

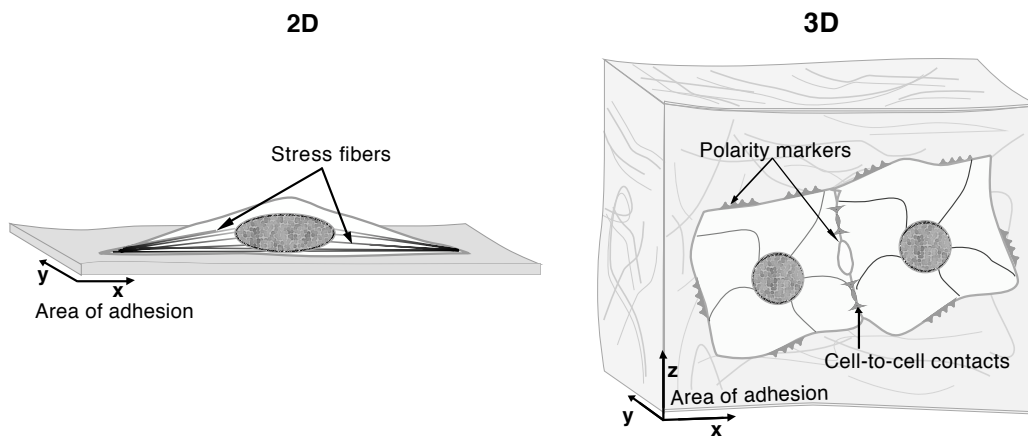
the cytoskeleton that is critical to transmit forces from the cytoskeleton into the nucleus [Lombardi et al., 2011a].

### 1.2.2 The cell's mechanical environment

Cells sense and respond to the mechanical cues exerted by the extracellular matrix and from cell-to-cell connections and are so mechanically coupled to their environment. The molecular composition, the mechanical properties and the dimensionality of the extracellular matrix (ECM) all play a role in how the cell will organize internally and adjust its mechanical properties (**Fig. 1.4**).

Most research in cell biology is still performed in flat two-dimensional (2D) plastic cultures, despite the fact that major differences in cellular behavior and physiology have been observed when cells are surrounded by a 3D environment [Griffith and Swartz, 2006]. Differences in morphology [Grabowska et al., 2011], adhesion [Cukierman et al., 2001], viability [Peretz et al., 2007], migration [Meshel et al., 2005], differentiation [Hwang et al., 2006], gene expression [Li et al., 2007] and even drug metabolism [Nakamura et al., 2003] have been recently documented. There are particular cellular systems in which the essentiality of 3D cultures cannot be overseen: primary epithelial cells only maintain their characteristic polar phenotype and form organotypic structures when embedded within 3D substrates [Godoy et al., 2009]. The study of the maintenance of epithelial apical-basal polarity is relevant because its loss is a key feature of malignant transformation of epithelial cells towards melanomas [Walker and Brugge, 2006]. In general, recent studies pointing at changes in migration and invasion strategies of cancer cells in 3D vs 2D environments are highlighting the importance of adopting 3D substrates as a standard in cancer research [Pathak and Kumar, 2011].

In organisms, the ECM is tissue specific and consists of a heterogeneous mixture of polymers and water that is hard to reproduce for laboratory cultures. However, many alternatives of simpler matrices have been developed that can mimic the structural integrity provided by the physiological ECM [Page et al., 2012]. These matrices can be made of natural or synthetic components and exhibit different compliance and mechanical characteristics depending on their composition (extensively reviewed in [Yamada and Cukierman, 2007]). As type I collagen is the primary structural component in physiological ECM, gels formed out of reconstituted collagen are a widely used. Collagen gels are biologically compatible



**Figure 1.4: Structural differences of cells cultured in 2D and 3D substrates.** When surrounded by a 3D matrix of adhesion proteins, cells exhibit dramatic changes in their structural organization in comparison to cells plated in 2D substrates. The total area of adhesion is increased, enhancing the physical cues cells receive from their environment. Cells, and epithelial cells in particular, also only make strong cell-to-cell contacts when in the 3D environment. They also maintain its characteristic polarity. In 2D substrates, more prominent cytoskeleton structures are observed, as exemplified here by the appearance of stress fibers.

with many cell types although they are softer and more hydrated (99%  $H_2O$ ) than natural tissue ECM (20%-70%  $H_2O$ ). In addition, because the fibers within are only entangled and not covalently bound, these gels exhibit high local heterogeneity [Pedersen and Swartz, 2005].

### 1.2.3 Altered mechanical properties in disease

As mentioned in the first part of the introduction, alterations in the mechanical properties of the cell and nucleus have been linked to several diseases. Many of the cases are directly related to loss of mechanical resistance in specific cells leading to mechanical damage, like in lung dysfunction, osteoporosis and arteriosclerosis. Here, two disease types in which alterations of mechanical properties of intracellular structures (specifically the nucleus) or where alterations in mechanical properties is a requirement for the acquisition of new functionalities will be outlined more in detail.

#### Laminopathies

The laminopathies are a series of disorders that arise as a consequence of different mutations in nuclear envelope proteins. Although most of the laminopathies share

mutations specifically in the LMNA gene, they manifest as diverse pathologies including muscular dystrophy, lipodystrophy, neuropathy and progeroid (or premature aging) syndromes [Korf, 2008]. Many factors characterize this collective set of diseases like mislocalization of nuclear proteins [Sullivan et al., 1999], structural anomalies in cytoskeleton organization [Broers, 2004], hampered wound healing [Lee et al., 2007] and DNA repair mechanisms [Manju et al., 2006]. As so often seen in human disease, there is no one individual mechanism to which the disease phenotypes of the laminopathies can be attributed. Disease-causing mechanism, mostly result from lamin envelope protein aberrations and are in part structural, in part modifications of signaling pathways and finally alterations in the mechanical properties of the nuclei [Capell and Collins, 2006, Maraldi et al., 2011]. Nuclei in laminopathies have been observed to be more fragile [Lammerding, 2004] or stiffer [Verstraeten and Lammerding, 2008], depending on the disease.

### **Cancer and malignant transformation**

Changes in cellular and nuclear properties are also important factors during cellular malignant transformation processes leading to cancer and metastasis [Kumar and Weaver, 2009]. Metastatic cancer cells achieve the mobility and deformability they need to squeeze through the surrounding tissue through changes in their cytoskeleton filaments [Hall, 2009], which have a drastic effect in the cell's mechanical properties [Suresh, 2007].

This is specially true for carcinomas, the most prevalent types of tumors. They arise from dedifferentiation and aberrant control of proliferation of epithelial<sup>1</sup> cells [Baum et al., 2008]. In healthy epithelial tissue, cells are characterized by a highly polarized phenotype and multiple cell-cell adhesive junctions, which ensure the mechanical integrity of tissues. Transient loss of the polarized phenotype relates to chronic inflammation leading to tissue fibrosis [Grünert et al., 2003]. This malignant transformation is associated with the morphologic and genetic transition of epithelial cells to fibroblastoid- or mesenchymal-like cells (EMT) and characterized by drastic cell shape changes, loss of cell-cell adhesion molecules, increased cellular motility and enhanced invasive potential [Gotzmann et al., 2006].

The transforming growth factor  $\beta$  (TGF- $\beta$ ) is known as the master regulator

---

<sup>1</sup>from the Greek *epi*:= "on, upon," and *thele*:= "nipple".



of EMT [Wendt et al., 2009]. TGF- $\beta$  is a multifunctional cytokine involved in development, cellular differentiation and survival. Although it can act as an effective suppressor of cell proliferation in healthy tissue, it is also an important promotor of cell malignant transformation. Interestingly, there is a functional connection between TGF- $\beta$  and the nuclear proteins A-type lamins. TGF- $\beta$  signaling can be modulated through interactions with the lamina-associated peptide 2 (LANA1) or the protein phosphatase 2A (PP2A) [Andres and Gonzalez, 2009]. As in the case of stem cell differentiation [Pajerowski et al., 2007], there seems to be a link between genomic plasticity (gain or loss), lamin-A expression and the morphological changes accompanying EMT transition.

## 1.3 State of the art

### 1.3.1 Approaches to measure cellular mechanical properties


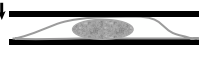
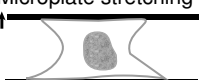






Measuring mechanical properties at the small scales found in cell biology has presented several methodological challenges resulting in bridging together interdisciplinary research across the areas of physics, biology, engineering and computational modeling. An overview of the methods used so far to measure cellular mechanical properties together with a brief description and the mechanical parameters measured in representative studies is given on **Table 1.1**. As it can be appreciated in this overview, different parameters can be measured depending on the method used. This is a consequence of both the experimental setup and the way the measurements are interpreted. The heterogeneity of the experimental setups and the mechanical models used to interpret the results might also explain why measurements of the same parameters for the same cell show so different results (e.g compare the values measured for the Young Moduli in the different fibroblast studies [ $E_{fibroblasts}$ ]).

The basic idea behind all methods is the application of some kind of force and the quantification of the cellular reaction to the force applied. Forces can be mechanical, like in the case of cell compression with microplates or optical, like in the case of optical tweezers or optical stretchers; they can be applied globally to the whole cell or locally like in the case of AFM and particle microrheology<sup>2</sup> and

---

<sup>2</sup>Recently renamed to particle tracking *nanorheology* so that we keep aware on the truly small scale of these particles.

Table 1.1: Experimental methods to study cellular mechanical properties

Method	Force applied by	Parameter $E^a$ , $\mu^b$ [kPa]; $\nu^c$ ; $\eta^d$ [Pa*s]
AFM 	Pushing a cantilever against the cell surface. Deflection of the cantilever is measured optically to determine an elasticity value.	$E_{epithelial} = 10-13$ [Lekka et al., 1999] $E_{fibroblasts} = 0.6-16$ [Mahaffy et al., 2004] $E_{endothelial} = 1.5-5.6$ [Costa et al., 2006] $E_{myocytes} = 35-42$ [Lieber et al., 2004] $E_{osteoblast} = 35-42$ [Takai et al., 2005] $E_{chondrocytes} = 2-4$ [Claessens et al., 2006]
Microplate compression 	Compressing cell between plates. Deformation description by microscopy.	$E_{myoblast} = 2$ [Peeters et al., 2005] $E_{endothelial} = 0.5$ [Caille et al., 2002a]
Microplate stretching 	Pulling apart of plates where cell is adhering. Deformation description by microscopy.	$E_{fibroblasts} = 1-10$ [Fernández et al., 2006] $E_{myocytes} = 1.5-11$ [Nagayama et al., 2006]
Micropipette aspiration 	Aspirating the cell surface into a small glass tube. Deformation description by microscopy.	$E_{endothelial} = 0.3-0.5$ [Byfield et al., 2004] $E_{chondrocytes} = 0.5$ [Hochmuth, 2000] $E_{chondrocytes} = 0.3 \pm 0.2$ [Trickey et al., 2004]
Substrate stretcher 	Stretching of elastic substrate where cell is adhering. Deformation description by microscopy.	$E_{endothelial} = 2$ [McGarry et al., 2005] Strain Field <sub>endothelial:Cell</sub> -[Nucleus] [Caille et al., 1998] 2D Strain <sub>tenocytes:Substrate</sub> -[Cell] [Wall et al., 2007]
Optical stretcher 	Trapping and stretching a cell in suspension within an optical trap. Deformation description by microscopy.	$E_{fibroblasts} = 0.2-1$ [Park et al., 2005] Optical deformability[%] [Guck et al., 2005]
Optical tweezers 	Pulling a cell in suspension by direct optical force. Deformation description by microscopy.	$\mu_{erythrocytes} = 0.25-0.6$ [Mills et al., 2004] $\eta_{erythrocytes} = 250-600$ [Mills et al., 2004]
Microrheology 	Attaching or microinjecting small (magnetic) particles into the cell and applying shear stress or a magnetic field. Deformation measured by beads movement.	$E_{epithelial} = 0.25-0.6$ [Crocker and Hoffman, 2007]
BIN <sup>e</sup> 	Ballistically injecting even smaller particles into the cell. Brownian motion is tracked and put in relationship to the elasticity and viscosity of the environment.	$\eta_{endothelial} = 140 \pm 10$ [Panorchan et al., 2006] $\eta_{fibroblasts} = 100 \pm 30$ [Kole et al., 2004]

<sup>a</sup>Young's modulus<sup>b</sup>Shear modulus<sup>c</sup>Poisson's ratio<sup>d</sup>Dynamic viscosity<sup>e</sup>Ballistic injection nanorheology

they can be applied directly or indirectly by applying them to the substrate the cells are attached, like in the case of substrate stretchers. Depending on the kind of force and the scale at which it is applied, different parameters can be determined from the measurement.

Furthermore, the material parameters are usually determined by measuring the response of cells to force application and comparing the experimental results with computational modeling predictions. Therefore, an important aspect to take into consideration is the mechanical models used to interpret the deformations. The cell interior is not homogenous [Luby-Phelps, 2000] and even if the contribution of individual structures was understood, it would still be hard to model cell mechanics as the sum of the parts of the structures involved in determining them. In particular, methods measuring local properties inside the cell have pointed to the magnitude of inhomogeneities across the cytoplasm [Weihs et al., 2006]. However, if the length scale of interest is larger than the length scale over which the structure and properties of the cell vary, a degree of homogeneity can be assumed and mechanical continuum approaches that measure an overall mechanical response can be applied [Vaziri and Gopinath, 2007]. Continuum models ignore the details of the microstructure and forces are described as stresses to the corresponding strains, having the advantage that stress distributions can be determined by the more established methods of analysis of continuum mechanics (s. sec. 1.1.2). Although the true biological character of the cell is just marginally considered and many simplifications have to be assumed, continuum based approaches are still in wide in use. Many questions are open in the field of cell mechanics and different techniques can approach these questions from different perspectives. Microrheology techniques, that sample and characterize the cell interior regionally, will help to understand and expand the fundamentals of the structures contributing to provide mechanical stability in the cell, however, and as claimed by the own authors "the vast majority of rheological claims about the cell are locally correct but should not be extrapolated to the cell as a whole" [Heidemann and Wirtz, 2004]. Heterogenous detailed information becomes a disadvantage to deal with when comparing different cell phenotypes, where averaged values might be suitable enough to explain the changes in overall mechanical behavior related to a certain state or to explain the acquisition of new cellular functions.

The field of cellular mechanics is relatively new in comparison to molecular or cellular biology and although several methods have been developed in the last

20 years, no standard techniques or models have been established so far. But it's not only the different scales and model assumptions that lead to the resulting divergence of measured values even for the same cell type, as shown in **Table 1.1**. These differences can be further explained by the conditions in which cells are kept before and during the experiments. As outlined in sec. 1.2.2, the substrate in which cells are seeded dramatically influences the organization of structural components involved in defining cell mechanical properties. Most of the methods developed so far require a direct contact to the cells to exert forces on them. This often requires plating the cells in special glass plates or chambers that can be fit into the measurement devices. Optical based methods usually work best with cells in suspension that can be caught completely into the optical traps - this is well suited for suspension cell types like blood or immune cells, but it represents a very artificial test for adherent cells. The lack of accessibility imposed by having cells surrounded by a 3D matrix renders most of established methods unsuitable for 3D culture studies. Microrheology measurements have been made suitable for measuring cells embedded in 3D substrates by inserting particles through "ballistic bombardment" [Panorchan et al., 2006], however one has also to take into consideration the cell damage and mechanical trauma suffered by the cells with this highly invasive introduction of particles.

In summary, despite the fact that several methods exist to measure cellular mechanical properties, this method palette is still in need of:

1. **Non-contact & non-invasive methods.** Methods like microplate stretching and compression, micropipette aspiration and AFM that require direct application of mechanical forces to the cell membrane have two major drawbacks. One is that cells are often damaged by the direct mechanical contact and the second one is that the need of the direct physical connection to the experimental setup constrains both the measurement of intracellular structures and the use in cells embedded in 3D substrates.
2. **Methods that allow measurements of a statistical significant amount of cells.** The experimental difficulty often associated with the type of biophysical experiments used to measure mechanical properties often results in studies where only a couple of cells per condition can be analyzed. This makes most methods unsuitable to measure statistical significant results. So far, only the optical stretchers are able to measure hundreds of cells. However, the optical

stretcher has the important restriction that the cells have to be in suspension.

### 3. Measurements in more physiological conditions, specially in 3D environments.

With the exception of BIN, none of the established methods has been optimized for measurements with cells embedded in 3D substrates. This is not only due of the reasons stated in 1., but also because the field of 3D substrates for cell culture is also an emerging field with current challenges of its own.







The necessity for these features applies in particular for methods that are able to measure the mechanical properties of the whole cell in respect to force and are not constrained by the local composition of the cell at the specific spatial point at which the measurement is being performed (as in AFM and the particle nanorheology techniques).

#### 1.3.2 Experimental approaches to study nuclear mechanics

Several of the experimental approaches conceived to study cellular mechanics have been adapted to measure nuclear mechanical properties. As in the case of the cell, the goal of the experiments is to induce a deformation of the nuclei that can be quantified together with the force applied to extract mechanical parameters. The nucleus is embedded in the cell and surrounded by the cytoskeleton. Therefore, the different methods have to either account for the fact that no direct measurements of nuclear mechanical properties are possible or prior isolation of the nucleus has to be performed. Measurements on isolated nuclei have accounted for absolute values regarding nuclear mechanical properties (s. **Table 1.1**).

However, there are many disadvantages related to removing nuclei out of the chemical and physical environment within the cell: i. variation of the chemical composition of the buffers used has an effect on the nuclear structures [Dahl, 2005] ii. the isolation process itself involves chemical or physical manipulation of the nuclei, which introduces a bias in the measurements [Lammerding et al., 2007] iii. the mechanical context of the nucleus itself is lost, which poses the questions if the conclusions taken out of these measurements can be transferred to physiological conditions. An overview of the approaches used so far to assess nuclear mechanical properties is presented in **Table 1.2**.

Table 1.2: Experimental methods to study nuclear mechanical properties.

Method	Isolation?	Studies
Atomic Force Microscopy		[Dahl, 2005]
Micropipette aspiration		[Dahl et al., 2004] [Dahl, 2005] [Rowat et al., 2006] [Pajeroski et al., 2007, Guilak et al., 2000]
Cell compression		[Broers, 2004, Caille et al., 2002b, Guilak, 1995]
Cell strain		[Caille et al., 1998, Lammerding, 2004, Gilchrist et al., 2007, Lammerding and Lee, 2009]
Magnetic bead microrheology		[Lammerding, 2005, de Vries et al., 2007, Tseng et al., 2004]
Microneedle manipulation		[Maniotis et al., 1997, Lombardi et al., 2011a]

Together these studies have provided the following insights regarding the nature of nuclear mechanics [Rowat et al., 2008, Lombardi and Lammerding, 2010, Martins et al., 2012]:

- **The nucleus is stiffer than the cytoplasm and contributes largely to the mechanical properties of the cell.** With the help of cell compression and micropipette aspiration experiments and subsequent analysis of the deformations of the whole cell and nucleus, a stiffness 3-4 fold higher was measured for the nucleus relative to the cytoplasm [Guilak et al., 2000, Gilchrist et al., 2007, Caille et al., 2002a].
- **The nuclear interior is a largely aqueous material and shows viscoelastic properties.** Volume changes under micropipette aspiration revealed a nuclear volume decrease of 60-70% before reaching a deformation resistance state [Rowat et al., 2006]. With a measured elastic modulus between 30-250 Pa - depending on the length scale tested - the nuclear interior is much softer than the nuclear envelope [Guilak et al., 2000, de Vries et al., 2007].
- **The nuclear envelope provides structural stiffness.** The behavior of the nuclear envelope during micropipette aspiration indicated that the nuclear envelope resists shear forces due to the concentration and structure of lamin

A filaments [Rowat et al., 2006, Dahl et al., 2004]. The nuclear lamina contributes to a major extent to the structural stiffness of the whole nucleus, which lies in a range of 1-200 kPa.

- **The nucleus is physically linked to the cytoskeleton.** Forces applied to the cytoskeleton are transmitted to the interior of the nucleus through SUN and Nesprin proteins [Lombardi et al., 2011a].

Although these qualitative features are fairly consistent between experiments, results from approaches to determine quantitative measures for the elastic or viscoelastic properties differ considerably. For instance, micropipette and AFM experiments report a measured nuclear elasticity in the range of 1-10 kPa, while particle tracking microrheology account for an average elasticity of about 200 kPa. These differences are in part methodological, as they differ in: the scale of forces applied to the nuclei, the mechanical parameters used or newly defined to fit a particular experiment and models employed to analyze the measured results. In addition, nuclei of different cell types or even different species (*Xenopus*, mouse, human) are used as probes. Lastly, as in the case of the field of whole cell mechanics, the mechanical environment in which the nuclei are kept plays a role in the resulting measured parameters: isolated nuclei exhibit different mechanical behavior than those within living cells and the structural differences between cells in different substrates can also be expected to spread into the nucleus.





# Aim

After identifying the drawbacks of current existing methods to analyze cellular and mechanical properties, the aims of this work lie in the establishment and development of novel image and model based frameworks to characterize mechanical properties and the mechanical behavior of cells in a more physiological 3D environment. By implementing confocal microscopy based experimental techniques and developing corresponding image processing analysis tools and having the advantage of addressing the problems from the biological and the theoretical side, the specific aims of this work are:

- To enhance a pre-existing method to study nuclear compressibility, optimizing experimental and analysis steps to enable the robust measurement of significant amount of cells to perform reliable comparative analyses between phenotypes.
- To perform a proof of principle study by analyzing the nuclei in a known system of mechanically impaired nuclei in a comparative study of wild type vs. LMNA<sup>-/-</sup> mouse embryonic fibroblasts (MEFs).
- To design and develop a novel method to apply controlled and known forces and deformations to cells embedded in 3D substrates.
- To implement these methods to mechanically phenotype a cellular system requiring a 3D environment for its analysis: the process of TGF- $\beta$  induced dedifferentiation in primary mouse hepatocytes (pmHCs) as a model of malignant transformation in cancer.
- To relate the observed changes in mechanical phenotype to the acquisition of new cellular functions.



# 2

## Methods (& Materials)

For this thesis two complete frameworks were established to measure mechanical properties of cells and cellular structures:

- A framework to measure the compressibility of the nuclear interior from series of nuclear deformation after disruption of the cytoskeleton with drugs, that will be referred as *Nuclear compressibility* for practical reasons and
- An experimental and computational framework for generation and quantification of cellular deformation within a 3D substrate, or *3D Substrate Stretcher*, for short.

Both of these frameworks are based on confocal microscopy experiments followed by image processing pipelines and finally coupled to image-based mechanical modeling. Therefore, many of the experimental details (cell culture, microscopy) and *in-silico* processing and analysis scripts (image pre-processing, segmentation, etc) are shared by both methods. In order to avoid repetition, these overlapping methods will be explained in general with references to details in the respective frameworks. An overview of the overlapping aspects of the methods, which at the same time gives the outline of this section is given in **Fig. 2.1**.

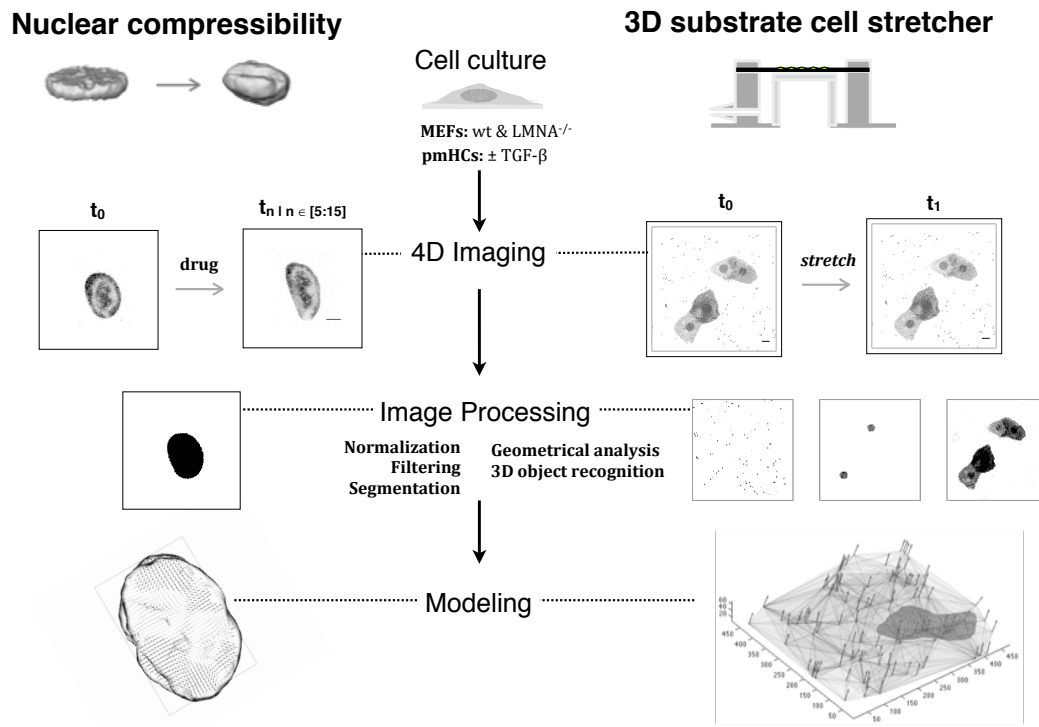


Figure 2.1: Big overview of all the overlapping methods in the developed frameworks.

## 2.1 Cell Culture

### Primary cells

#### Mouse embryonic fibroblasts

Wild type (wt) and lamin A knock-out (LMNA<sup>-/-</sup>) mouse embryonic fibroblasts (MEFs) were provided by Colin L. Stewart<sup>1</sup> (*Institute of Medical Biology, Singapore*) [Sullivan et al., 1999]. Cell batches were kept in liquid nitrogen until use. Over the course of the measurements three different batches were thawed. Cells were obtained and unfrozen at passage 3 and cultured in DMEM supplemented with 10% fetal calf serum, 1% penicillin:streptomycin and 1% L-glutamine. All experiments were conducted between passages 4 and 6. No morphological differences were observed in the cells between these passages, however after passage 7 or 8 MEFs would stop dividing.

<sup>1</sup>The group was contacted per E-Mail and cells were sent per post from Singapore approximately 8 weeks after contact. A fact to consider when thinking about working with these cells.

### Primary mouse hepatocytes

Primary mouse hepatocytes were kindly provided by Marlies Mürnseer (*II Medical Clinic, Medical Faculty Mannheim, University of Heidelberg*). Cells were received a couple of hours after isolation, cultured in Williams medium containing 10% FCS, 1% PenStrep, 1% L-Glutamat and 0,1% Dexamethason and plated in 2D or 3D collagen substrates depending on the experimental setup. As these cells don't further divide in culture conditions all experiments had to be performed within the same week of isolation.

Cells provided by  
**Marlies Mürnseer**

**Preparation of the collagen sandwich** The collagen matrices were prepared by neutralization of acid solubilized, isotonic rat tail collagen I solution. The collagen solution was mixed with one part 10x DMEM and neutralized to pH 7.4 on ice by titration with NaOH and HCl. 1 µl Fluorescent beads per 200 µl collagen I solution was added. 250 µl of the neutralized solution were distributed on the membrane and allowed to polymerize in the incubator for 60 minutes to build the first layer. After polymerization, cells were plated at a density of  $2.5 \times 10^4$  cells/cm<sup>2</sup> in Williams Medium E. After 4h adhesion time, unattached cells were removed by washing twice with PBS. A second layer of 150 µl neutralized collagen containing fluorescent beads was added dropwise on top of the cell layer. Starvation medium was added after allowing polymerization of the second collagen layer.

Preparation of 3D  
collagen substrates  
performed by **Marlies  
Mürnseer**

### Transfection & Transduction

To label structures for live cell microscopy cells were seeded in 8-well Lab-Tek chambers and transfected with Lipofectamine 24h hours afterwards. The list of DNA plasmids used for transfection is found on **Table 2.1**. Imaging was performed 24h after transfection. Because pmHCs were only inefficiently transfected with transfection reagents, vectors for fluorescent proteins were introduced via viral transduction with a powerful AAV-Virus of Elena's Lab.

AAV virus provided by  
**Elena Senis**

Table 2.1: Plasmids used for cell transfection

Protein	Plasmid	Notes
H <sub>2</sub> B	H <sub>2</sub> B-GFP	H <sub>2</sub> B was fused on its C-terminal end to mGFP with a linker containing the sites AgeI and NotI. Clonings were performed in the vectors pEGFP <sup>a</sup> N1 where EGFP was replaced by mGFP [Beaudouin et al., 2006].
soluble EGFP	EGFP	kindly provided by Jennifer Lippincott-Schwartz <sup>b</sup>
paGFP	paGFP	kindly provided by Jennifer Lippincott-Schwartz
Vimentin		Vimentin plasmids were kindly provided by H. Herrmann-Lerdon <sup>c</sup> .

<sup>a</sup> [Lippincott-Schwartz et al., 2001]

<sup>b</sup> *Cell Biology and Metabolism Branch, NIH, Bethesda, USA*

<sup>c</sup> *Cell Biology Unit, DKFZ, Heidelberg, Germany*

## 2.2 Microscopy

### 4D Confocal Microscopy

Confocal microscopy was performed with a Leica SP5 laser scanning confocal microscope equipped with the LAS software. Either the 63x or the 40x oil objectives were used. 512 x 512 pixel images were scanned at a speed of 700 mHz and with a line average of 2 scans. After acquisition, images were exported as 8 bit-gray scale .tiff files.

For 3D stacks acquisition, the xyz-mode was used with a z-step size kept constant at 0.3  $\mu\text{m}$  and a pinhole aperture of 1 AU. The xyzt mode was used when acquiring consecutive and automatic 3D time series. Standard excitation and detection wavelengths were used for the different fluorophores. An overview of the fluorescent stains and proteins together with the microscopy settings for excitation and emission is found on **Table 2.2**.

When combining fluorophores with overlapping emission wavelength ranges the sequential mode between stacks was used to avoid fluorescent bleed-through.

### FRAP

FRAP experiments were performed to calculate diffusion of soluble fluorescent proteins inside the nuclei. The diffusion coefficient  $D$  of a particle is directly proportional to the dynamic viscosity  $\eta$  of the medium in which the particle is diffusing:

Table 2.2: Overview of fluorophores used for confocal microscopy

Fluorophore	Excitation $\lambda$ [nm]	Detection range $\lambda$ [nm]
Hoechst 33258	405	420-470
Fluorescent beads	405	490-510
EGFP	488	505-520
YFP	488	505-520
Cherry	488	505-520
Rhodamine Phalloidin	543	560-580
Cell Mask	594	620-630

$$D = \frac{k_B T}{6\pi\eta R_0} \quad (2.1)$$

with  $k_B$  := Boltzman constant,  $T$  := temperature of the medium and  $R_0$  := hydrodynamic radius of the particle, at a constant temperature changes in GFP diffusion would point to changes in nucleoplasmic viscosity.

For FRAP experiments, cells were transfected with either paGFP and H<sub>2</sub>B-Cherry or H<sub>2</sub>B-GFP. Within the Leica LAS FRAP Wizard a region of interest was selected in the nucleus to be either bleached with the 488 nm laser or photo activated with the 405 nm laser. Each FRAP series consisted of: 2 pre-bleached images, 10 bleaching images, 100 post-bleached images. The sequences of xyt images were analyzed with an *ImageJ* plugin developed in house to extract the change of intensity in defined regions. Gaussian curves are fitted to the first time points and the diffusion coefficient were derived from the corresponding  $\sigma$  curves.

### 2.3 Nuclear rounding for Nuclear compressibility

The first method to study mechanical properties of the nuclear interior is based on analyzing the deformation of the nuclear interior upon chemical disruption of cytoskeleton filaments as first described in [Gladilin et al., 2010]. Deformation of the cell nuclei was induced without mechanical contact by disrupting the cellular pre-stressed state of adhering cells by either disrupting focal adhesions with Trypsin-EDTA (0.0125%) or the actin fiber network with LatrunculinB (1.25  $\mu$ m).

In order to better visualize the deformation of the nuclear interior and increase the useful information for the subsequent analysis, patterns were bleached onto the fluorescently labeled chromatin. Patterns were bleached within the FRAP Wizard in the Leica LAS Software by selecting a region of interest inside the nuclei, which was illuminated with 100% power of the 488 argon laser. For each cell, a time series of 1-3 steps prior to drug treatment and 10-20 steps after treatment was imaged. This resulted in several image stacks for each cell. The number of z-slices varied between different time series to account for differences in nuclear volume. All images were acquired with a Leica SP5 laser scanning confocal microscope with a 63x objective and stored as 8-bit grey scale image stacks.

### 2.4 3D Substrate Stretcher

The 3D substrate stretcher is based on the *StageFlexer* aluminum chamber that enables the biaxial stretching of cells growing inside a 3D substrate matrix attached to a deformable silicone membrane. The membranes were bought from *FlexCell* (s. Materials table) and placed on top of a plastic loading station and clamped at the sides by a metal top lid fixed with screws. Upon vacuum induction by taking air out with a common plastic laboratory syringe attached to the chamber through a rubber tube, the membrane is pulled at the sides and the silicone membrane where the cells are sitting is biaxially stretched. A screw clamp<sup>2</sup> served as a vacuum-controlling device to regulate the syringe movement. All modifications introduced to the chamber were performed by the *DKFZ precision mechanics lab*. To adapt the stretcher for experiments with cells in 3D, the silicone membranes were coated with a collagen sandwich as described in sec. 2.1. Fluorescent beads were mixed in the collagen with a 1:200 diluted solution of blue fluorescent beads.

For stretching experiments at the microscope, the collagen coated membranes containing the cells were mounted into the chamber and placed on the microscope stage. After a suitable image field (i.e. with at least one fit cell enclosed with beads) was found the z-volume was defined making sure that the cells were completely within the scanned image stack and that enough beads were present beneath and over the cells. A working zoom between 2.5 and 3.5 was necessary to resolve the cellular structures as well as the beads to extract them with the subsequent image

---

<sup>2</sup>A specially clever idea suggested by S. Kallenberger and quickly implemented in the carpenter's workshop of the DKFZ



analysis. At least 3 detection channels were necessary to describe stretching of 1. the fluorescent beads 2. the nucleus 3. the cell. To separate the signal of the fluorescent beads and the nuclei - both excited with the 405 nm laser and both with a huge emission range - different detection ranges were set with two different photomultipliers for detection, taking in advantage that the fluorescent beads emit well into the green wavelengths. In cases where EGFP and not CellMask was used to mark the cell the scan was acquired in sequential mode to have a clean green signal. Once these initial imaging parameters were set a first 3D image stack was acquired. Immediately afterwards the membrane was stretched. Membrane stretching causes in the first place a relative big translation in respect to the image field. Therefore, the same image field acquired before stretching had to be found after stretching by translating the stage. After the same image field was found and stable, the 3D volume was redefined and the after-stretching 3D stack was acquired.

## 2.5 Image processing pipelines

File and image processing pipelines were created in ImageJ, Matlab and R to i. sort and identify suitable image series for the analysis ii. pre-process the images to iii. extract the desired information needed for the analysis. An example of the source code for the plugins implemented in ImageJ can be found in *Appendix 1*.

### File preprocessing

Images are exported as sequentially named files into a single general folder for each day. To facilitate the identification of the acquired series and images taken, shell and ImageJ scripts were developed to efficiently sort and create visual overviews of the different series and channels. The importance of these plugins might pass unnoticed until the first time someone attempts to sort several dozens of multichannel images per hand. Shortly: new folders were created for each series, consisting of all the z-stacks for each image field in every channel acquired, and images were sorted into the corresponding series and channels folders. With this file structure an ImageJ plugin was developed to create montages of the merged z-projections for each of the acquired channels together with the printed information about the total z-stack volume information.

### **Image preprocessing**

Image analysis involves the conversion of features and objects in image data into quantitative information about these measured features and attributes.

**Normalization** The raw image stacks were imported in the image processing software *ImageJ* (National Institute of Health, version 1.4) and converted to 8-bit grayscale images. To soften the effect of intensity differences within the z-stacks and over the stacks due to photo bleaching, all image stacks were normalized with the *Stack normalizer* plugin between 0 and 255 grayscale values.

### **Filtering**

**Edge-preserving filtering** If exact information of the detailed image structures was to be extracted, images were smoothed with an *Anisotropic 2D diffusion filter ImageJ* plugin to conserve the edges while removing statistical systemic noise. By mimicking the process of anisotropic diffusion (i.e. with different properties in different directions) these kinds of filters smooth along the parallel direction of the edges but not orthogonal to them [Beil et al., 2005]. The starting parameters used for filtering were: *smoothings=10, a1=0.05, a2=0.09, dt = 20 and edge=5* and were optimized depending on the individual image series level of noise keeping in mind to use the same parameters for each set of stacks to be compared among each other.

**Simple non-edge-preserving filtering** In cases when image structures required further smoothing, as in the case of the processing for subsequent segmentation, a simpler and faster median filter [*Radius = 1 pixel*] was applied.

### **Segmentation of cellular structures**

Because all of the geometrical- and mechanical analyses are based on surfaces generated from the segmented image stacks, a precise and consistent segmentation i.e. threshold selection was needed.

**Automatic segmentation of cells & nuclei** In the cases where labeled structures were clearly separated from the background with a sufficient signal-to-noise ratio, as was the case for:

- single H<sub>2</sub>B-GFP labeled nuclei in the nuclear rounding framework
- single GFP-transduced cells in the 3D substrate stretcher

an automatic segmentation could be applied with established algorithms. To choose appropriate algorithms, the *Auto Threshold ImageJ* plugin was used to test among a set of given segmentation methods. For most cases the histogram-thresholding-based algorithms:

- Otsu: based on the minimization of intra-class variance, defined as a weighted sum of variances of the two classes **or**
- Li: Minimum Cross Entropy thresholding method

were generating the best results clearly separating the structures from the background at the outer structure edges across the z-stacks.

Remaining holes within the foreground structures (nuclei or cells) were closed in the thresholded images by consecutively applying a *dilating*, *fill holes* and *eroding* binary processes.

**Manual segmentation of cells & nuclei** In cases where structures were not clearly distinguished for the background, as was the case for most of the 3D $\lambda$  - imaging for the 3D substrate stretcher where:

- Overexposed beads were visible in the nucleus channels, despite of sequential scanning and the separated detection ranges
- Cells stains with cells mask, as it stains both living and dead cells as well as cell debris.

a manual threshold selection had to be performed. This more laborious and time consuming segmentation consisted on first removing all undesired structures of the background by manually selecting the structure to extract and *clear all* the remaining image pixels setting them to 0. After all the image rubbish was manually removed, a suitable threshold was set to segment the images. As in the case of the automatic segmentation, remaining holes within the foreground structures (nuclei or cells) were closed in the thresholded images by consecutively applying a *dilating*, *fill holes* and *eroding* binary processes.

### Generation of 3D surface and volumetric mesh models

To render the 3D volumetric surface descriptions of cells and nuclei, surface meshes were generated with *Amira*. After loading the segmented image stacks with the correct x,y,z ratio, extracted from the image meta-data, the 3D surfaces of the object was generated with the *SurfGen* operation. To reduce data volume and computation time in the further steps of the analysis, surfaces were simplified to 10 000 - 20 000 faces in the case of cells and 2000 - 5000 faces in the case of nuclei. For further mechanical analysis based on finite element calculations, corresponding finite elements model suitable tetrahedral grids had to be created for each surface with the *TetraGen* operation. Three conditions had to be met by the surfaces to enable the subsequent creation of the final tetrahedral grid: i. the surfaces has to be closed, ii. without intersecting triangles and iii. with all voxels corresponding to the objects with the correct orientation (i.e. voxels corresponding to the interior of the nucleus had to belong to the *interior* material). Therefore a closeness test, to ensure the continuity of the surface; an intersection test, to search for and eliminate intersecting triangles and an orientation test were performed on the surfaces. Additionally, it was verified that the surfaces consisted only of one *patch*, that is one set of enclosed 3D coordinates. Although this did not represent a hindering for triangulation, it was relevant for the numerical tools utilized in the next analysis steps. If the surfaces fulfilled all these requirements the *TetraGen* operation was computed on them to fill the surfaces with the appropriate number and geometry of tetrahedra.

### Rigid registration

Image registration was based on mapping the generated surfaces to each other and obtaining the xyz-translation values describing the nuclei translation between time steps. Surfaces were mapped onto each other with a mapping tool developed by Dr. Evgeny Gladilin by calculating and matching the eigenvectors of both surfaces [Gladilin and Eils, 2008].

### Quantification of geometrical properties of cellular structures

**Surface-based quantification** One possibility to quantify the volume and area of cells and nuclei was by analyzing the 3D surfaces generated by *Amira* via the *Sur-*

*faceArea* operation that calculates and displayed the total area and volume of the surface in arbitrary units by measuring the area reached by the triangles constructing the surface.

**Pixel-based quantification** As measuring geometrical features with the help of the Amira meshes was laborious and time consuming, an *ImageJ* plugin was written to assign pixels of the thresholded object to belong to the exterior or the interior part of the object depending on their neighborhood pixel. For all white pixels (i.e. the ones belonging to the object) identified, the neighboring pixels were checked and assigned to and if all of the surrounding pixels were also white, the pixel was assigned to the internal volume. If at least one pixel was black (i.e. in contact to the background) the pixel was assigned to the surface pixels. Total volume was calculated as the sum of surface and interior pixels. The counted pixels were multiplied by the x,y,z, voxel size and summed up.

### Shape descriptors

Integrated in ImageJ is the automatic calculation of shape descriptors for 2D and 3D structures. These features were measured with the particle analyzer plugins for ImageJ for the case of 2D image projections. In the case of 3D geometrical descriptions, shape descriptors were integrated in the analysis plugins Following shape descriptors were used:

- Circularity:  $\frac{4\pi \cdot \text{area}}{\text{perimeter}^2}$  with a value of 1 indicating a perfect circle. The more circularity decreases and approaches 0 the more elongated the shape.
- 2D aspect ratio:  $\frac{\text{majoraxis}}{\text{minoraxis}}$
- 3D aspect ratio:  $\frac{\text{zaxis}}{\text{xy majoraxis}}$

### 3D object recognition

To extract the positions of beads embedded in the collagen matrix of the 3D substrate stretcher, the *3D Object Counter ImageJ* plugin was applied to the complete image stack containing the beads after an edge-preserving filtering step. After manual selection of a segmentation threshold and setting a lower and higher threshold for the size of the objects to be identified, the plugin looks for objects of the given

size and joins them over the different stacks. Different properties can be measured and displayed with this plugin. The parameters used for the analysis were: the total voxel size of the particles and the center of mass of the different structures. By setting the size thresholds to only find individual beads, beads clusters were excluded, as well as objects located at the x-y edges. The result was table containing the total number of beads in the image, as well as their sizes and positions.

## 2.6 Image and model based mechanical modeling

### 2.6.1 Calculation of nuclear compressibility<sup>3</sup>

The numerical analysis workflow adopted for the analysis had been previously developed by Dr. Evgeny Gladilin and is based on a 3D finite element method on tetrahedral grids used to model and simulate intracellular mechanics [Gladilin et al., 2007]. For the physical model of nuclear deformation, the nucleus was approximated as a homogeneous, isotropic material described by the St. Venant–Kirchhoff constitutive law [Ciarlet, 1988]. In the case of a pure displacement problem where the forces are given implicitly as the boundary displacements, the material law is given by the Lamé–Navier partial differential equation of the displacement  $\mathbf{u}$ :

$$\Delta \mathbf{u} + \frac{1}{1-2\nu} \text{grad div } \mathbf{u} = 0 \quad (2.2)$$

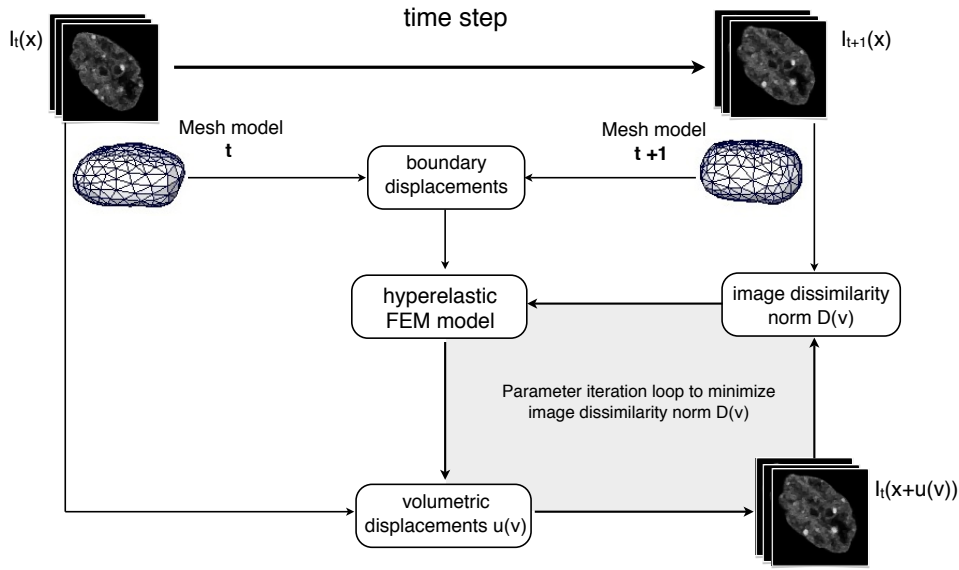
which is dependent only on  $\nu$ .

To determine the Poisson’s ratio ( $\nu$ ) underlying the deformation of the nuclear interior for each time step two data representations of the nucleus in adjacent time points are needed:

- The 3D microscopic image stacks  $I_t$  and  $I_{t+1}$
- The finite elements tetrahedral grids describing the shapes of the nuclei at time  $t$  and  $t + 1$

The boundary displacement field was computed in the form of surfaces correspondences mapping the triangulated surfaces of the nuclei. With the boundary

<sup>3</sup>Section adapted from [González Avalos et al., 2011]



**Figure 2.2: Principle of image- and model-based framework for determination of nuclear compressibility.** For each pair of adjacent time steps, finite element models of the nuclei are generated from 3D microscopic images. The displacements of the surface nodes are given by the surface correspondences mapping the nuclear boundary from one time-step onto the next. The displacements of the interior nodes  $u(v)$  are computed from the displacements of the surface nodes via the FEM and are applied to the source-image  $I_t(x)$  to calculate its deformed configuration  $I_t(x + u(v))$ , i.e., the simulated target-image. The minimum of the dissimilarity norm  $D(v) = \min(D(v))$  between the simulated target-image  $I_t(x + u(v))$  and the real next time-step image  $I_{t+1}(x)$  corresponds to the Poisson's ratio  $v_{min}$  of the nuclear interior. [Figure and legend from [González Avalos et al., 2011]]

displacement field as reference, volumetric deformations for different Poisson's ratios  $u(v)$  with  $vin[0, 0.5]$  were computed and applied to the voxels of the source image  $I_t x$  via the finite element method to generate the *in-silico* deformed image stack. Finally  $v$  is determined by minimizing the difference between the simulated  $I_t(x + u(v))$  and the experimental  $I_{t+1}(x)$  image stacks [Fig. 2.2]. :

$$v_{min} = \min(|D(v) = I_{t+1}x - I_t(x + u(v))|) \quad (2.3)$$

$D(v)$  is computed as a sum over the image points of the selected regions of both images  $I_{t+1}x$  and  $I_t(x + u(v))$ . When looking at the Taylor expansion of the image intensity as a function of displacement [González Avalos et al., 2011]:

$$I_t(x + u(v)) - I_{t+1}x \approx \mathbf{u} \nabla I_{t+1}x = |\mathbf{u}| |I_{t+1}x| \cos(\alpha) \quad (2.4)$$

one learns that the dissimilarity norm  $D(v)$  depends not only on the magnitudes of the local image gradient and the displacement vectors, but also on the relative spatial orientation of these two vectors to each other given by the angle  $\alpha$ .

## 2.6.2 Calculation and description of strains in the 3D stretcher

### Bead displacements calculation

The basis to calculate the deformation of the substrate after stress application with the substrate stretcher is based on calculating the displacements of beads in the 3D image field before and after stretching. When comparing the coordinates of the images before and after stretching, the image fields were not always identical between the two time points. Therefore, after extracting the beads coordinates for each time point, beads present in both image fields had to be selected and mapped to each other. The z-projections containing the information of all the beads identified with the 3D Object counter plugin, together with their number were used to compare beads present in both images and to remove the extra ones. Additionally beads located inside the cells were left out of the calculation to avoid bias in the calculation of substrate deformation.

After beads located in both fields were identified, they had to be matched to each other. The imageJ plugin automatically numbers beads according to their z position. However, because the z position is more error prone than the x,y as it contains also information about the point spread function, the bead numbering was reset either by their x- or their y- position in R. Because the translational component of the deformation is much bigger than the deformation component (about 10% of the whole) the relative positions to the beads was mostly kept constant and this re-arrangements generated the correct beads correspondences between both images. Beads still not corresponding to each other were assigned manually by exchanging the positions in the table. Beads displacements between the two time points were calculated by subtracting the x,y,z components in both time point for each bead. To have already the correct scale of coordinates and displacement, the x,y and z components of each coordinate were multiplied by the voxel value. A first evaluation of strain visualized in 2D was rendered to assess if the degree of substrate deformation was large enough to continue processing the rest of the series and to continue to the mechanical analysis. Both tables containing the beads



coordinates at each time point, as well as the displacement table was exported for further use in *Matlab* or *Amira*.

### Beads 3D volumetric meshes generation

Tetrahedral meshes representing the substrate in the 3D stretcher had to be created from the 3D point coordinates of the identified beads. This was performed using the Matlab function *DelaunayTri* triangulation, which in the case of a 3D set of points is composed of tetrahedra. The 3D delaunay triangulation produces a mesh of tetrahedra by connecting points in a nearest-neighbor manner while at the same time selecting large internal angles over small internal angles. Apart from producing a tetrahedral mesh suitable for the mechanical analysis, the main advantage of this Matlab function is that it additionally contains in-built methods to work with the generated structure.

### Bead interpolation test to assess substrate homogeneity

To test the homogeneity of the substrate movement while stretching, a *Matlab* script was developed to assess the interpolation accuracy of beads displacements for beads enclosed by other beads. The script for interpolation of points was adapted from a C program written by Evgeny Gladilin and is based on linear interpolation of a point's  $P$  displacement  $d_p$  from the displacements  $d_{x_1}$  to  $d_{x_4}$  of the surrounding 4 points  $x_1$  to  $x_4$  building a tetrahedron around point  $P$  (Fig. 2.3). To find all points surrounded by other 4 points i.e. belonging to the mesh interior, first all the outer points were identified by building the convex hull of the tetrahedron mesh. Points not included in the surface were assigned to the set of interior points. After retrieving the list of interior points  $P_i$  they were successively analyzed.

For each interior point  $P$ , a new tetrahedral mesh was generated from the points list after removing  $P$ . The position of  $P$  inside this new mesh was determined and the 4 points  $x_1$  to  $x_4$  building the tetrahedron in which  $P$  localized were retrieved together with their

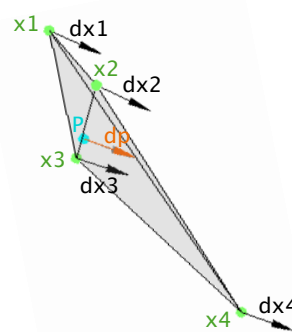


Figure 2.3: Example tetrahedron for point interpolation.

Matlab script based on  
C scripts written by  
Evgeny Gladilin

corresponding displacements  $d_{x_1}$  to  $d_{x_4}$ . The Jacobi matrix of this points, with  $x_1$  as reference was calculated :

$$J = \begin{pmatrix} (x_{2_1} - x_{1_1}) & (x_{3_1} - x_{1_1}) & (x_{4_1} - x_{1_1}) \\ (x_{2_2} - x_{1_2}) & (x_{3_2} - x_{1_2}) & (x_{4_2} - x_{1_2}) \\ (x_{2_3} - x_{1_3}) & (x_{3_3} - x_{1_3}) & (x_{4_3} - x_{1_3}) \end{pmatrix} \quad (2.5)$$

By multiplying the relative coordinates of  $V = P - x_1$  with the inverse Jacobian:

$$S = V \times J_{inv} \quad (2.6)$$

We get the shape function  $S$  for  $P$ , describing the relative spatial orientation of  $P$  towards  $d_{x_1}$  to  $d_{x_4}$ . Linear interpolation of  $d_{p_{int}}$  is finally calculated by multiplying the shape function components  $S_i$  with the corresponding components of the relative displacements,  $i = 1 - 3$ .

$$d_{p_{int}_i} = dx_{1_i} + (dx_{2_i} - dx_{1_i}) \cdot S_i + (dx_{3_i} - dx_{1_i}) \cdot S_i + (dx_{4_i} - dx_{1_i}) \cdot S_i \quad (2.7)$$

The interpolation error is calculated by comparing the actual displacement  $d_p$  with the interpolated displacement  $d_{p_{int}}$ :

$$IntError_p = \sum_{i=1}^N (d_{p_{int}_i} - d_{p_i})^2 \quad (2.8)$$

### Calculation of local substrate strain

To asses the magnitude of deformation for each tetrahedron element (**Fig. 2.3**) with points  $x_1$  to  $x_4$  and their respective displacements  $d_{x_1}$  to  $d_{x_4}$ , the linearized strain tensor 1.5 was calculated. The principal strains are found by using an eigenvalue decomposition of this tensor. The maximal deformation is described by the the largest eigenvalue. See Matlab scripts in *Appendix 2* for the detailed calculations.

### Mapping substrate strain on cell surfaces

The magnitude of deformation acting on the cell surface was estimated by taking all tetrahedra elements belonging to the cell surface, and looking up the location

of their centers of mass inside the bigger substrate tetrahedra. The corresponding maximal deformations were then mapped onto the surface. See Matlab Scripts in *Appendix 2* for the detailed calculations.

### Geometrical interpolation of cell and nucleus

To position of the cell and nucleus after stretching was calculated by interpolating all the points making up their meshes as described in section 2.6.2 for the interior points of the substrate mesh. See Matlab Scripts in *Appendix 2* for the detailed calculations.

## 2.7 Materials

Table 2.3: Materials, equipment, software

Fluorescent stainings & beads	
CellMask Deep Red Plasma membrane Stain	Life Technologies GmbH, Darmstadt, Germany
CellTracker Carboximethylfluorescein diacetate	Life Technologies GmbH, Darmstadt, Germany
Fluoro Max Dyed Blue Fluorescent Particles	Thermo Fisher Scientific, Waltham, MA, USA
Hoechst33528	Sigma-Aldrich Chemie GmbH, Steinheim, Germany
MitoTracker Red	Life Technologies GmbH, Darmstadt, Germany
Rhodamine Phalloidin	Life Technologies GmbH, Darmstadt, Germany
Media & buffer components	
DMEM - Dulbecco's Modified Eagle Medium	Life Technologies GmbH, Darmstadt, Germany
FBS - Fetal Bovine Serum	Life Technologies GmbH, Darmstadt, Germany
L-Glutamine	Life Technologies GmbH, Darmstadt, Germany
Penicilin/Streptomycin	Merck Millipore, Darmstadt, Germany
PBS - Phosphate-Buffered Saline	Life Technologies GmbH, Darmstadt, Germany
Williams Medium E	Sigma-Aldrich Chemie GmbH, Steinheim, Germany

## 2.7 Materials

---

---

### Drugs, proteins, transfection reagents

---

Collagen from rat tail tendon	Roche Diagnostics GmbH, Mannheim, Germany
Latrunculin B	Life Technologies GmbH, Darmstadt, Germany
Lipofectamine 2000 Transfection Reagent	Life Technologies GmbH, Darmstadt, Germany
Trypsin EDTA	Life Technologies GmbH, Darmstadt, Germany

---

### Microscopy & 3D Stretcher tools

---

8-well imaging $\mu$ -slide	Ibidi, München, Germany
30mm round cover slips	Menzel Gläser, Braunschweig, Germany
Anti-static pinzette	Life Technologies GmbH, Darmstadt, Germany
Screwdriver	Bauhaus, Heidelberg, Germany
Screwclamp	Bauhaus, Heidelberg, Germany
Sp5 TCS LSCM	Leica Microsystems, Germany
StageFlexer Membranes	Flexcell International Corp., Hillsborough, NC, USA

---

### Hardware, Software & Apps

---

Amira 4.11	Visualization Sciences Group, Berlin, Germany
Fluorescence SpectraViewer App	Life Technologies, Carlsbad, Ca, USA
ImageJ 1.44o	National Institute of Health, USA
Iphone 4 <sub>Pher</sub>	Apple, Cupertino, Ca, USA
MacBook Pro <sub>Eel</sub>	Apple, Cupertino, Ca, USA
Matlab R2011b	Mathworks
Papers 2.32	Mekentosj, Aalsmeer, The Netherlands
R 2.15.1	The R Foundation for Statistical Computing
Textmate, 1.5.11	MacroMates Ltd.

---

# 3

## Results

The results of this thesis are presented in four independent parts. In the first two sections the performance and robustness of the methods developed will be shown. As the main goals and the most important contributions of this work are in the developed methods themselves, and because of their novel nature, it is of importance to prove that both the experimental and the analysis workflows manage to accomplish their intended purposes. Therefore,

- 3.1 presents the results on the optimization of the *Nuclear compressibility* framework
- 3.2 serves as a step by step guide to the results of the complete framework development of the *3D Substrate Stretcher*.

Subsequently, the results of the application of these methods to perform comparative analysis in two different cell systems will be shown.

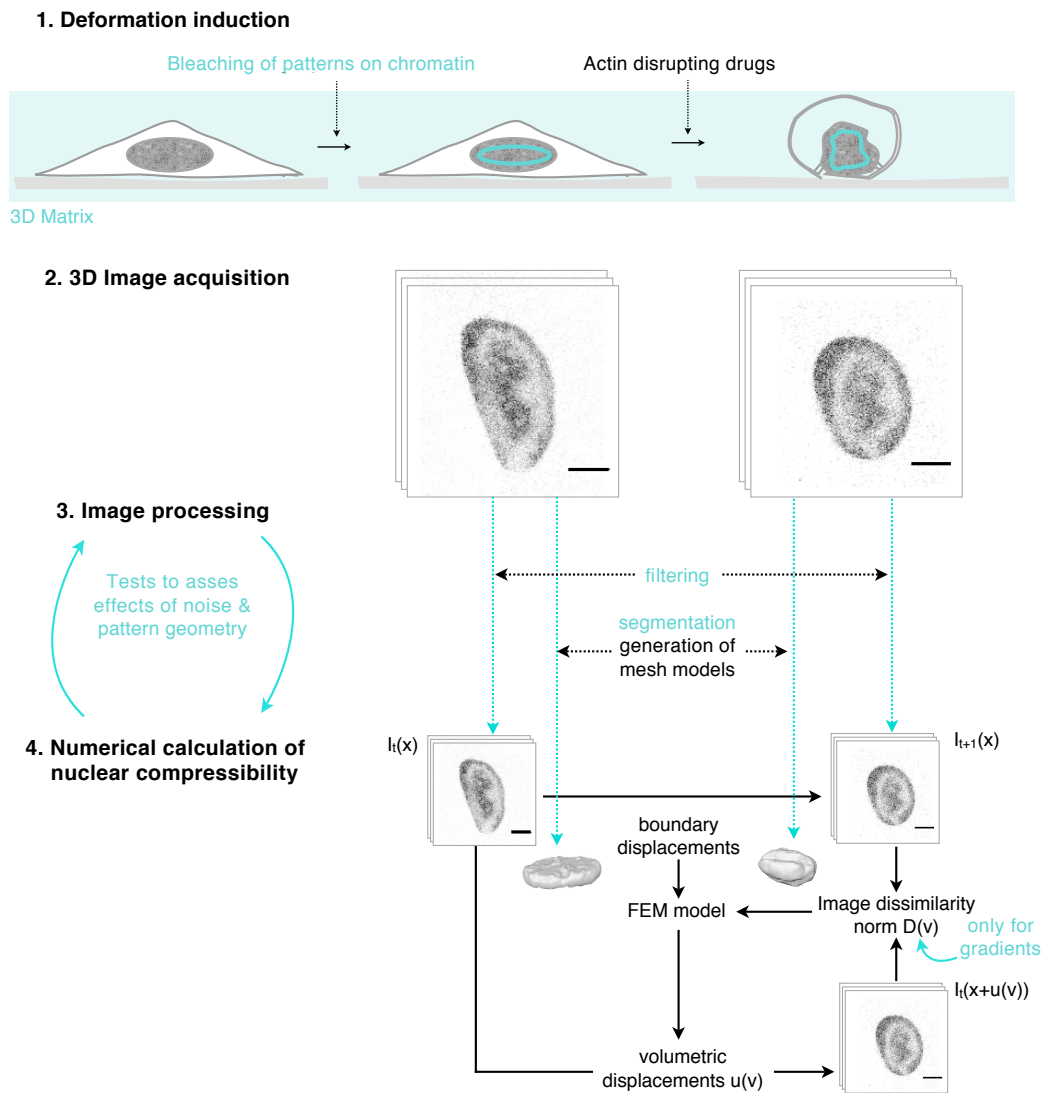
- 3.3 presents the results of the nuclear compressibility framework in wild type vs.  $LMNA^{-/-}$  primary mouse embryonic fibroblasts (MEFs), as a model system for nuclear fragility and proof of principle for this methods.
- 3.4 contains the results of the morphological and mechanical characterization of untreated vs. TGF- $\beta$  treated primary mouse hepatocytes (pmHCs), as a model system for dedifferentiation and malignant transformation.

### 3.1 Nuclear compressibility: optimization of the framework

The general image and model framework to measure nuclear compressibility comes from [Gladilin et al., 2010], where the idea of using cytoskeleton disrupting drugs to deform the nuclei and the numerical framework to determine nuclear compressibility from these image stacks was established and used to measure one single cell. A first attempt to apply this method to perform a comparative study between two cell phenotypes was performed in [Gonzalez, 2008, Gonzalez et al., 2009], however due to difficulties in the experimental setup and the low degree of robustness of the image-based framework towards experimental systematic noise, only 2-3 cells per condition were measured leading to no statistical significant results.

Therefore, an important part of this work was to characterize and optimize the image- and model based framework to allow the measurement of more cells to perform significant comparative studies between cell phenotypes. The enhancement of the method was conducted both experimental and computational. Insight gained from theory and from tests at the image processing level was utilized to modify the experimental setup. At the same time, analysis and modeling requirements were learned from the challenges imposed by the biological experiments.

**Fig. 3.1** shows an overview of the steps comprising the experimental and computational modeling workflow to determine the compressibility of the nuclear interior together with a summary of the parts where the previously developed method was enhanced. The workflow consists on: **1.** Inducing deformation of the fluorescently stained nuclei by cell rounding after application of cytoskeleton disrupting drugs. **2.** Acquiring 3D image stacks at different time points depicting the shape of the nuclei over time. **3.** Processing the image stacks to generate the depiction of the nucleus for each time points in two forms: As a filtered image stack depicting the nucleus as a function of image intensities  $I_t(x)$  and as a 3D mesh model of the nuclear surface. **4.** Determination of the compressibility of the nuclear interior in the form of the value for the  $\nu$  that better describes the deformation between time points  $t$  to  $t+1$  by comparing the image stack from the first time point deformed with different values for  $\nu : I_t(x + u(\nu))$  with the actual image stack of the subsequent time point  $I_{t+1}(x)$  as described in sec. 2.6.1.



**Figure 3.1: Overview of nuclear compressibility workflow and introduced enhancements.** Schematic overview of the steps comprising the nuclear compressibility framework with the enhancements to the method marked in blue. The method consists of **1.** The induction of nuclear deformation by application of cytoskeleton disrupting drugs. **2.** The acquisition of the 3D image stacks at different time points depicting the shape of the nuclei at each time point. **3.** The processing of the image stacks to generate the depiction of the nucleus for each time point in two forms: As a filtered image stack depicting the nucleus as a function of image intensities  $I_t(x)$  and as a 3D mesh model of the nuclear surface. **4.** The actual determination of nuclear compressibility  $[v]$  by comparing the image stack from the first time point deformed with different values for  $v$   $I_t(x + u(v))$  with the actual image stack of the subsequent time point  $I_{t+1}(x)$ . Scale bar = 5  $\mu\text{m}$ . Modified from [González Avalos et al., 2011].

### 3.1.1 Reducing error sources with image processing

As described in section 2.6.1, the calculation to determine the compressibility of the nuclear interior from the nuclear deformation microscopy series is based in the comparison of image stacks deformed artificially with the numerical framework  $I_t(x + u_{(\nu)})$  against image stacks depicting the actual experimental deformation  $I_{t+1}(x)$  (s. also **Fig.2.2**). The value for  $\nu$  which better describes the deformation of the nucleus for each time step  $t$  is found by minimizing the  $\nu$  dependent difference  $D(\nu)$  between image stacks:

$$\nu_{min} = \min(|D(\nu) = I_{t+1}(x) - I_t(x + u_{(\nu)})|) \quad (3.1)$$

This is valid for an ideal theoretical case, assuming that the difference between  $I_t(x)$  and  $I_{t+1}(x)$  is merely due to the deformation of the nucleus and that the relationship between the artificially generated image stack and the experimentally acquired image stack can be reduced to:

$$I_{t+1}(x) = I_t(x + u_{deformation}) \quad (3.2)$$

However, because of the nature of the experimental set-up, which has more causes for structural variations between the image stacks of two consecutive time points, this relationship has to be extended with several terms to accounting for different error sources:

$$I_{t+1}(x) = I_t(x + u_{total}) + I_s(x) \quad (3.3)$$

where,

$$u_{total} = u_{deformation} + u_{translation} + u_{ne} \quad (3.4)$$

and,

$$u_{translation} = u_x + u_y + u_z \quad (3.5)$$

with:

- $I_s(\mathbf{x})$ : statistical noise scattered as a consequence of the imaging process.
- $u_{translation}$ : movement of the cell (x, y, z translation) between time steps.
- $u_z$ : movement of the cell in z-direction causing intensity differences in the



z-slices among the time steps.

- $\mathbf{u}_{ne}$ : movement of structures in the nucleus e.g. nuclear bodies, which cannot be comprised by the description of elastic deformation

$\mathbf{u}_{translation}$  resulting from the movement of the cell, and consequently the nuclei, between acquisition time steps was eliminated computationally by registering the image stacks, mapping the nuclei onto each other (s. 2.5). In an attempt to reduce  $\mathbf{I}_s(\mathbf{x})$  and  $\mathbf{u}_z$  a filtering and a normalization step were performed, respectively. Although with this measures, the structural difference between images is significantly reduced, the method was still failing to find the correct value of  $\nu$  at levels of image noise equivalent to a gaussian noise with  $\sigma = 10$  (data not shown).

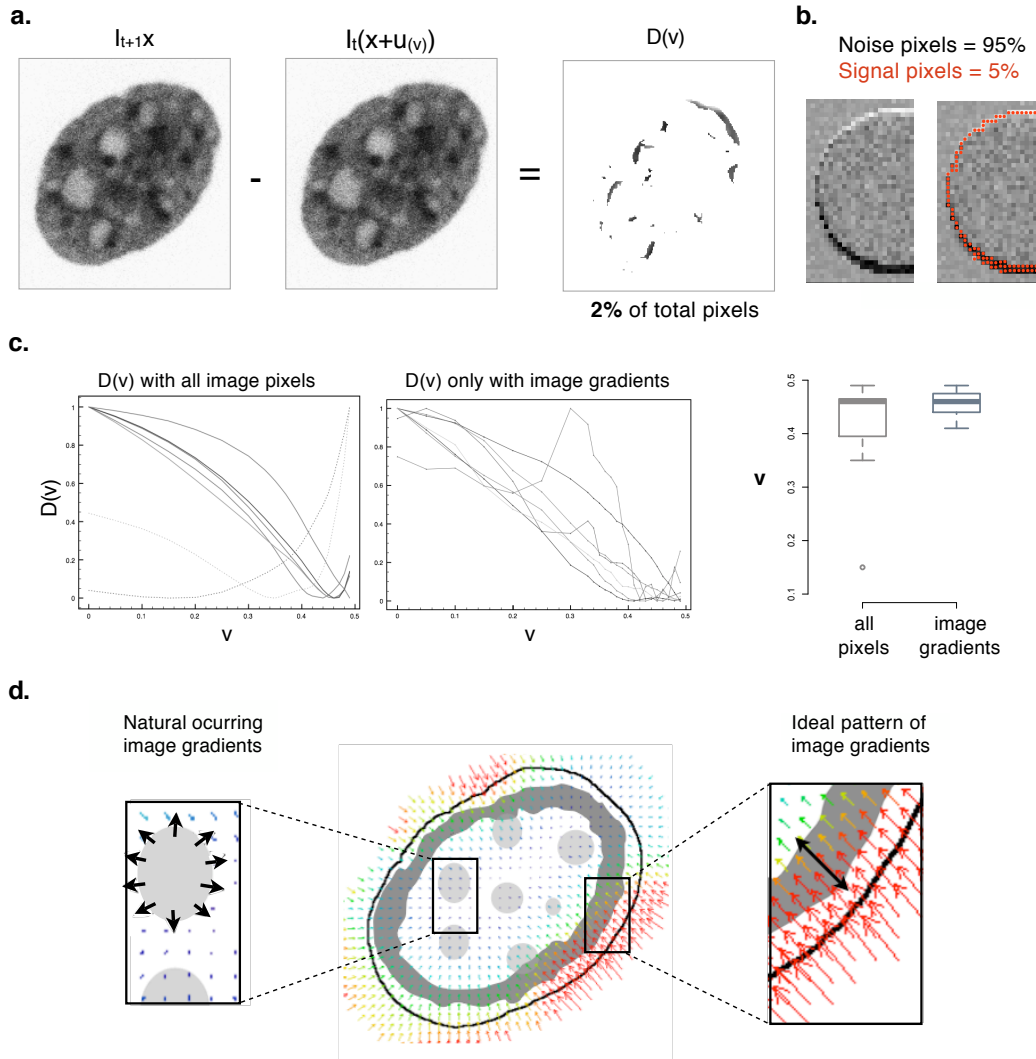
### 3.1.2 Influence of the amount of image gradient in the calculation of $\nu$

The big influence that statistical noise had in the calculation of  $\nu$  can be attributed to the fact that only image regions with strong image gradients contribute to the actual signal for the calculation and that the majority of the natural texture of the nucleus does not exhibit strong image gradients (Fig. 3.2 a,b).

The first solution approach to this problem was computational: by modifying the tool to only take into calculation regions with strong image gradients. With this step we ensure that only pixels relevant for the calculation are used and reduce the effects of statistical noise. An example of this reduction is shown in Fig. 3.2 c, where the same data is analyzed first with the tool taking all image pixels for the calculation of  $D(\nu)$  and then only taking into consideration the pixels of the image gradients. The measured values for different time points of the same cell change from  $0.41 \pm 0.12$  to  $0.46 \pm 0.02$ , which means a reduction of the statistical dispersion (measured as the standard deviation) of the values from 30% to only 5%.

### 3.1.3 Suboptimal geometry of the nuclear patterns

In the natural texture of the nuclear interior the bright structures contributing to the image gradients arise by the presence of nuclear bodies, most notably the nucleolus and chromocenters. This fact was problematic for two reasons. First, these nuclear bodies have been shown to have some degree of non-elastic movement [Gonzalez, 2008], which means their movement between time steps is known to



**Figure 3.2: Influence of image gradients magnitude and orientation in the calculation of  $v$ .** **a.** In the calculation of the image difference ( $D(v)$ ) between the deformed and the actual image stack of the next image step, only pixels with strong image gradients contribute to the actual signal. In the case of the the patterns in nuclear texture forming with the  $H_2B$ -GFP staining, these pixels are only around 2% of the total image pixels. **b.** The rest of the pixels just adds to enhancing the statistical noise because. **c.** By changing the analysis tool to only take into consideration pixels from image gradients, the statistical dispersion of the measured values is reduced significantly. **d.** Schematic representation of a cell nucleus with naturally occurring intensity gradients (light grey dots) and image gradients from bleached patterns (dark grey stripes). Color vectors represent image displacements, black arrows indicate the intensity gradient. The naturally stained structures (e.g., nuclear bodies) are mainly concentrated around the center of the nuclei, where small displacements and varying orientation of the image gradient (black arrows) are not optimal for the parameter estimation (zoomed left inlet). By bleaching circular stripes near the nuclear boundary, image gradients with parallel/antiparallel orientation to the displacement are generated (zoomed right inlet). *Modified from [González Avalos et al., 2011].*

be not only because of the deformation of the nucleus. The second reason is a problem of the pattern geometry. From theory, specifically from equation 2.4, follows that parameter estimation depends not only on the magnitude of the local gradient and the displacement vector, but also on their relative spatial orientation to each other. Ideal conditions for parameter estimation are given in regions with strong local image intensity gradients and large displacements that are oriented parallel or antiparallel to each other.

As the deformation field of the nuclei after drug induction goes normal to the nuclear boundary (**Fig. 3.2 c**, color arrows), the ideal geometry of image gradients for the calculation of  $\nu$  would be peripheral concentric stripes near to the nuclear boundary, where the magnitude of the deformation is the largest (**Fig. 3.2 d**).

#### 3.1.4 Correct geometry of image gradients improves the calculation of $\nu$

To measure the dependency of the method's accuracy on the geometrical patterns of the nuclei, we evaluated the framework's performance on artificial images depicting a shape similar to a nucleus with different geometry of patterns and different degrees of noise.

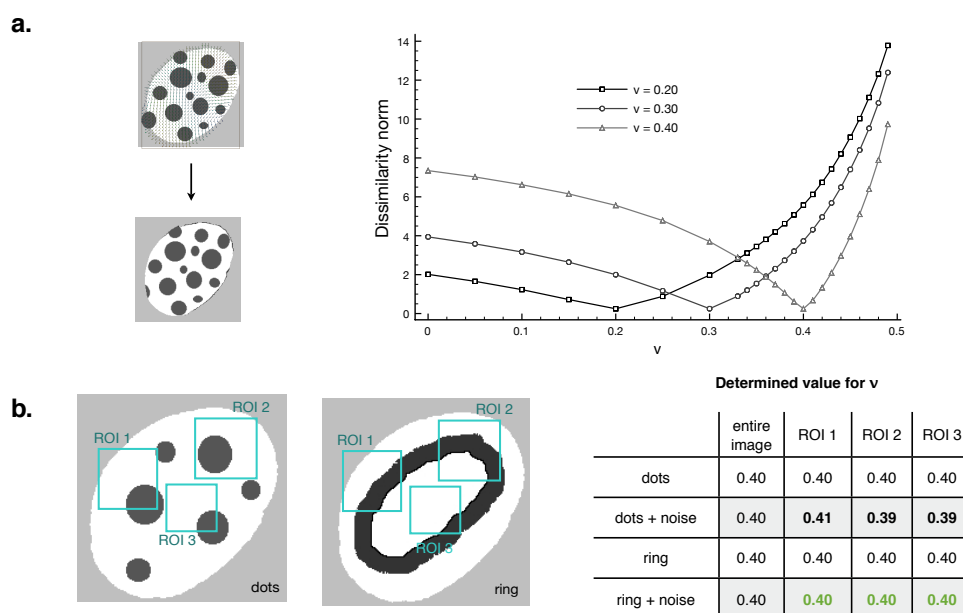
The evaluation scheme consisted of two basic steps (**Fig.3.3 a**):

- Deformed images were computed with a known  $\nu$  value.
- $\nu$  was determined from the original and deformed image pair using the numerical framework described in section 2.6.1.

Experimental results with noise-free images showed that the framework correctly predicts  $\nu$  values for both of the image intensity patterns used (**Fig.3.3**). Addition of stochastic noise hampered the accuracy of the prediction in the case of the dot-like patterns resembling the naturally occurring appearance of the nuclear interior (**Fig. 3.3 b**). However, introduction of peripheral concentric stripes with parallel orientation between the image intensity gradient and the displacement field helped to increase the accuracy of the framework predictions even in the presence of a substantial noise level (s. table in **Fig. 3.3 b** green values).

#### 3.1.5 Bleaching patterns on the nuclei improves accuracy

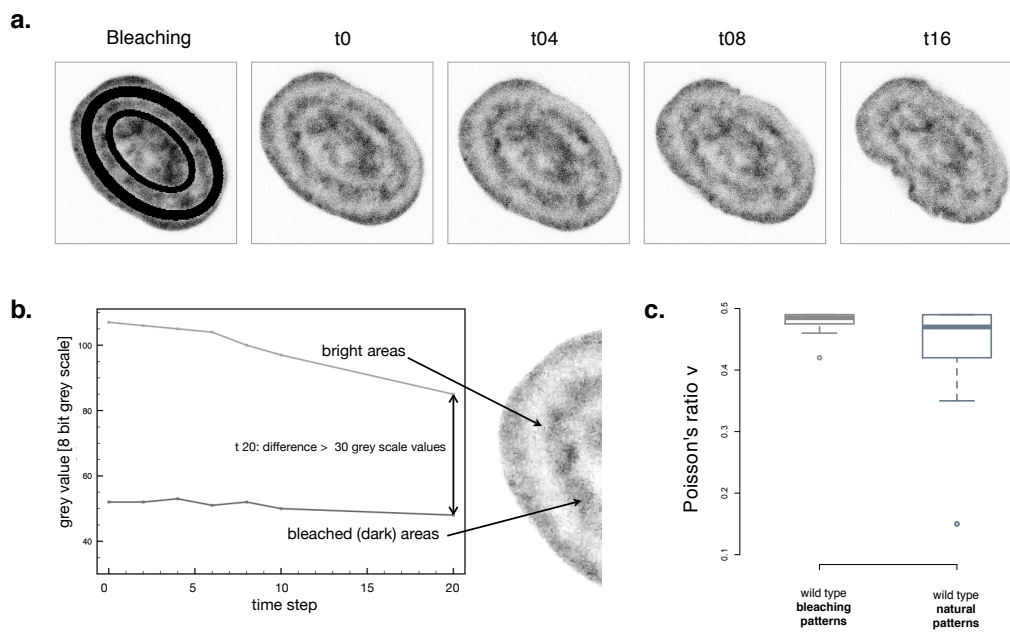
After assessing the importance of the correct geometry of the image patterns for the calculation of  $\nu$  and establishing that the natural occurring patterns are not



**Figure 3.3: Testing the influence of image gradient geometry on the accuracy in the calculation of  $\nu$ .** **a.** Correct  $\nu$  values are determined from the minima of the dissimilarity curves  $D(\nu)$  between original and deformed images. **b.** Images with different patterns (circles and ring) were deformed with a known value of  $\nu = 0.40$  and the framework was used to determine  $\nu$  for the entire images or using different regions of interest (ROI 1-3). As seen in the table, accuracy of the prediction is hampered when stochastic noise is added to the images in the case of dot-like patterns resembling the naturally stained intranuclear structures (s.  $\nu$  bold values in table). The circular ring near the nuclear boundary helps to generate more pixels with parallel/antiparallel orientation of non-vanishing image gradient and displacement vectors, and consequently, to increase the accuracy of the predictions even in the presence of a high-level additive noise (s.  $\nu$  green values in table). *Modified from [González Avalos et al., 2011]*

optimal for the framework, we decided to introduce artificial patterns onto the nuclei by bleaching the GFP staining the nuclei. Taking advantage of the fact that the fluorescent proteins were tagged to the core histone  $H_2B$ , which as a part of chromatin is known not to diffuse in small time scales [Abney et al., 1997, Beaudouin et al., 2006], the bleached patterns were expected to be maintained in the nuclei. Indeed, they were: after bleaching the patterns into the nuclei, they were maintained for the the whole duration of the imaging session (up to 4 hours) if the nucleus was not imaged again.

A problematic issue in the maintenance of the patterns was the general bleaching of fluorescent proteins caused by the acquisition of the time series. This had the effect that the difference in intensity between the bright areas (not previously bleached) and the dark areas (previously bleached) was reduced and the patterns



**Figure 3.4: Bleaching patterns on fluorescently stained nuclei.** **a.** Bleaching patterns on the nuclei reflect the deformation of the nuclei **b.** and are conserved over up to 20 imaging time points despite further bleaching by the image acquisition procedure. **c.** The use of bleaching patterns reduces the statistical dispersion of the measured values significantly.

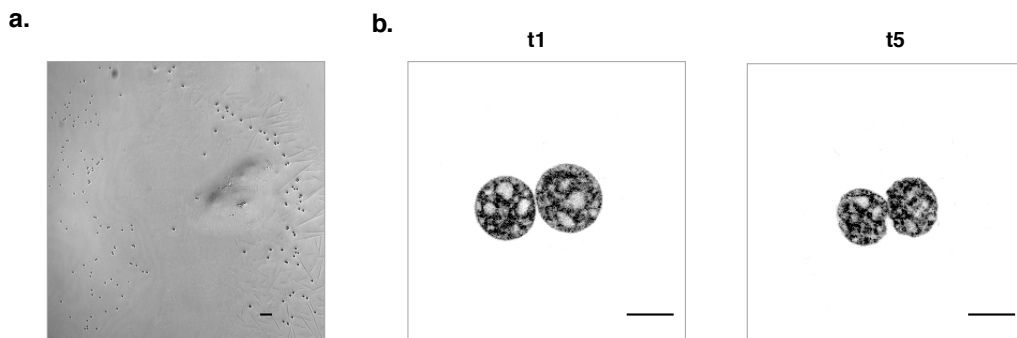
were lost. This was observed when using mCherry-H<sub>2</sub>B, where patterns were lost after 3-4 time points. By changing to H<sub>2</sub>B-GFP the difference between bleached and unbleached areas was maintained for over 20 time points (**Fig. 3.4 b.**) With this, the change in patterns reflected the deformation of the nuclear interior over time (**Fig. 3.4 a.**).

The advantage of using the bleaching patterns in the calculation of the  $\nu$  becomes evident when comparing the results from the analysis of data sets with and without bleaching patterns. The use of bleaching patterns reduces the statistical dispersion of the measured values significantly, giving a more consistent and accurate value (**Fig. 3.4 c.**).

### 3.1.6 Adapting the nuclear compressibility framework for 3D

Because the experimental framework to induce nuclear deformations by disruption of the actin cytoskeleton works completely without direct mechanical contact, it could be adapted to work with cells embedded in the 3D collagen matrix. The only difficulty arose in finding a proper concentration for the first collagen

layer to keep the cells under the working distance of the 63x objective. Tests, where different concentrations of collagen with beads were used for the first layer (Fig. 3.5 a.) revealed 85  $\mu\text{l}$  per well to be the most suitable concentration in which cells were fully embedded in the matrix and still completely visible. With this concentration it was possible to acquire image stacks depicting the deformation of the nuclei at good resolution (Fig. 3.5 b.). The fact of having the cells embedded in the matrix even brought the advantages of having them immobilized in the z-direction and in enhancing the time for the actin-disrupting drugs to act.



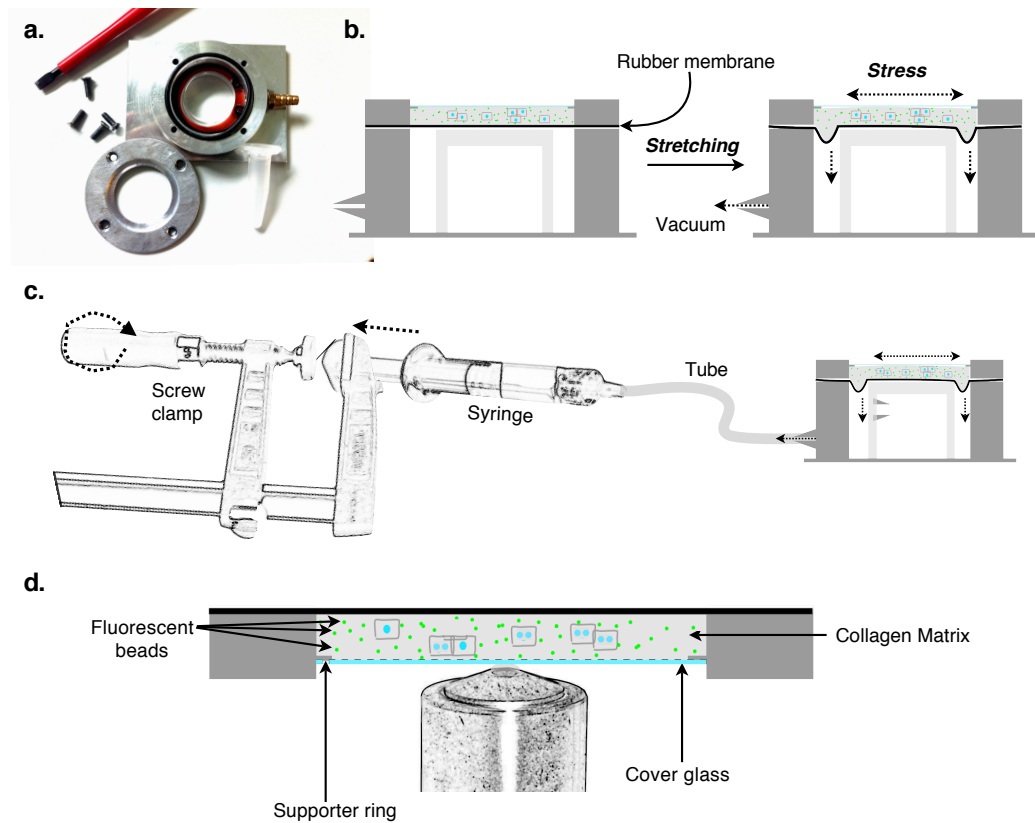
**Figure 3.5: Adaptation of the nuclear compressibility experimental workflow for the use with 3D substrates.** a. Transmission image of a cell and beads embedded in a collagen matrix to test the maximum amount of collagen that could be used to build the first collagen layer. An amount of 85  $\mu\text{l}$  per well resulted to be the most suitable set up, where the collagen covers cells and beads and the top of the sandwich is still visible with the LSCM. b. Examples of image stacks depicting nuclear deformation of a cell embedded in the collagen matrix and treated with trypsin shows how the experimental workflow is suitable for experiments in 3D. Scale bars = 10  $\mu\text{m}$ .

## 3.2 The 3D substrate stretcher

The idea to work with planar substrate stretchers arose in the search for experimental methods with which deformations on the cell and nuclei could be applied in a more controlled manner. From the many options discussed with E. Gladilin, we decided to start developing the planar stretcher because of the clear advantage of permitting a mostly planar (xy) strain application, as opposed to the cytoskeleton disruption experiments where the shift in z-direction was complicating the analysis. Also, deformations of the the cell and cellular structures can be put into relation to deformations of the marked substrate. Furthermore, the indirect strain application by deformation of the substrate would allow us to observe nuclear deformations in true physiological conditions i.e. with the nucleus completely embedded into to cytoskeleton.

The substrate stretcher consists of a small aluminum chamber that enables the biaxial stretching of cells growing inside a 3D substrate matrix attached to a deformable silicone membrane (**Fig. 3.6 a.**). The aluminum chamber is based on the *StageFlexer* model by *Flexcell Int.* [Wall et al., 2007] where a silicon membrane is placed on top of a plastic loading station and clamped at the sides by firmly fixing a metal top lid fixed with screws. When air is taken out of the chamber the membrane is deformed downward across the loading post imparting biaxial strain to the membrane center where the cells are placed (**Fig. 3.6 b.**). Air is pulled out with a common plastic laboratory syringe attached to the chamber through a rubber tube. To stabilize the stretched position with this vacuum-controlling device the syringe was attached to a screw clamp (**Fig. 3.6 c.**).

Several further technical modification had to be introduced to the chamber to allow the acquisition of high resolution confocal microscopy images. The original chamber setup was designed to be used in an upright position, imposing the difficulty to look at the cells through the layers of the glass loading station and the silicon membrane when using an inverse microscope. At the same time the chamber was too large to be used with an upright microscope. For these reasons the chamber was positioned upside-down and an extra metal lid was designed and produced at the *DKFZ precision mechanics lab* to reduce the distance between cells and microscope to the required objective working distance. A fine 200  $\mu\text{m}$  supporter ring was added to the newly designed lid to be able to protect the membrane with



**Figure 3.6: Development of the substrate stretcher experimental setup.** **a.** The substrate stretcher is a small aluminum chamber, in which a rubber membrane is clamped at the edges but resting on a plastic station in the center. **b.** Upon vacuum induction inside the chamber, the membrane gets pulled down to the sides and stretched at the center where the cells are sitting. **c.** In order to stabilize the syringe position, vacuum control was achieved through turning of the screw-clamp attached to it. **d.** To enable the acquisition of high quality images, the chamber is mounted upside down at the microscope. A special slim support ring was built to support the glass cover slip and at the same time retaining the cells in enough medium to survive the imaging sessions

a thin cover-glass without it to be in direct contact to the cells - squeezing them (Fig. 3.6 d.). The last important modification was to reduce the final weight of the metal chamber for it to be under the 150 g allowed on the microscopy stage.

### 3.2.1 Going 3D

Silicone membranes for the chamber are sold from *FlexCell* coated with different adhesive proteins. However, in the need to provide a more physiological substrate in three dimensions for the cells to attach while being stretched, we enhanced this method by coating the cells with ca. 80  $\mu\text{m}$  3D collagen sandwiches as described



in sec. 2.1

As perviously mentioned, a clear advantage of the substrate stretcher is the ability to mark the substrate to use it as reference material to put in relation to the cellular deformation. For this purpose 1  $\mu\text{m}$  fluorescent beads were embedded into the collagen preparations used for both of the soft collagen layers. A final bead concentration of 1:200 was found to fulfill the required conditions for the beads to not form many clusters but being close enough to enclose cells and sample the space with enough accuracy for further analysis.

### 3.2.2 Live 4D imaging in the 3D stretcher

With the technical modifications introduced in the stretching chamber, it was possible to acquire images at the confocal microscope with enough resolution and quality for further analysis, while at the same time keeping cells in proper conditions for life cell imaging. After the chamber size was adjusted and the weight of the chamber was reduced, the stretching chamber could be mounted up-side down at the microscope stage without damaging the piezo-piece.

The introduction of the holding ring for the cover glass enlarged and stabilized the space between cells and glass, providing the cells with more space so that they stopped being squeezed by the glass (**Fig. 3.7 a.**). The extra space was also important for the quantity of cell medium that could be added to the cells to keep them in viable conditions. In the absence of mechanical or phototoxic stress, cells were viable for several hours inside the chamber.

Next, the 3D collagen matrix had to be optimized so that i. the layers were thick enough for the cells to feel the 3D environment (**Fig. 3.7 b.**) but at the same time ii. the layers, in particular the second layer closer to the glass and the objective, had to be thin enough to allow the acquisition of the whole substrate and cell volume within the working distance of the objective. With final collagen volumes of 250  $\mu\text{l}$  for the first and 200  $\mu\text{l}$  for the second layer, a complete volume of approximately 80-100  $\mu\text{m}$  could be acquired with the 40x objective (**Fig. 3.7 c.**).

The final technical problem was the stabilization of the stretched position. A disadvantage of using a deformable membrane (or substrate) as scaffold for 3D imaging is that fluctuations in z-position can occur during the acquisition of the z-stacks. An uncommon problem, not usually encountered when using stiff glass

or plastic substrates to seed the cells. Within the stretcher chamber, small air fluctuations occurred after air was pulled out of it with the syringe. The minimal air fluctuations unnoticed at the scale of the syringe (as no change in the position of the syringe could be observed) manifested in movements of the membrane to put to 30  $\mu\text{m}$  (**Fig. 3.7 d**). This problem was circumvented by locking the syringe in a stable position and tightly regulating the pulling of air with the screw clamp.

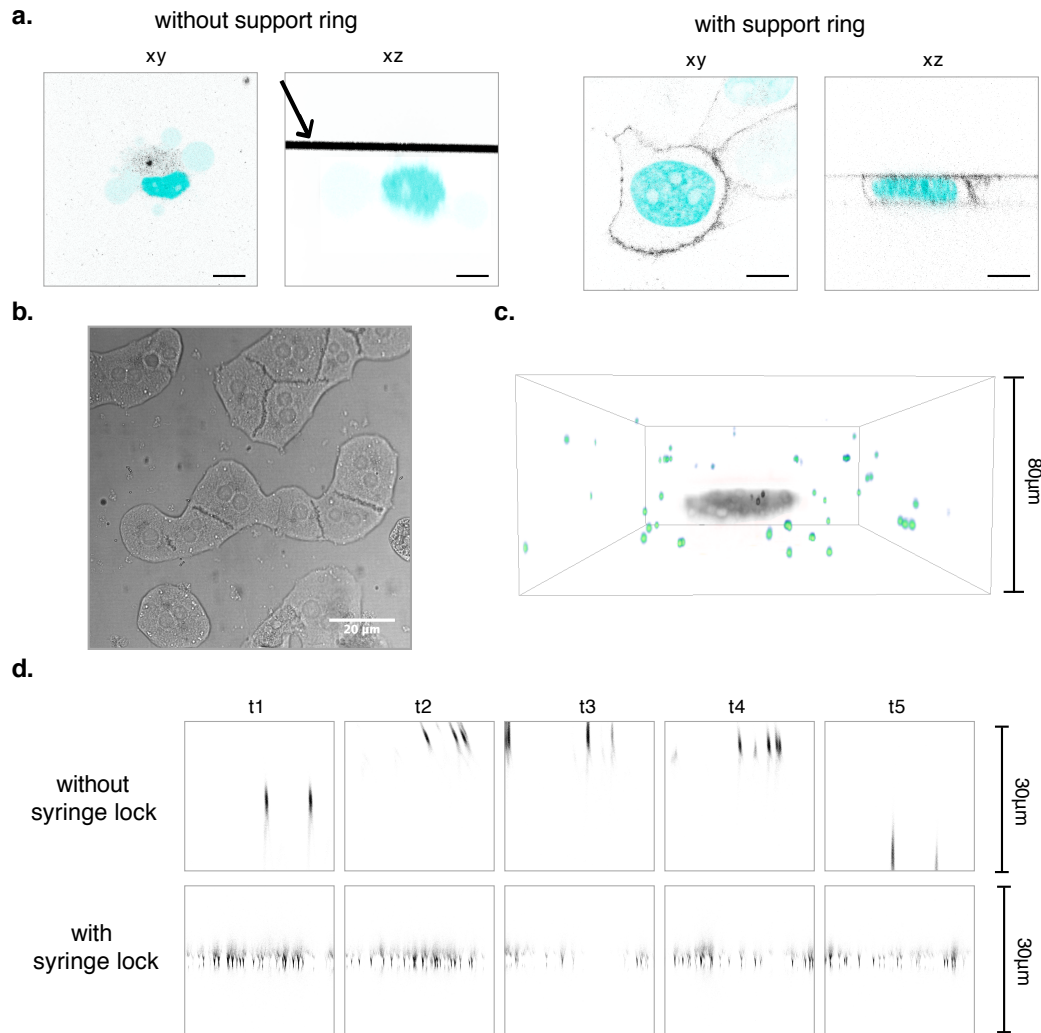
Several stainings and staining combinations were tried out for visualizing cellular structures. Essential for the analysis were i. the beads, as markers for the substrate deformation ii. a marker for the cell iii. a marker for the nucleus. In addition, it was important to keep the number of lasers used for fluorescent excitation low to reduce photo-toxicity. Therefore, dyes with the same excitation wavelengths and separable detection wavelengths were preferred. In primary cells, where regular transfection was extremely inefficient (data not shown), the options were further reduced by the availability of fluorescent staining suitable for life cell imaging. The best working combination to reduce phototoxicity and still have clean separable structures for beads and nuclei was found in the use of blue fluorescent beads and Hoechst to stain the nuclei. Both of these fluorescent dyes have wide emission curves after excitation with the 405 nm laser. However, the dyes of the fluorescent beads emitted much stronger at the same laser power. Taking advantage of these features, different photomultipliers with adjusted gain were used to separate the beads signal from the nuclear signal (**Fig. 3.8 a**. beads & nuclei).

CellMask was a suitable marker for the cell, ideally emitting in the far red area so that the signal was completely separated from beads and nuclei. However, this stain had the disadvantage of also staining all cell debris coming from dead cells in the vicinity. This was of particular annoyance for the segmentation of individual cells (s. section 2.5). Therefore, an even better marker for the cell surface was found in the use of soluble GFP monomers. Although using fluorescent proteins involved the extra step of transfection or viral transduction, the enhancement of the signal-to-noise ratio in the cell staining was an essential improvement (**Fig. 3.8 a**.: compare cell signal in the first and second row<sup>1</sup>).

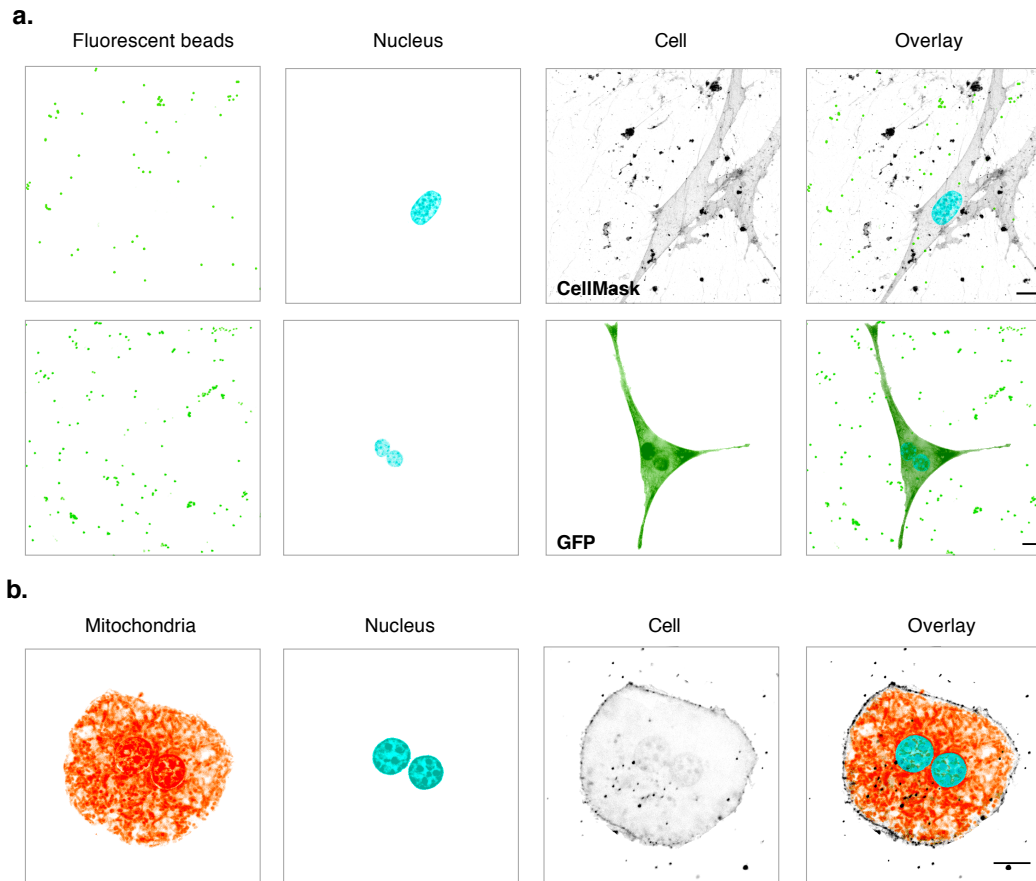
In an attempt to mark more structures in the cell interior to gain more information about strain propagation inside the cells, Mitotracker stainings were tried out to mark the mitochondria (**Fig. 3.8 b**.). Mitochondria displacements in the

---

<sup>1</sup>..and then imagine trying to segment the structures



**Figure 3.7: Live cell imaging and stretching in 3D.** **a.** Before the introduction of the 200  $\mu\text{m}$  holding ring, cells didn't have enough medium or space inside the chamber and were squeezed by the cover glass (black arrow). The space gained by the introduction of the holding ring gave the cells space to survive with enough medium. **b.** The collagen layers were thick enough for pmHC cells to develop organotypical structures only forming in 3D cultures, probing that the stretcher provides a suitable 3D environment. **c.** With the optimization of the collagen volume for the sandwich layers a volume of approximately 100  $\mu\text{m}$  with cells embedded in the middle could be imaged **d.** Small fluctuations in the vacuum inside the chamber caused relatively large movements in  $z$  after stretching. This problem was solved by the syringe stabilization with the screw-clamp. Scale bar = 10  $\mu\text{m}$ .



**Figure 3.8: Stainings for live cell imaging at the 3D stretcher. a.** Three structures had to be made visible for further analysis: the fluorescent beads embedded in the substrate, the nuclei and the cells. Although the blue fluorescent beads and the nuclei had similar emission wavelengths, their signals were separated by adjusting the gain in different photomultipliers. Two ways of marling the cells were tried out: CellMask or soluble GFP. GFP labeling had the advantage of staining only the inside of living cells. CellMask had a better emission wavelength in the far red region. However, it had the drawback of staining all the dead cells in the vicinity, a fact that complicated the segmentation. **b.** Mitochondria would have been useful markers for tracking the deformation in the cell interior. But although mitochondrial staining worked was possible with Mitotracker stains, cells weren't able to resist the phototoxicity caused by so many stains and lasers and died quickly. Scale bars = 10  $\mu\text{m}$ .

cellular interior have been shown to correlate with the cytoskeleton [Lombardi et al., 2011a] and would have been an interesting marker to study mechanotransduction in the cell interior. However, cells with the extra mitochondrial staining died quickly presumably of phototoxicity.

### 3.2.3 Cellular and nuclear surface reconstructions

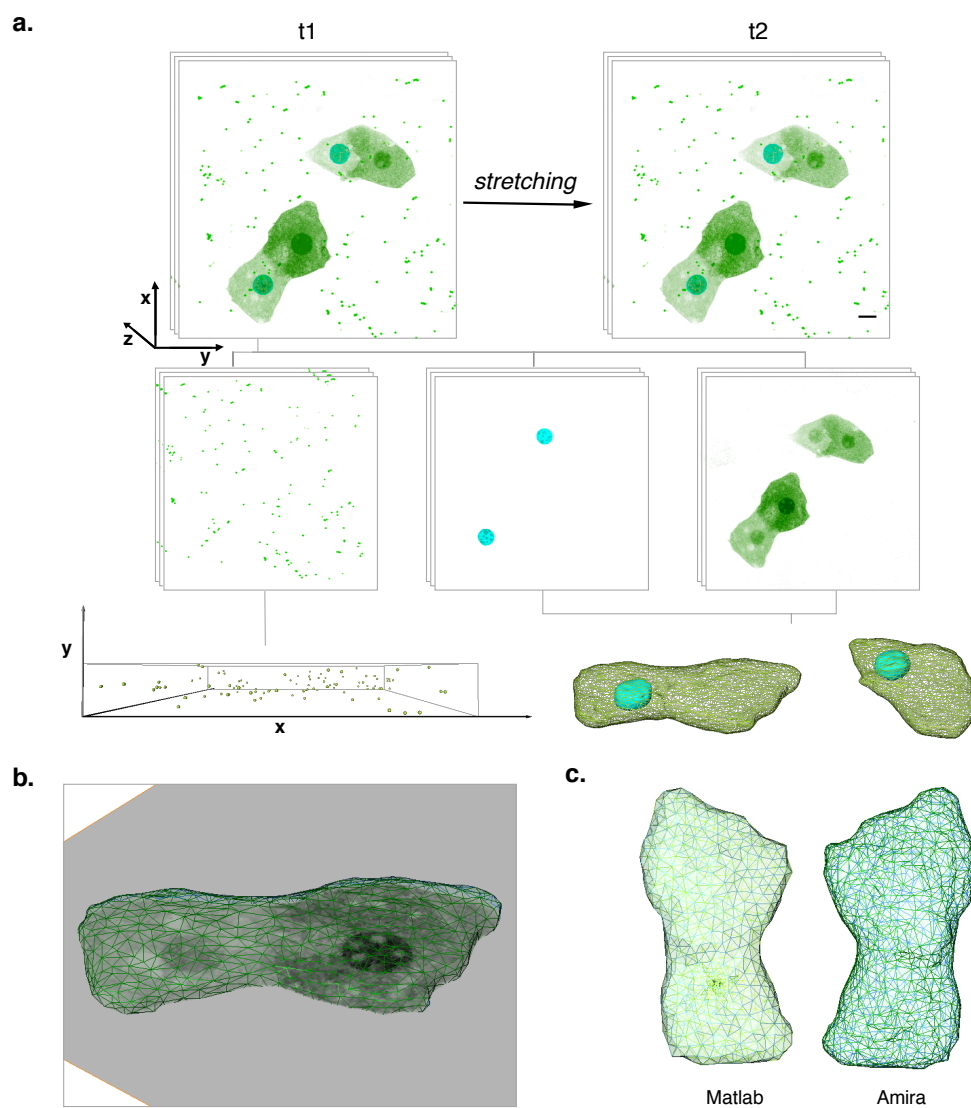
With the selection of fluorescent stains for cell and nucleus, 3D image stacks were acquired before and after stretching. Two types of information were extracted from the acquired channels. The beads intensities were processed as described in section 2.5 and used to describe the substrate deformation as explained in the next section. The other two channels with the stained nucleus and cell were used to generate the 3D surfaces depicting the shapes of the cells and nuclei (**Fig. 3.9 a.**). As the whole mechanical analysis is based on the change in shape of these surfaces, their accurate generation was a crucial step in the analysis of the time series. **Fig. 3.9 b.** shows how, after automatic segmentation of the GFP signal, the generated surfaces indeed match very well the cell contours of the original image stack. Correct surfaces were generated by both the programs employed (Matlab and Amira). Compatibility of these meshes was important to perform the two types of mechanical analysis (**Fig. 3.9 c.**). Because of the way in which the images were read in the different programs, the generated meshes appeared mirrored to each other.

### 3.2.4 Description of 3D substrate deformation

#### Reconstruction of 3D substrate from beads coordinates

The main advantage of the 3D stretching framework is the ability to map the local deformation of the 3D substrate on the cells embedded in it. And as substrate deformation is described by calculating the beads displacements i.e. by mapping their positions between time points, the accurate extraction of the individual bead coordinates was an important requirement.

The xyz coordinates for each bead were extracted with the 3D object recognition plugin in ImageJ. This plugin works by first segmenting the stacks and then joining the segmented structures along the slices of the z-stack. Once the objects are identified, several features can be outputted as a result. Because of the high signal-to-noise ratio resulting from the bright dyes incorporated in the beads, the



**Figure 3.9: Volumetric surface reconstruction from cellular structures.** **a.** Surfaces are extracted from the 3D Image stacks after segmentation either with Amira or Matlab. **b.** Because all the subsequent analysis bases on these surfaces, it is of extreme importance that the surface matches the cell contour. **c.** Surfaces in Matlab and Amira were constructed equally well, just because of the way the coordinates are read they appear as mirrored. Scale bar = 10  $\mu\text{m}$ .

1  $\mu\text{m}$  beads were easily separated from the background and identified as objects (s. 2D z-projections in **Fig. 3.10 a.**). The object identification is dependent on two parameters set manually by the user: the intensity *threshold* for segmentation and the *size* of the objects. Because the imaging conditions between acquisition time points were not necessarily kept constant, these parameters had to be set individually for each image stack.

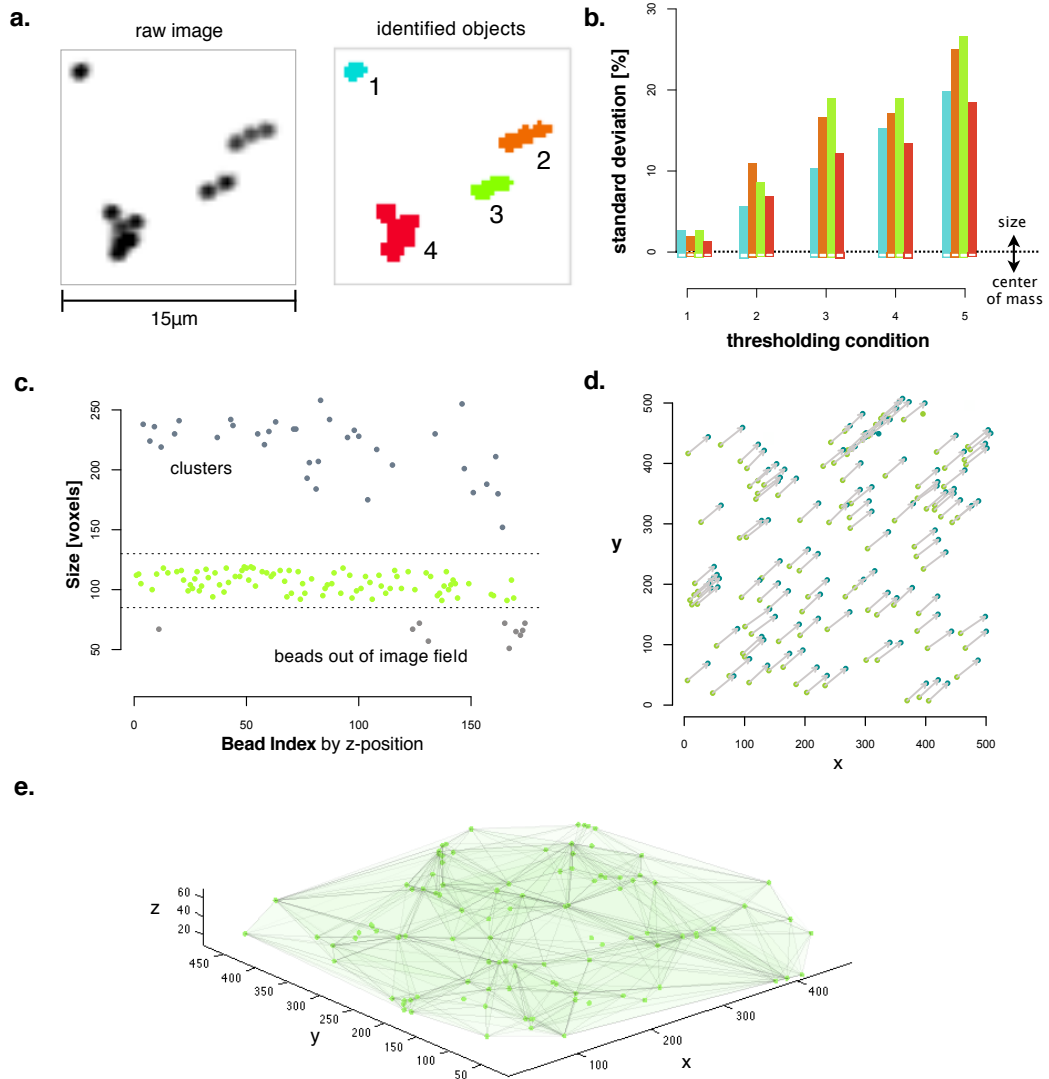
**Fig. 3.10 b.** shows the sensitivity test of the beads coordinate calculation towards variations of parameters within the segmentation algorithm. As it can be seen, the sizes of the identified objects are completely dependent on the segmentation threshold because they change significantly in the different thresholding conditions. However, determination of the coordinates of the *center of mass* of the identified objects - which is used as the final bead coordinate - stays very robust towards variation of the threshold.

Although threshold dependent, the determined object size was very consistent for all the individual beads in the image. This was used to select individual beads fully embedded in the substrate by excluding beads out of the image field (which had a smaller size) and bigger beads clusters (which were significantly bigger) (**Fig. 3.10 c.**).

By setting up these selection criteria, we established an accurate and robust method to extract the beads positions. The coordinates were subsequently loaded into *R*, where the displacements of corresponding beads between the two time points were calculated as described in section 2.6.2. An example of identified beads and their displacements is shown projected in **Fig. 3.10 d.** The calculated beads coordinates and displacements were then loaded into *Matlab*, where the points were joined into a volumetric mesh of tetrahedra (**Fig. 3.10 e.**) with which the substrate deformation could be calculated.

### Substrate homogeneity analysis

The main working assumption of the 3D substrate stretcher is that we can characterize the substrate deformation by tracking the displacements of the individual beads embedded in it. This is true if the beads are completely embedded in the matrix and move accordingly with it. If, for any reason, beads are somehow restricted in their movement e.g. if they get trapped in between cell debris or slide in between the matrix pores, their displacement would not reflect the deformation



**Figure 3.10: Detection and sorting of beads between adjacent time points.** **a.** The accurate calculation of the beads positions is an important prerequisite for the analysis 3D stretcher. The most important parameter for object identification is the intensity threshold used to segment the objects, which is set manually and can vary between image stacks. However, unlike the size of the identified object, which varies with the different thresholds, the center of mass stays constant regardless of the parameters chosen. **c.** The calculated size of the objects serves as an efficient filter for individual beads suitable for the calculation of the substrate deformation. Because of the small variation in size, considerably smaller objects belong to beads out of focus and bigger objects belong to beads clusters. **d.** With the beads coordinates in both time points, beads were mapped into each other and displacements were calculated in R. **e.** Finally, the point cloud of beads coordinates was connected into a tetrahedral mesh in Matlab.



of the substrate and the strain calculation would be biased.

To identify beads that were not moving homogeneously with the deformation field of the substrate, we developed a script to test the continuity or homogeneity of the local deformation field. Under the working hypothesis that the substrate features a bulk strain to the membrane stretching and that on a big scale it moves homogeneously in a particular direction. If the volume is sampled densely enough to capture local homogeneities, we should be able to determine the displacement of a particular bead by the displacement of neighboring beads. To implement this we looked for all the beads with enough neighbors i.e. beads lying in the interior of the substrate (**Fig. 3.11 a.**), estimated its displacement by interpolating it (as described in sec. 2.6.2) (**Fig. 3.11 b.**) and calculated the error in the interpolation by comparing the interpolated displacement to the actual displacement.

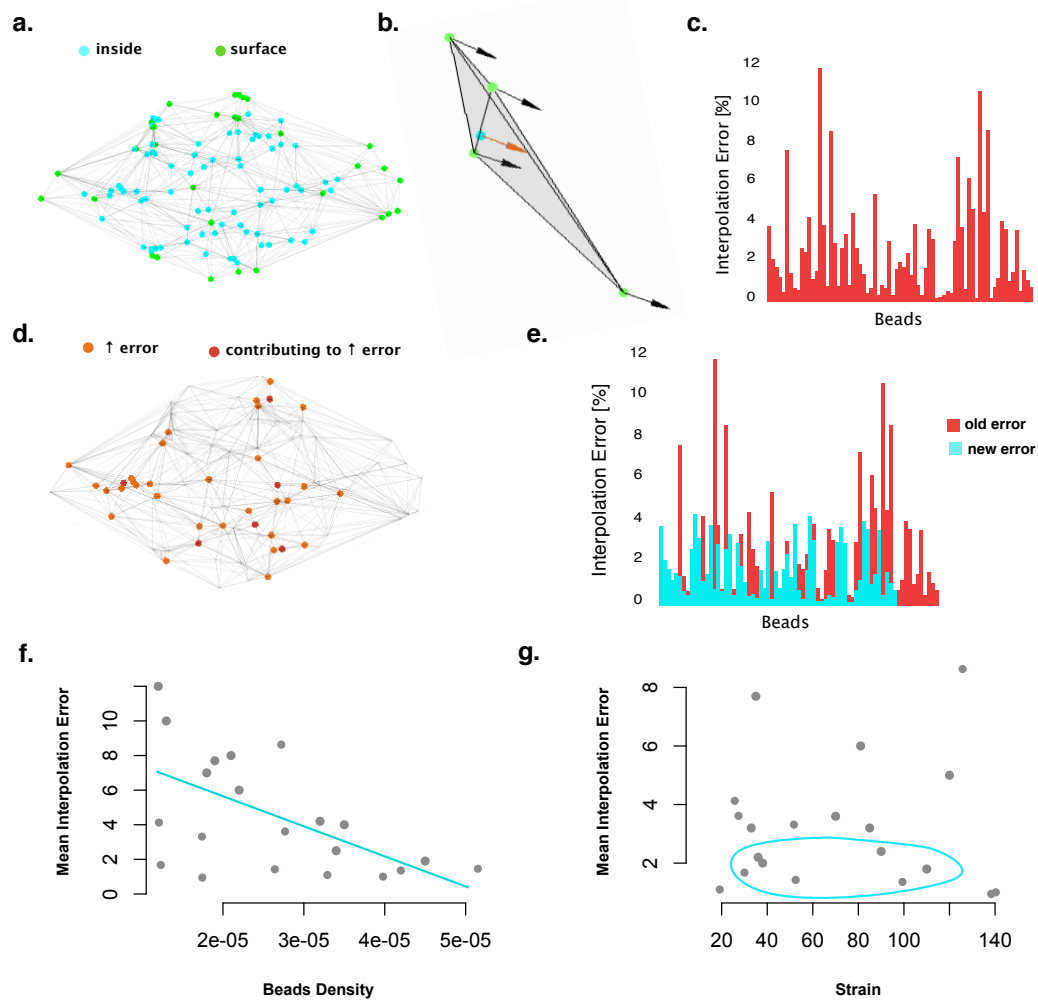
Accuracy in the interpolation error also plays an important role for the mapping of strains on cells, where the displacements for the cell points have to be interpolated from the substrate with a certain accuracy.

For most of the beads, the linear interpolation can accurately predict the actual bead displacements with a mean error of around 2% (**Fig. 3.11 c.**). This translates into an accuracy of under 1 micrometer. In most of the data sets, around 5% of the beads exhibited a disproportionately high error of over 10%. The error in interpolation could be due to two reasons: 1. that the bead being interpolated behaved randomly and/or 2. that one of the beads used for the interpolation was behaving randomly. Indeed, after identifying the source of error (**Fig. 3.11 d.**) and removing the problematic beads, the whole error was reduced (**Fig. 3.11 e.**).

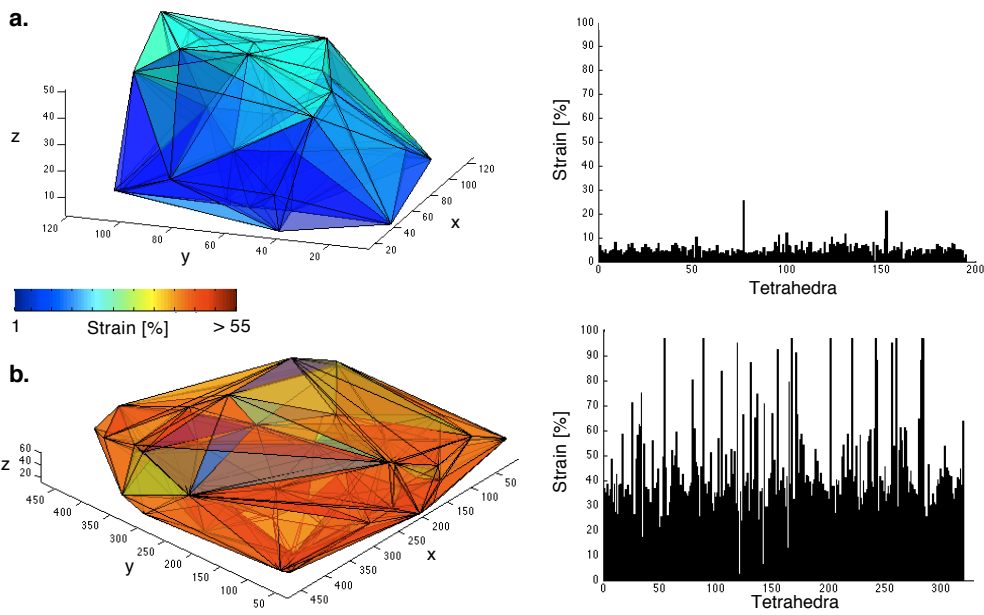
The mean interpolation error is negatively correlated to the the density of the beads inside the matrix (**Fig. 3.11 f.**). Meaning that a certain spacial sampling is necessary to correctly describe the substrate and pointing to local inhomogeneities in the substrate.

### 3D strain assessment

Reconstituted collagen gels have been shown to exhibit a *non-affine* mechanical behavior [Chandran and Barocas, 2006], meaning that the local behavior of the entangled filaments is not completely homogeneous or *affine* with the macroscopic deformation. Therefore, it should not be assumed that the cells within the matrix are exposed to the macroscopic or *bulk* strain of the substrate as a whole. Instead



**Figure 3.11: Assessing local substrate homogeneity through interpolation of beads in substrate.** To identify beads behaving differently than the general strain field of the substrate, the displacements of beads belonging to the inside of the mesh (a.) were interpolated based on the displacements of neighboring beads enclosing it (b.) and the error in interpolation was calculated. The displacements for most of the beads was calculated with an interpolation accuracy of around 2% with some outliers behaving differently (c.) Once the source of error of the beads was identified (d.) and the key beads were removed, the mean error was reduced significantly (e.). The interpolation error had a negative correlation to the beads density in the substrate, pointing to substrate homogeneities that require a high spatial sampling (f.) but not to the mean substrate strain (g.).



**Figure 3.12: Example of heterogeneity in local strains.** Two examples of substrate deformation within the image fields of around  $100 \times 100 \times 30 \mu\text{m}^3$  show how although there is indeed a difference in strain magnitude between the two data sets **a.** vs. **b.**, there are significant variations within different regions.

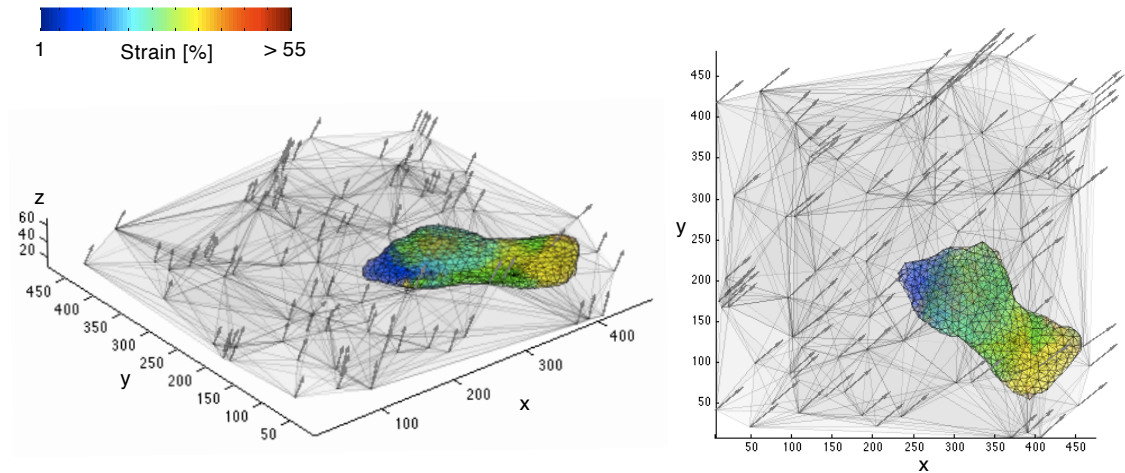
there lies an importance on characterizing the local strains. With the meshing of the beads in tetrahedra, we can calculate the individual tetrahedra strain as described in 2.6.2. This gives a local description of the deformation in the substrate at a relevant scale for the cells embedded in it. Examples in **Fig. 3.12** show that although a magnitude range of the strains is observed in the different stretching examples (**a.** vs. **b.**), the local variation is indeed very high (e.g. ).

The ability to measure the magnitude of substrate strain and the accuracy of interpolation for each stretching series enabled the selection of suitable experimental data sets for the analysis with: high bead density, low interpolation error and high substrate strain (**Fig. 3.11 g.**).

### 3.2.5 Mapping substrate strain on cellular structures

With the calculation of local substrate strain for the substrate meshes we could then map these strains on the cells surfaces as described in section 2.6.2. As it can be seen on **Fig. 3.13**, strains are not uniformly distributed on the cell surface. The actual strain the cell *feels* depends on the local substrate strain. Being able

to capture these heterogeneities in 3D is not only essential for the calculation of mechanical properties, it is also an important feature for the investigation of the effects of stress and strains on cells.

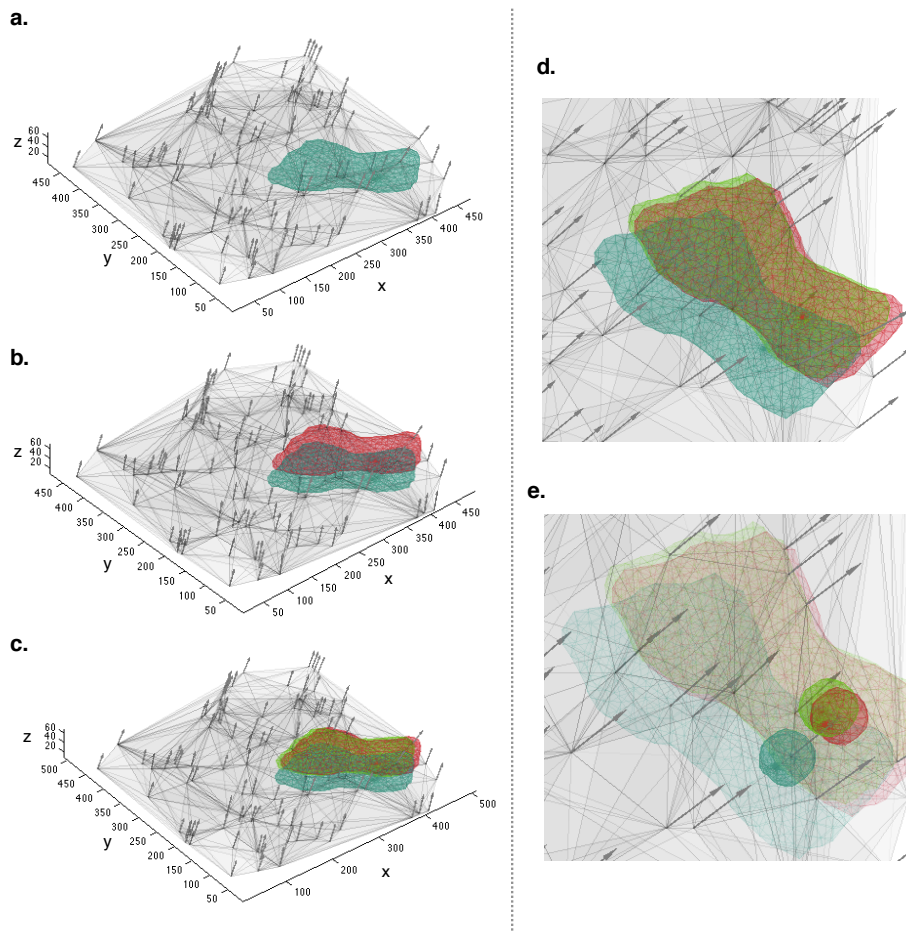


**Figure 3.13: Mapping substrate strain on cell surface.** Having calculated the strain for the substrate elements. The strain 'felt' by the cell depending on its localization within the matrix could be calculated.

### 3.2.6 Geometrical interpolation of cell and nucleus

The same point interpolation tools used for sec. 3.2.4, were implemented to interpolate the position of the cell and nucleus after stretching. Most studies with substrate stretchers so far have been working under the assumption that cells adhere strongly on the substrate and behave as the substrate itself, a behavior that was first observed in [Caille et al., 1998] and then confirmed [Gilchrist et al., 2007] and cited by others [Lombardi et al., 2011a]. Yet, other studies with similar stretching devices have reported that cells deform significantly less than the substrate applied to the substrate (e.g. 30-60% of applied strain in [Wall et al., 2007]). However, all of these studies have described the substrate- to cell - strain relationship for 2D substrates.

With our developed tool for geometrical interpolation it is possible to interpolate the displacements of the individual points forming the cellular mesh at  $t_1$  (Fig. 3.14 a.) to calculate their predicted position at  $t_2$  i.e. after stretch (Fig. 3.14 b.). Comparison to the actual position of the cell (Fig. 3.14 c. and d.) gives a



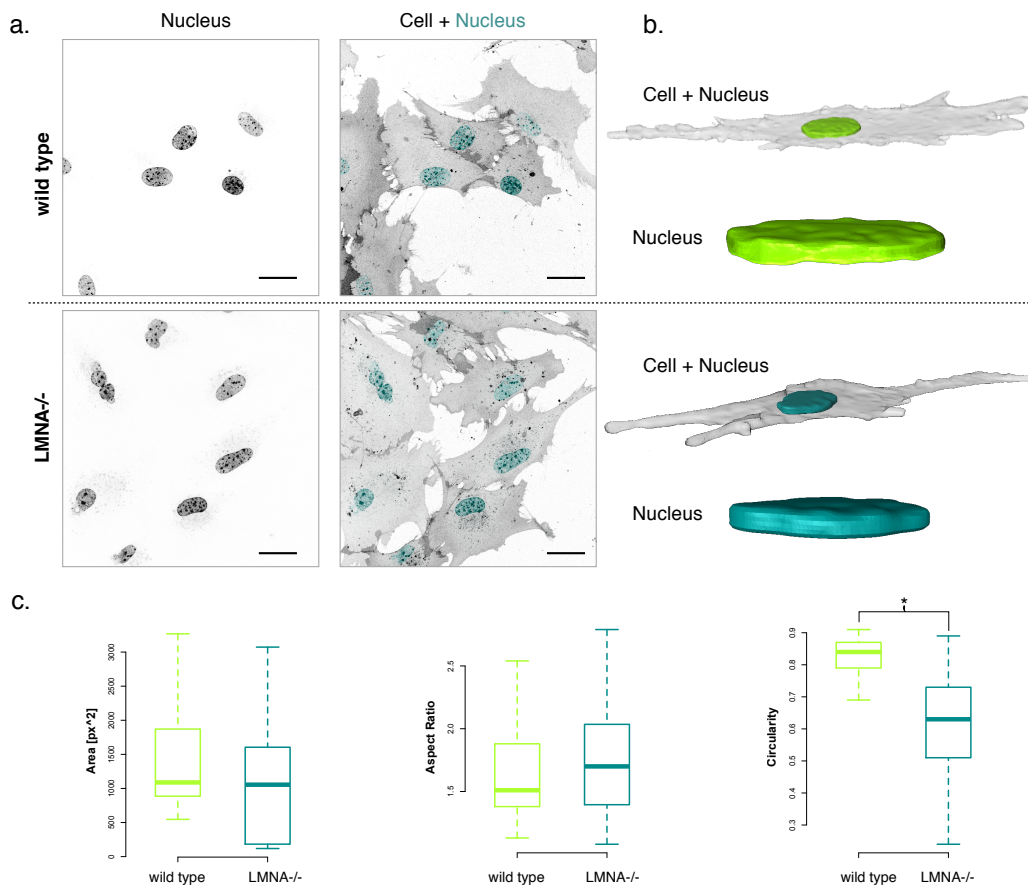
**Figure 3.14: Interpolation of cell and nucleus with substrate displacement.** By using the substrate displacements to interpolate the surface mesh model of the cell before stretching (**a. blue cell**), the position and shape of the cell at after stretching could be estimated (**b. red cell**). Comparison to the actual position of the cell after stretching was possible with the mesh model with the cell at t2 (**c,d. green cell**). The same can be done for the nuclei (**e.**)

qualitative measure of the degree of attachment of the cell to the substrate. Or with the assumption that cells in collagen matrix are completely embedded into the substrate it gives a qualitative measure of the relative stiffness of the cell to the substrate. The same principle can be applied to the cell nuclei (**Fig. 3.14 e.**), to learn the way in which strains are transduced into the cell interior.

Finally, the interpolated displacements acting on the cell surface can serve as boundary conditions to make a more formal calculation of the intracellular deformation and calculate a quantitative measure of relative stiffness, taking into consideration mechanical constants.

### 3.3 Mechanical phenotyping of wt vs. LMNA<sup>-/-</sup> MEFs

The system of wild type and LMNA<sup>-/-</sup> MEFs was initially established in [Sullivan et al., 1999] and has been extensively used since then by several groups to characterize the importance of the lamin A/C proteins in cell mechanics [Lammerding, 2004, Broers, 2004, Lee et al., 2007]. Therefore, they serve as a model system for nuclear structural fragility.



**Figure 3.15: Cellular and nuclear geometry of wild type and LMNA<sup>-/-</sup> cells and nuclei.**  
**a.** Cells and nuclei of wild type and LMNA<sup>-/-</sup> cells exhibit a very similar morphology when observed under the microscope, except for the LMNA<sup>-/-</sup> nuclei with clear structural damage (red circles) **b.** Example 3D volumetric reconstructions of cells and nuclei of both phenotypes also show very similar shaped. **c.** Even quantitatively, no morphological differences are observed in the total area or aspect ratio of the nuclei. Only by taking into account the damaged nuclei in the LMNA<sup>-/-</sup> cells, significant changes in circularity between the nuclei can be observed.

When looking at the cells and nuclei of wild type vs. LMNA<sup>-/-</sup> MEFs no ob-

vious qualitative morphological differences are observed. Except for nuclei with clear structural damage (red circles), both phenotypes have a very similar appearance when observed under the microscope (**Fig. 3.15 a.**). The similar appearance of the very flat cells and nuclei, characteristic of fibroblasts, can also be appreciated in the 3D reconstruction (**Fig. 3.15 b.**).

### 3.3.1 No nuclear morphological differences

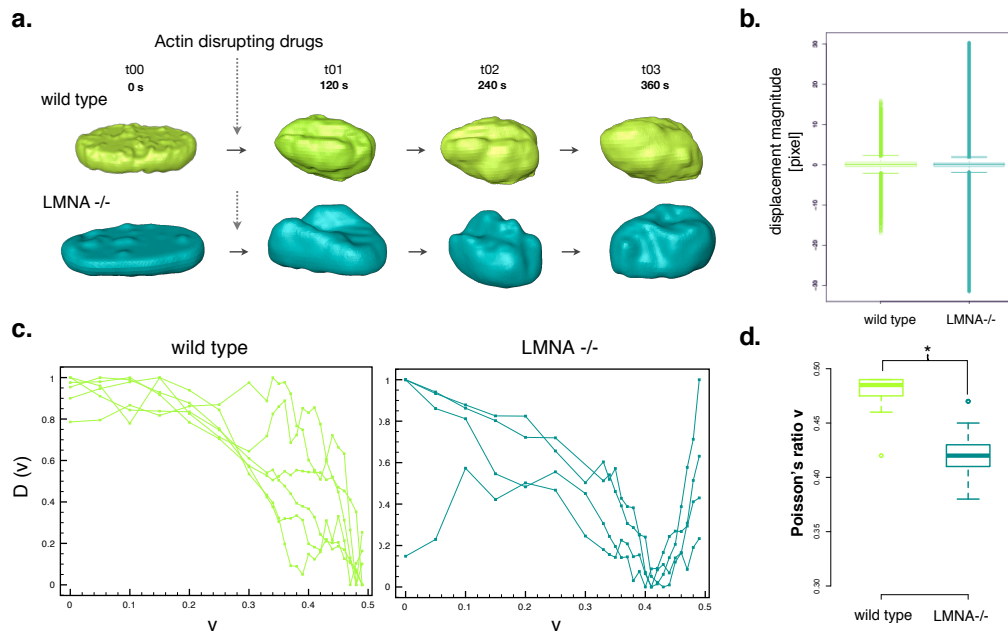
To test if quantitative measures could capture a difference in morphology between the phenotypes, the shapes of the nuclei of wild type and LMNA<sup>-/-</sup> MEFs were quantified by segmenting the image stacks and measuring the geometrical properties of the found structures. Because these cells and their nuclei are extremely flat (3D aspect ratio:  $\approx 0.2 \pm 0.1$ ) (**Fig. 3.15 b.**), the properties were calculated in 2D with the help of z-projections. No significant differences in area or aspect ratio are observed between the wild type and LMNA<sup>-/-</sup> cells. The significant difference in circularity (**Fig. 3.15 c.**) arises from nuclei which show some degree of structural damage.

### 3.3.2 Increase of nuclear compressibility in LMNA<sup>-/-</sup> MEFs<sup>2</sup>

Examples of the surfaces depicting nuclear deformation for wt and LMNA<sup>-/-</sup> cells are shown in **Fig. 3.16 a.** In both cases, nuclei round up shortly after drug exposure. However, the LMNA<sup>-/-</sup> cell nuclei undergo stronger deformations, as seen when comparing the displacement magnitudes of these two cell types (**Fig. 3.16 b.**). The larger local deformations of the LMNA<sup>-/-</sup> nuclei are also reflected in a more wrinkled boundary of the LMNA<sup>-/-</sup> cell nuclei compared to the wild type cells. Examples of the dissimilarity curves  $D(v \in [0, 0.5])$  for the wild type and mutant cells are shown in **Fig. 3.16 c.** Comparing the minima of the dissimilarity curves one can see significant differences in the obtained  $v$  values. The distribution of the resulting  $v$  values for all measurements is shown in **Fig. 3.16 d.** Mean values of  $0.48 \pm 0.02$  ( $n = 27$ ) and  $0.43 \pm 0.02$  ( $n = 40$ ) were determined for the wt and the LMNA<sup>-/-</sup> cells, respectively. This points to a significant increase in nuclear compressibility for the LMNA<sup>-/-</sup> cells.

<sup>2</sup>Section adapted from [González Avalos et al., 2011]





**Figure 3.16: Nuclear compressibility of wild type and LMNA<sup>-/-</sup> nuclei.** **a.** Comparison of nuclear deformations over four time steps for the wild type and LMNA<sup>-/-</sup> cells, respectively. The LMNA<sup>-/-</sup> nuclei exhibit stronger deformations that are characterized by large furrows on the upper side of the nucleus. **b.** Comparison of the distributions of displacement magnitudes [in pixel units] shows stronger deformations LMNA<sup>-/-</sup> MEF cell vs wild type MEF. **c.** Dissimilarity curves  $D(v)$  for determination of the Poisson's ratio of the nuclear interior of wild type and LMNA<sup>-/-</sup> cells, respectively. **d)** Summary of measurements of  $v$  values for wild type and LMNA<sup>-/-</sup> MEF cells. Mean values of  $0.48 \pm 0.02$  ( $n = 27$ ) and  $0.43 \pm 0.02$  ( $n = 40$ ) were measured for the wild type and the mutant cells, respectively. **e)** Comparison of  $v$  values determined for series of wild type nuclei with the bleaching patterns method ( $0.48 \pm 0.02$  ( $n = 27$ )) and for series in which only the deformation of naturally occurring gradients was monitored ( $0.44 \pm 0.1$  ( $n = 15$ )). [Figure and legend from [González Avalos et al., 2011]]

### 3.3.3 No nuclear viscosity differences

FRAP measurements were performed in an attempt to correlate the observed changes in nuclear compressibility to changes in the viscosity of the nuclear interior. However, no differences in the diffusion coefficient of paGFP were measured in the nuclei of wild type ( $\mu = 23.7 \pm 3.3 \frac{\mu\text{m}^2}{\text{s}}$  |  $n = 15$ ) vs. LMNA<sup>-/-</sup> cells ( $\mu = 23.7 \pm 5.3 \frac{\mu\text{m}^2}{\text{s}}$  |  $n = 16$ ). A comparison to 3T3 Fibroblast also did not show any differences ( $\mu = 22.3 \pm 5.1 \frac{\mu\text{m}^2}{\text{s}}$  |  $n = 35$ ).

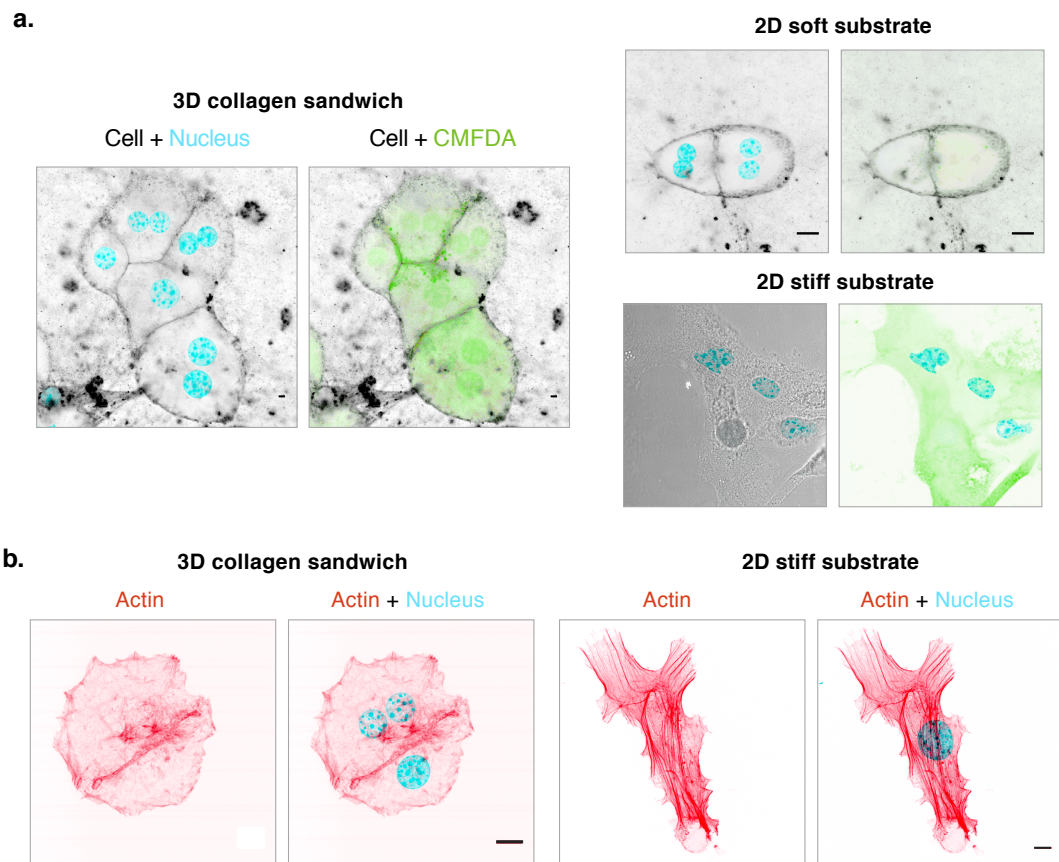


### 3.4 Mechanical phenotyping of hepatocyte EMT

Hepatocytes are an interesting research target. They contribute to 80-90% of the liver mass and their ability to metabolize foreign compounds is what renders the liver the main organ involved in detoxification of xenobiotics [Eckl and Bresgen, 2003]. This makes them an attractive cell system for toxicological studies. They are also a model system for epithelial cell polarity and how loss of the polarized phenotype relates to fibrosis, cirrhosis and finally to carcinomas.

#### 3.4.1 pmHCs need a 3D substrate to preserve epithelial polarity

Differentiated and functional hepatocytes show a particular kind of epithelial polarity. Simple polarized cells have an apical and one basolateral side. Hepatocytes, on the other hand, have several apical and vasolateral poles and the apical sides form a continuous network of so called 'bile canaliculi' [Decaens et al., 2008], which are specialized structures responsible for secreting bile extract and for the uptake of recycled biliary salts, hence their name. The formation of these organotypic structures is one important marker for differentiation in hepatocytes. When plated in 3D collagen sandwich (3D cs), primary mouse hepatocytes (pmHC) form functional bile canaliculi as tested by adding cell tracer CMFDA. CMFDA molecules freely pass through the cell membrane and their impermeable metabolites stains the cell interior green. Polarized hepatocytes secrete CMFDA through these channels, where aggregation of the fluorescent tag can be observed (**Fig. 3.17 a. 3D collagen sandwich**). The formation of bile canaliculi is lost when the cells are plated in just one layer of soft collagen (**Fig. 3.17 a. 2D soft substrate**). Total functionality loss and loss of the phenotype is observed when cells are plated in stiffer substrates like cell culture plastic or even in silicone membrane (**Fig. 3.17 a. 2D stiff substrate**). The extent of the change in shape and structure of the cells when plated in 2D vs. 3D substrates can be more strikingly observed when fixing the cells and looking at the structure of their actin filaments (**Fig. 3.17 b. 3D collagen sandwich**). Differentiated hepatocyte cells in the 3D substrate have a mostly round shape and an actin cytoskeleton arranged to enforce cell-to-cell contacts. On the 2D substrate the round shape is lost and a prominent network of actin stress fibers can be observed (**Fig. 3.17 b. 2D glass**).



**Figure 3.17: Primary mouse hepatocytes (pmHCs) in 2D and 3D substrates.** **a.** pmHCs only conserve their fully epithelial phenotype when plated in 3D substrates. The formation of functional bile canaliculi was examined by incubating the cells with the green fluorescent tracer CMFDA, which freely passes through cell membranes. Functional and polarized hepatocytes continuously secrete the fluorescent metabolite of the cell marker into their bile canaliculi, where an accumulation of the green staining can be observed (**3D collagen sandwich**). This accumulation is not observed when cells are plated on layer of soft collagen, although some cells still retain their shape and form cell-to-cell contacts (**2D soft substrate**). Complete loss of epithelial morphology is observed when cells are plated in stiffer substrates (**2D stiff substrate**). **b.** The structural changes dependent on the substrate dimensionality can be further appreciated when looking at fixed cells and staining their actin filaments. Polar epithelial cells are characterized by the absence of actin stress fibers and actin staining is only observed at cell-to-cell contacts (**3D collagen sandwich**). When plated in stiff substrates (here, cell culture glass), the shape of the epithelia cell is completely different and major formation of stress fibers is seen (**2D stiff substrate**). Scale bars = 10  $\mu\text{m}$ .

Experiments aiming at investigating hepatocyte function or polarity should therefore be performed solely in 3D substrates. For all following experiments to study hepatocyte EMT<sup>3</sup>, pmHCs were plated in the collagen sandwiches as described in Section 2.1. To characterize morphological, structural and mechanical changes during hepatocyte dedifferentiation pmHCs were treated for 48h with TGF- $\beta$  and the features described in the following sections were analyzed.

### 3.4.2 Changes in cellular and nuclear morphology in EMT

Example images of cell membrane and nucleus of untreated and TGF- $\beta$  pmHCs show the change in cellular and nuclear morphology observed after TGF- $\beta$  treatment (**Fig. 3.18 a.**). In cell bundles or as individual cells, polar and untreated pmHCs exhibit the mostly roundish cellular shape characteristic for epithelial cells. Upon treatment with TGF- $\beta$  their cellular shape changes dramatically into a variety of spindle- and star- like shapes observed in mesenchymal cells (**Fig. 3.18 c.**). When reconstructing the cellular surfaces in 3D one can see that apart from elongating, TGF- $\beta$  treated cells become much flatter (**Fig. 3.18 b.**).

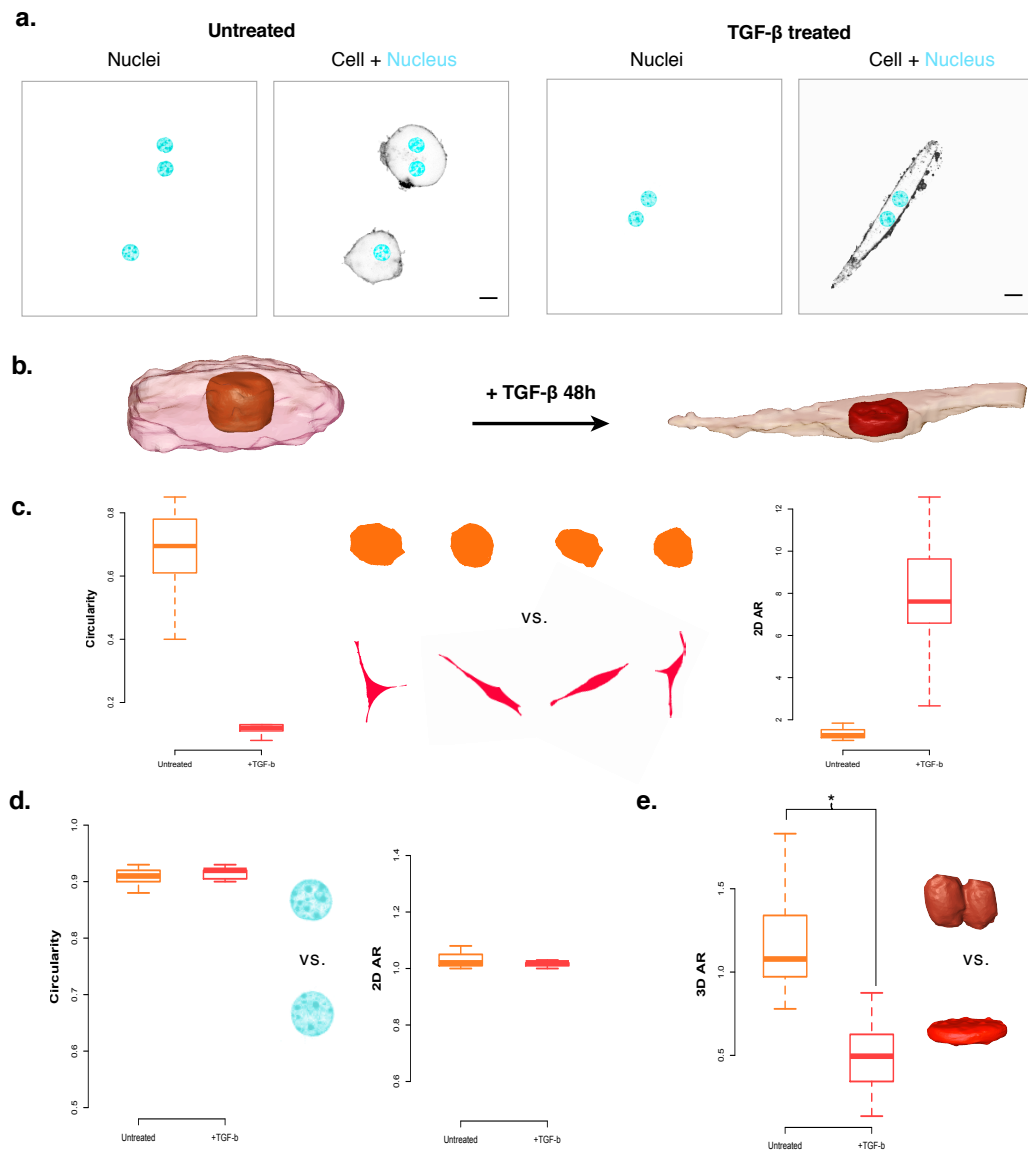
The change in nuclear morphology is not that obvious. When observed in just one plane, nuclei from untreated and treated cells are undistinguishable (**Fig. 3.18 d.**). Upon quantification of morphological properties, projections of pmHC nuclei show an almost perfect circularity between 0.9-1 and an aspect ratio around a value of 1. These features remain unchanged after treatment (**Fig. 3.18 d.**). It is only after reconstruction of their 3D geometry that the striking change in shape is visible. While nuclei of untreated cells are elongated cylinders, their treated counterparts become extremely flat (**Fig. 3.18 e.**). This change is captured by measuring the 3D aspect ratio of the nuclear surfaces, a measure which significantly differs between treated and untreated cells (**Fig. 3.18 e.**).

### 3.4.3 Changes in cytoskeleton organization in EMT

The structural organization of hepatocyte cytoskeleton filaments was analyzed by immunofluorescent staining. **Fig. 3.19** shows the distribution of the different cytoskeleton components (actin, vimentin and microtubule) in untreated and

---

<sup>3</sup>As described in the introductory section, EMT is a process of dedifferentiation. A transition of one type of differentiated cell (here epithelial) to another type of differentiated cell (here mesenchymal)



**Figure 3.18: Morphology changes after TGF- $\beta$  treatment.** Example images **a.** and 3D surface reconstructions **b.** of nuclei and cells of pmHCs untreated and after 48h TGF- $\beta$  incubation. **c.** After treatment a drastic change in shape can be observed. **c.** The circular epithelial cells transform into a variety of spindle and star shaped mesenchymal-like cells. **d.** Changes in nuclear morphology pass undetected when looking at 2D images, where the nuclei maintain its marked circularity after treatment **e.** However, a significant change can be observed when looking at their shapes in 3D dimensions. The elongated nuclei in z-direction get significantly flatter as can be measured by their 3D aspect ratios. Scale bars = 10  $\mu\text{m}$ .

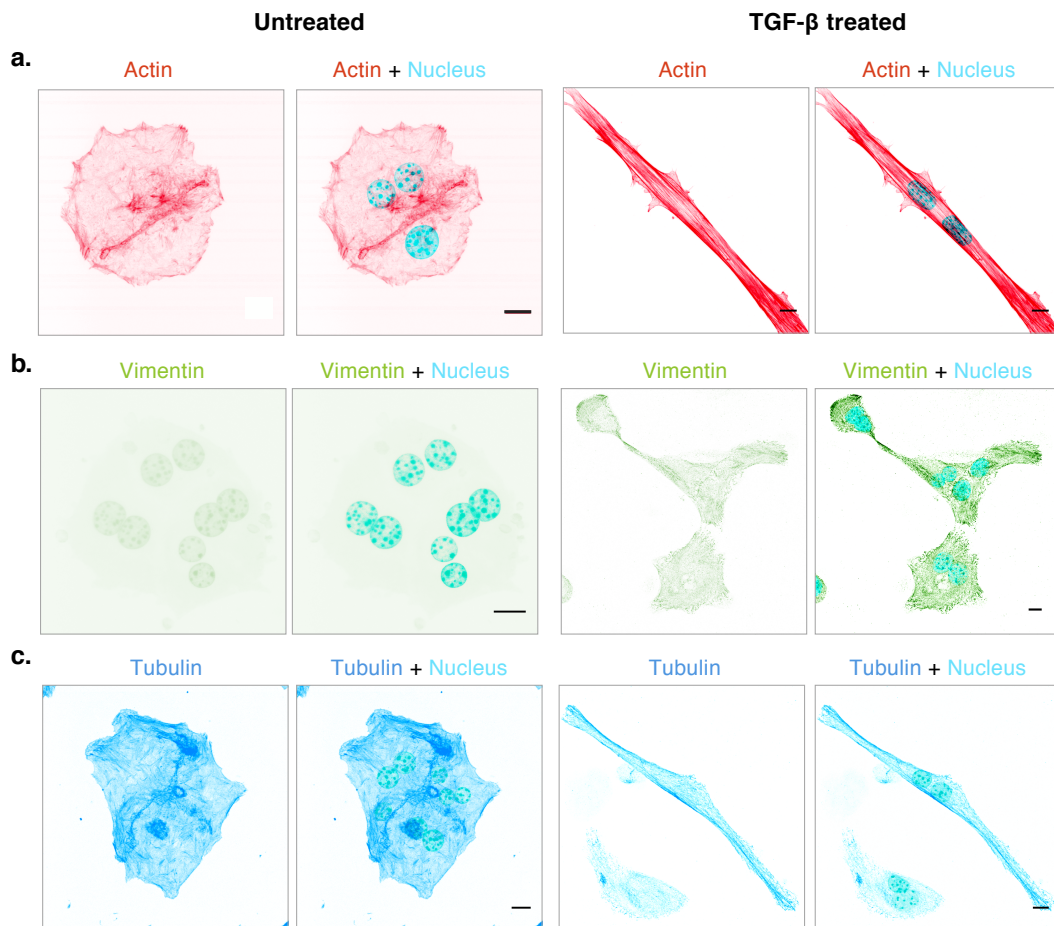
TGF- $\beta$  treated cells. In untreated cells, actin filaments are ordered primarily at the cell to cell contacts, supporting the bile canaliculi (**Fig. 3.19 a.**). This specific type of actin organization is explained by the formation of actin belts around the channels, which by association with myosin proteins are responsible for bile canaliculi contractility [Tsukada and Phillips, 1993]. After TGF- $\beta$  treatment, actin stress fiber formation can be observed along the whole cell. Vimentin is not expressed in differentiated hepatocytes. Cytoplasmic intermediate filaments are differentially expressed and epithelial cells are known to express keratins. Loss of keratin expression and gain of vimentin expression is actually one of the markers for EMT. In dedifferentiated pmHCs vimentin is expressed as a network around the nucleus and across the whole cell (**Fig. 3.19 b.**). Keratin immunostaining was performed to visualize the intermediate filament structure in untreated hepatocytes. Unfortunately, none of the two different antibodies utilized worked with the immunostaining protocol.

Microtubules form a network of filaments visible inside the whole cell, radiating from the nucleus and visible inside the whole cell. This network can be seen in differentiated pmHCs as well as in cells after treatment (**Fig. 3.19 b.**). In cell bundles of differentiated pmHCs there is also an enhanced expression at the bile canaliculi. Microtubules are important players in the formation and maintenance of these structures, as they provide the tracks for transport of proteins [Cohen et al., 2004].

#### 3.4.4 Decrease of nuclear compressibility after EMT

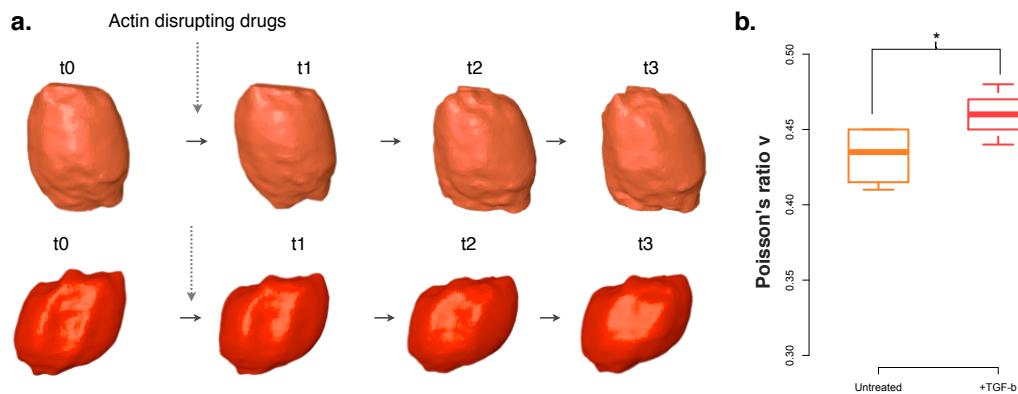
After observing the dramatic change of shape in the nuclei of TGF- $\beta$  treated vs. untreated hepatocytes, we proceeded to measure the compressibility of the nuclear interior with the established *Nuclear compressibility* framework. This was carried out in the context of a master student internship and experiments were performed by Lisa Kaschel under my supervision. As described in sec. 3.1.6, the experimental setup to follow nuclear deformations after cytoskeleton disruption was easily adapted to work with the cells embedded in the 3D substrate.

Examples of surface reconstruction of time series of deforming nuclei of treated and untreated pmHCs is shown in **Fig. 3.20 a.** Although in general, smaller deformations were observed in the hepatocytes in comparison to the MEFs, the deformations were large enough to calculate a Poisson's ratio for both cell states.



**Figure 3.19: Changes in the pmHCs cytoskeleton organization after TGF- $\beta$  treatment. a.** In differentiated hepatocytes, actin structures can be observed around the bile canaliculi. Upon treatment, stress actin fibers are observed to span the whole cell. **b.** As expected for epithelial cells, no vimentin expression is observed in untreated hepatocytes. The vimentin network can be observed after treatment with TGF- $\beta$ . **c.** The network of microtubules can be observed in untreated as well as in treated cells. In untreated cells however, enhanced microtubule accumulation can be seen along the bile canaliculi. Scale bars = 10  $\mu\text{m}$ .

An increase in the Poisson's ratio from a value of  $0.44 \pm 0.02$  ( $n = 8$ ) to a value of  $0.46 \pm 0.02$  ( $n = 10$ ) was measured, meaning a significant decrease in nuclear compressibility after treatment.

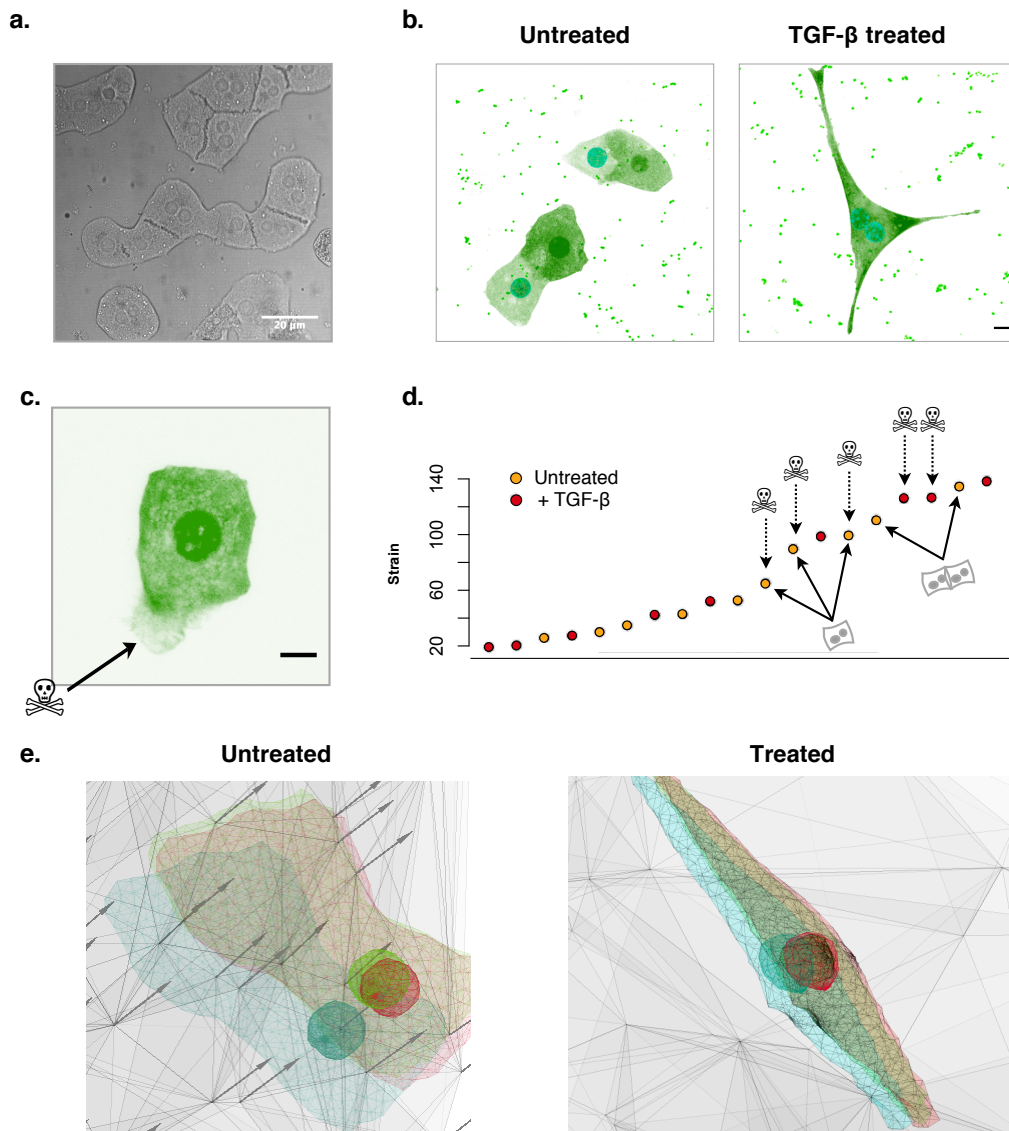


**Figure 3.20: Decrease of the compressibility of the nuclear interior after TGF- $\beta$ .** a. Example time series of deforming nuclei of treated and untreated pmHCs with the experimental pipeline to study nuclear compressibility. b. An increase in the Poisson's ratio after TGF- $\beta$  treatment from a value of  $0.44 \pm 0.02$  ( $n = 8$ ) to a value of  $0.46 \pm 0.02$  ( $n = 10$ ) was measured/

### 3.4.5 pmHC EMT on the 3D stretcher

When plated on the stretcher membranes within the 3D collagen matrix, treated and untreated pmHCs were viable in the 3D stretcher chamber. Untreated hepatocytes also stayed in their undifferentiated form, exhibiting their characteristic organotypic structures (Fig. 3.21 a.). Over the course of several months, experiments with these cells were optimized leading to several stretching series for untreated and untreated cells (examples in Fig. 3.21 b.).

While performing the experiments, some cells (treated as well as untreated) would undergo sudden cell death as a consequence of the stretching procedure, showing membrane bubbles and damage in the cell nucleus (Fig. 3.21 c.). We took advantage of the possibility of quantifying the magnitude of substrate deformation and mapping it into the cells, to check if this sudden cell rupture was correlated with the magnitude of deformation that the cells experienced. Indeed, this kind of cell death was observed to happen at high deformation of the substrate. The degree of deformation at which this effect was observed also varied with EMT.



**Figure 3.21: pmHCs on the 3D stretcher.** **a.** pmHCs are viable and form organotypic structures inside the 3D stretcher chamber. This enabled the acquisition of stretching series for both treated and untreated cells as exemplified in **b.** **c.** Sometimes the cells would die as a result of the stress imposed on them. Cell damage was visible in the form of ruptures in the membrane (s. arrow) and altered cell nuclei. **d.** This death event correlated with high strain magnitude of the substrate for both treated (red points) and untreated (orange) cells. Treated cells seem to be more resistant than untreated cells. However, untreated cells in cell bundles are also able to resist higher amount of strain. **e.** Examples of stretching series analysed with the geometrical interpolation of cell and nucleus show qualitative differences between untreated and treated cells. Although in both cases the interpolated cell surface (red) matches the cell position after stretching (green), the position of the nucleus of the untreated cell after stretching (green nucleus) is not accurately predicted by interpolation (see different positions of the red and the green nuclear surfaces). In contrast, in the treated example the positions of both the cell and the nucleus are well matched by the pure geometrical interpolation (as can be appreciated by the green and red surfaces lying over each other).



It can be observed that untreated cells start dying at a lower magnitude substrate deformation than treated cells. Interestingly, this is the case for single untreated cells. Untreated cells in cell bundles showed a higher resistance to deformation (**Fig. 3.21 d.**).

In the examples where cell and nuclear deformation was estimated by interpolation, qualitative differences were observed between treated and untreated examples. While both cells of untreated and treated cells were accurately interpolated by the substrate displacements, the nuclei inside untreated cells showed a large interpolation error. On the other hand, nuclei in treated cell moved more homogeneously with the cell body and showed a lower interpolation error (**Fig. 3.21 e.**).



# 4

## Discussion

### 4.1 On the methods developed & the cell mechanics field

#### 4.1.1 The Nuclear compressibility framework in context

The experimental and computational framework to measure the compressibility of the nuclear interior had been developed before and was first published to be capable to measure the compressibility of one deforming nucleus in [Gladilin et al., 2010], where the general experimental idea and numerical framework are presented in detail. However, upon the first attempt to use this framework for comparative measures of different phenotypes (i.e. actual phenotyping) in [Gonzalez, 2008, Gonzalez et al., 2009], several difficulties on both the experimental and computational sides were identified that did not allow measurements of enough cells to achieve statistical significant results. By optimizing the key identified aspects of both experimental and image analysis sides, a reliable and stable overall framework to perform comparative studies between cell phenotypes was established. This led to the publication of the comparative study of the wild type vs. LMNA<sup>-/-</sup> MEFs [González Avalos et al., 2011] and enabled the characterization of the nuclear compressibility changes in the TGF- $\beta$  treated and untreated pmHCs.

The bleaching of patterns of the fluorescent proteins to better follow deformations enabled us to enhance the signal to noise ratio and overcome the constraints imposed by the natural occurring patterns. By itself, this implementation can be combined with any other LSCM-compatible method to study nuclear and cellular mechanics that is based in detecting deformations by microscopy (s. **Table 1.1**).

The framework presented to measure the compressibility of the nuclear interior has several advantages over other established method to measure nuclear mechanical properties: in contrast to AFM or micropipette aspiration techniques, no isolation of the nuclei is required and the nuclei can be measured in their physiological environment inside the cell; the contact-free mode of action also enables the easy implementation for cells in 3D substrates, this is not possible with all methods that require direct contact to the structures to be studied like the compression based methods; finally, coupling the relative simple experimental setup with the automatic computational analysis, measurement of a substantially higher amount of nuclei is enabled to permit studies with statistical significant results - something that in the field of nuclear and cellular mechanics is not yet to be taken for granted.

On the other side, a disadvantage of the method is that the magnitude of forces acting on the nuclei to induce deformation upon cytoskeleton disruption remains unknown. Thus, we are restricted to the calculation of the compressibility. The calculation of further parameters, like the stiffness, requires a precise description of the internal forces acting on the nuclei upon actin filament disruption. These forces can be estimated as attempted in [Jean et al., 2004] by integrating information about adhesion sites and actin filament structure. Their approach is based on 2D image outlines and the description of forces and deformation remains very descriptive. However, by expanding this approach with 3D images and calculating the forces for the whole nuclear surfaces - the methods could be combined to gain several mechanical parameters from the description of deforming nuclei.

As the significance of changes in nuclear compressibility are difficult to interpret (s. also sec. 4.2.1), the results of these method should be taken with care and put in context with other measured features if the goal is to gain biological understanding.

#### **4.1.2 The 3D substrate stretcher framework in context**

Planar substrate stretchers are mostly used in the field of cell mechanics to apply continuous strain on cells and measure their effect on a genetic or biochemical level afterwards [Richard et al., 2007, Le Bellego et al., 2006, Hornberger et al., 2005, Boerma et al., 2005]. They have also been adapted by several groups for the use together with microscopy techniques to characterize cellular and intracellular deformations [Tan et al., 2008, Gavara et al., 2008] and reviewed for the nucleus

in [Lammerding et al., 2007]. The problem relying the compatibility with high-resolution live-cell imaging was recently addressed by [Huang et al., 2010] with a similar in-house developed chamber, however most of these methods are still restricted for the use in epi-fluorescent microscopes, with which characterization of 3D deformations is not possible.

This first problem was addressed with the modifications of the chamber and the optimization of the microscopy set-up. The ability to keep cells in viable conditions in the imaging chamber to perform high-resolution 3D live-cell imaging while stretching, open the door to studies in mechanotransduction. By optimizing different fluorescent stainings to mark the diverse structures involved - e.g adhesion sites, cytoskeleton filaments, members of the LINC complex - and implementing less aggressive forms of 3D microscopy, this stretching chamber can be used to study the structures interplay during force application.

Furthermore, the experiment was also enhanced for performing experiments with cells fully embedded in 3D substrates. This represents the most important asset of this framework, because so far only particle rheology techniques had succeeded in analyzing the mechanical behavior of cells in 3D substrates [Panorchan et al., 2006].

The possibility to characterize local substrate strains and mapping them on the cells enables a whole range of further experiments to relate strain to its effects on cellular function. The importance to characterize 3D substrates will be growing in the next years with the cell biology field moving towards the use of 3D cell cultures (s. also sec. 4.1.5). The measurement of quantitative mechanical properties like the relative stiffness is also enabled and will be implemented in the future, combined with 3D mechanical and numerical modeling.

#### **4.1.3 Mechanical properties should be analyzed in 3D**

This might be a strong declaration and surely not applicable to every cell type. But for cells that in physiological conditions grow in a 3D environment, the massive differences resulting in plating cells in 2D vs. 3D substrates in terms of morphology [Grabowska et al., 2011], adhesion properties [Cukierman et al., 2001], viability [Peretz et al., 2007] and gene expression [Li et al., 2007] speak for themselves regarding the importance of the right environment for the cells. This is particular relevant for the area of cell mechanics: if all the structures involved in mechanics

and mechanotransduction are differently arranged in 2D vs.3D substrates, what significance does it have to measure the cells outside its environment? The importance of analyzing cancer progression and malignant transformation in 3D environments has been focus of recent reviews encouraging cell culture research to move in this direction [Yamada and Cukierman, 2007] [Albini and Sporn, 2007].

Despite its observed importance, implementation of 3D substrate measurements to cell mechanics approaches has been hampered by the general working mode of the field. In a field where implementation of biophysical methods to measure certain parameters is still very challenging and often seen as the final goal, it is easy to neglect the biological context. But being able to just calculate something should not stay as the final goal. As presented in the introduction, many parameters have been measured so far. But with the wide palette of techniques and models used, the results are neither comparable to each other nor provide biological insight because the biological context of the cells is often ignored.

In a way, this work started with the similar aim of establishing measurement methods, but it is part of the development of interdisciplinary work, specially in the field of systems biology, to evolve together with the methods being developed and identifying the necessities that the biological system need. Not only modifying the biological samples to fit the methods, but adapting the methods to meet the requirements of the biology that is being studied. In order to change the way research is being performed in this field and to enable more hypothesis driven research questions, the first step is to provide tools to analyze the cells in a physiological environment, as well as tools that open the possibilities of relating the observed mechanical behavior to specific functional measurements. I hope the tools developed within this project can contribute to the field in this respect.

The results of the structural and morphological differences observed in pmHCs when plated in 2D vs 3D support these claims, making the point very clear on how important it is to maintain the cells in the 3D environment where they can develop physiological structures. If the whole cytoskeleton is changed and the polarity of the cells is lost in 2D, how are the changes arising from treatment supposed to be observed? As shown in this work, the relevant morphological, structural and mechanical changes featured in EMT are only apparent once cells exhibit a fully differentiated epithelial phenotype before the onset of dedifferentiation.

#### 4.1.4 Image & model based methods enable measurements in 3D

Methods that measure the influence of forces in cells that can be adapted for working in 3D cultures are now being enabled by advances of microscopy, image analysis and their integration to mechanical modeling. To be able to work with cells embedded within the substrates, enabling deformations and measuring the effect of cells without directly 'touching' the cells is a key aspect.

The framework to study the compressibility of the nuclear interior provides a good example on how a relative simple experimental idea i.e. to disrupt cytoskeletal filaments with drugs to let nuclei round up, can be further developed into a working framework to study mechanical properties. In fact we are not doing more than adapting microscopic acquisition and image processing to look at the trypsination process that cell biologists use to split cells everyday. By identifying the requirements of the analysis tools by understanding and implementing the theory (e.g. realizing how the optimal patterns should look like for the calculation) and then implementing them into the biological system (e.g. bleaching these patterns onto the nuclei), the common problems in biology like the fluctuations in the measurement due to noise could were addresses and corrected. The step for performing experiments in 3D was so easy because the experiment was already based in being able to acquire a process by microscopy and the knowledge existed in order to i. adapt the conditions of the biological sample in order to keep providing cells with the proper environment (e.g. have the cells embedded in enough collagen) and ii. fulfill the requirements of the experimental setup (respecting the objectives working distance).

The development of the 3D substrate stretcher provides another example of how this can be achieved. The whole development pipeline, from the chamber construction to the determination of bead concentration or cells staining was a loop of adapting the requirements of the biological side (e.g. cells need space, cells need medium, cells need the 3D matrix) to the capacities of the machines (the objectives are limited by their working distance, the microscope stages can't hold heavy weight) to the necessities for the analysis (generation of surfaces for cells and nuclei was only possible by adapting the stains on cells, strain can only be calculated with enough accuracy if a certain bead density is present).

Another advantage of these methods is that they can be upscaled to measure a higher amount of cells. Image processing pipelines and the mechanical analysis can

all be integrated in automated scripts. Once the acquisition at the microscope is automated as well, measurement of many cells together with their analysis can be very quickly. Similar substrate stretching devices have been adapted to work in an automated way [Huang et al., 2010, Lombardi et al., 2011b]. This is not yet completely solved for our approaches, as the microscopy acquisition is still very tricky, but the potential is there. The tasks being performed like finding the previous image field and adjusting the volume to the beads densities are processes that, in theory, can be now easily implemented with *intelligent imaging* approaches [Conrad et al., 2011]. Coupling analysis scripts to the microscopy acquisition softwares and training them to perform tasks automatically that so far are being performed manually by the user(s), will open the doors to enhancing the measured throughput and making the methods available and usable for more people.

The final advantage of these methods is that the cells measured are treated in the same mechanical conditions. Cells measured are embedded in the same substrate and exposed to the same conditions. This is important to reduce the effects of variability in the measurement i.e. the probability for having systemic effects of probe treatment is higher when isolating 10 nuclei, grab them and mount them under the AFM machine one by one than with measuring the rounding up of 10 nuclei of cells embedded in the same matrix, in the same chamber, with the same temperature.

#### **4.1.5 Importance of the local characterization of substrate strain**

As outlined in the introduction, many substrates exist and are currently under development to use as substrates for 3D cultures [Yamada and Cukierman, 2007]. Also in this respect, it is important to find appropriate substrates that provide the biological functionality for the cells that need to be studied and at the same time are well characterized to understand what is the effect that these substrates have on the cells. As the field of 3D cell cultures grows, so is the necessity of understanding the effects that the substrates have on the cells. Collagen matrices, like the ones used in this study had been shown to have a non affine behavior. This means that deformation at small scales is not affine to the bulk deformation observed at the macroscopic level. To understand what the cells are actually feeling we need to be able to describe the deformations at that local scale. Indeed, as claimed by [Pedersen and Swartz, 2005] "one of the major challenges in mechanobiology is to better



characterize cell strain vs. bulk strain in various 3D systems undergoing mechanical perturbations so that mechanisms of cell response can be better investigated".

The developed analysis scripts to quantify substrate deformation and apply it to the cells provides the tools to measure exactly this. Independently of measuring mechanical properties, this can be used to relate the strain magnitude that a cell feels to certain functions. Here we show that for cell death (measured by serendipity when cells died by the force applied) - but it can be extended to studies of mechanotransduction.

#### 4.1.6 "All models are wrong but some are useful"

The ability to calculate and map strains on cells with the 3D stretcher will enable a whole range of studies in the area of mechanotransduction. However, the interpretation of the cellular and nuclear deformation to quantify or make statements about the mechanical properties of the cells is equally important. Many parameters can be extracted from the observed deformation, but the interpretation of these parameters is still model dependent. Already, the accuracy in the interpolation of the cell within the substrate serves as a quantity of the way the cell is embedded and deformed within the substrate: if the position of the cells can be completely predicted by the substrate deformation it means that i. cells are perfectly attached to the substrate and ii. cells exhibit a similar bulk stiffness to the substrate stiffness. The error in the prediction can be attributed to a decrease on stiffness but also to a lower attachment of the cells to the substrate, the actual measurement of adhesion sites distribution on the cells would clarify this point. Integration of this information at the modeling level would allow us to better interpret the changes in stiffness. The same lines of reasoning apply to the modeling of force transduction inside the cells. A higher degree of error in the interpolation in the nuclei points to structural constraints in the cell interior e.g. by protection of the cytoskeleton. These constraints are not taken into consideration in the homogeneous and isotropic models employed for the propagation of the deformation inside the cell, however these models can be expanded in future steps to include a more detailed information (e.g. including internal cytoskeleton structure) so that they are able to explain the changes observed. Again, an interplay between the observations of the models pointing to sensible experiments and expanding the models with the insight gained with the experimental data is what

makes experimental and model based frameworks valuable.

## 4.2 On the insight learned from the comparative studies

### 4.2.1 Nuclear compressibility in LMNA mutants<sup>1</sup>

The comparative study between wild and LMNA<sup>-/-</sup> MEFs revealed an increase in compressibility, measured by a significant lower Poisson's ratio, of the nuclear interior in LMNA<sup>-/-</sup> cells. In a first stance, the measure of compressibility characterizes the ability of a material to preserve or change its volume in a deformed state. Besides the global influence on the volume of a deformed body, the Poisson's ratio  $\nu$  has an effect on the local spatial distribution of the displacement. Since measurements of the nuclear volume from 3D microscopic images are associated with inaccuracy due to imprecision of threshold-based image segmentation, our method for determining  $\nu$  is based on the analysis of its local effects on the displacement of the nuclear interior. Previous studies focused on the analysis of compressibility of the entire nucleus as a one single material in terms of an apparent Poisson's ratio ( $\nu_a = -\epsilon_{lateralstrain}/\epsilon_{axialstrain}$ ) calculated from geometrical reconstruction of change in the nuclear shape.  $\nu$  values ranging from 0.3 to 0.5 have been measured for chondrocytes [Ofek et al., 2009, Leipzig and Athanasiou, 2008]. While the apparent Poisson's ratio characterizes an effective compressibility of a one-material approximation of the entire nucleus as whole,  $\nu$  values determined in the present work describe exclusively the compressibility of the nuclear interior, i.e., stained chromatin embedded in the nucleoplasm. The nuclear membrane, which also contributes to the overall mechanical behavior of the nucleus, was excluded from the computation of the Poisson's ratio in our approach. From this point of view, the effective compressibility of the entire nucleus computed from observation of changes in overall nuclear contours and the Poisson's ratio of the nuclear interior determined in this work by analyzing displacements of inner nuclear domain represent two different quantities. Nevertheless, our experimental results are in good agreement with the previous observations that a wild type fibroblast cell nucleus can be described as a low compressible material [Guilak et al., 2000, Vaziri et al., 2006].

---

<sup>1</sup>Section adapted from [González Avalos et al., 2011]

Higher nuclear compressibility in the mutant cells can be ascribed to alterations of constitutive properties of the major nuclear components, i.e. nucleoplasm and/or chromatin, due to the deficiency in the nuclear lamina. Compressibility of composite materials, such as biological matter, depends on the amount of water, the size of macromolecules and other microstructural properties. As we did not measure changes in the diffusion coefficient of GFP between wild type and mutant cells, we cannot point to specific changes in the viscosity of the nuclear interior. However, this still cannot be ruled out because viscosity measurements based on diffusion are highly dependent on the size of the particle diffusing and we might be missing the scaling at which the changes are happening.

Nevertheless, the analysis of the 3D nuclear shape showed that the mutant nuclei exhibit much stronger deformations, and thus, cannot maintain their round shape under the impact of forces triggered by the disruption of cytoskeletal support. From this observation, we postulate higher structural flexibility of the chromatin in the mutant nuclei in comparison to the normal cells, which in turn may have an impact onto the epigenetic machinery of intranuclear information processing. Similar changes in chromatin deformability have been measured with rheology techniques in the context of human embryonic stem cell differentiation, where an increase in nuclear rigidity was linked to higher LMNA expression, cell differentiation and loss of genomic plasticity [Pajerowski et al., 2007]. This agrees with the assumption that the lamin proteins are an important element to maintain mechanical integrity of chromatin-bearing nuclei [Hutchison, 2002].

But above all, the resulting measurements published in [González Avalos et al., 2011] showed merely an application as proof of principle of our image- and model-based framework for probing the compressibility of the nuclear interior in situ. In general, this method can be adopted to contact less measurement of dimensionless material parameters of arbitrary stainable intracellular subregions that do not necessarily need to be enclosed by membranes. With the introduction of bleaching patterns on fluorescently labeled structures, this technique is not constrained by naturally appearing gradients.

### 4.2.2 Differences in mechanical behavior in pmHC EMT

Characterizing the mechanical changes related to EMT was the main motivation of the development of the methods in 3D. The analysis of this cell system can provide an understanding on the basis of the drastic mechanical, structural and morphological changes in cellular and nuclear properties that cells have to achieved in order to gain the new biological functions necessary for malignant transformation [Suresh, 2007, Wirtz et al., 2011]. And while many research efforts have been concentrated on the effects of changes in the ECM mechanical properties [Pathak and Kumar, 2011], no efforts have been attempted to characterize the changes in mechanical behavior of the cells themselves. Characterizing changes in nuclear mechanical properties is of particular importance, as the nucleus is the biggest and stiffest organelle of the cell and its coordination and interactions with the cytoskeleton are a crucial step affecting cell polarity, shape, and migration efficiency [Friedl et al., 2010].

On a first step, changes in morphological parameters of the cells and specially the nuclei were quantified. Although the cell shape differences are obvious by pure microscopic imaging, changes in nuclear morphology only became apparent after 3D-reconstruction of their surfaces. After this differences were captured, we used the *Nuclear compressibility* framework to measure a decrease of the compressibility of the nuclear interior in nuclei of dedifferentiated hepatocytes. Comparing the measures of both the shape, as well as the compressibility of the nuclei, we can see that not only the shape of the nuclei, but also its mechanical behavior moves towards the one observed in fibroblast cells. If, as in the case of wild type and LMNA<sup>-/-</sup> cells, compressibility of the nuclear interior is interpreted as a measure of damage resistance of the nuclear interior (i.e. chromatin structures) towards deformations, this stronger resistance against forces would render the cells with the required resistance to survive in a more mechanical aggressive environment (stiffer ECM).

Indeed, a stronger resistance to stress was observed in the cells after EMT. TGF- $\beta$  treated cells seem able to endure higher deformations of the substrate before damage is observed. This protection might be attributed to the formation of actin stress fibers supporting the cellular structural stability. Before treatment, cell bundles of epithelial cells can acquire mechanical resistance by reinforcement of their cytoskeleton at cell to cell contacts. Indeed, cell bundles seem to stay in a me-

chanical continuum when deformed. When this sort of protection is lost, reinforcement of the cytoskeleton with stress fibers and around the nucleus might provide more mechanical protection to individual mesenchymal-like cells. The enhanced cytoskeleton could also explain the observed better integration of the nucleus within the treated cells.

Although still at a qualitative level, this preliminary observations already relate the observed morphological and structural changes to the changes in mechanical behavior expected to be necessary during the process of malignant transformation. Expanding this study and integrating it with the molecular understanding of cancer biology, will enable us to not only describe, but to better understand the mechanisms by which tumor cells modulate their mechanical responses and phenotype towards changes in their environment.





## Related publications

The results of the first part of this work were published in following papers:

- **González Avalos, P.**, Gladilin, E., Reichenzeller, M. & Eils, R. Contactless investigation of nuclear mechanics of normal and lamin mutant cells using a 3D image- and model-based framework. *Proceedings of the ASME 2009 Summer Bioengineering Conference* (2009)
- **González Avalos, P.**, Reichenzeller, M., Eils, R. & Gladilin, E. Probing compressibility of the nuclear interior in wild-type and lamin deficient cells using microscopic imaging and computational modeling. *Journal of Biomechanics* 44, 2642–2648 (2011).

An manuscript compiling the second part of the work is currently in preparation:

- **González Avalos, P.**, Mürnseer, M., Dooley, S., Gladilin, E. & Eils, R., Experimental and numerical framework for generation and quantification of cell deformations in 3D substrates. (2012), in preparation





## References

- [Abney et al., 1997] Abney, J. R., Cutler, B., Fillbach, M. L., Axelrod, D., and Scalettar, B. A. (1997). Chromatin dynamics in interphase nuclei and its implications for nuclear structure. *The Journal of cell biology*, 137(7):1459–1468.
- [Affonze and Lutchen, 2006] Affonze, D. A. and Lutchen, K. R. (2006). New perspectives on the mechanical basis for airway hyperreactivity and airway hypersensitivity in asthma. *J Appl Physiol*, 101(6):1710–1719.
- [Albini and Sporn, 2007] Albini, A. and Sporn, M. B. (2007). The tumour microenvironment as a target for chemoprevention. *Nature reviews Cancer*, 7(2):139–147.
- [Andres and Gonzalez, 2009] Andres, V. and Gonzalez, J. (2009). Role of A-type lamins in signaling, transcription, and chromatin organization. *The Journal of cell biology*, 187(7):945.
- [Asnacios and Hamant, 2012] Asnacios, A. and Hamant, O. (2012). The mechanics behind cell polarity. *Trends in cell biology*.
- [Baum et al., 2008] Baum, B., Settleman, J., and Quinlan, M. P. (2008). Transitions between epithelial and mesenchymal states in development and disease. *Seminars in cell & developmental biology*, 19(3):294–308.
- [Beaudouin et al., 2006] Beaudouin, J., Mora-Bermudez, F., Klee, T., and Daigle, N. (2006). Dissecting the Contribution of Diffusion and Interactions to the Mobility of Nuclear Proteins. *Biophysical Journal*.
- [Beil et al., 2005] Beil, M., Braxmeier, H., Fleischer, F., Schmidt, V., and Walther, P. (2005). Quantitative analysis of keratin filament networks in scanning electron microscopy images of cancer cells. *Journal of Microscopy*, 220(2):84–95.
- [Boal, 2002] Boal, D. (2002). *Mechanics of the Cell*. Cambridge University Press, Cambridge, first edition.
- [Boerma et al., 2005] Boerma, M., van der Wees, C., Vrieling, H., Svensson, J., Wondergem, J., van der Laarse, A., Mullenders, L., and van Zeeland, A. (2005). Microarray analysis of gene expression profiles of cardiac myocytes and fibroblasts after mechanical stress, ionising or ultraviolet radiation. *BMC Genomics*, 6(6):1471–2164.
- [Boisvert et al., 2007] Boisvert, F.-M., Van Koningsbruggen, S., Navascués, J., and Lamond, A. I. (2007). The multifunctional nucleolus. *Nature reviews Molecular cell biology*, 8(7):574–585.
- [Brangwynne et al., 2006] Brangwynne, C. P., MacKintosh, F. C., Kumar, S., Geisse, N. A., Talbot, J., Mahadevan, L., Parker, K. K., Ingber, D. E., and Weitz, D. A. (2006). Microtubules can bear enhanced compressive loads in living cells because of lateral reinforcement. *The Journal of cell biology*, 173(5):733–741.

- [Broers, 2004] Broers, J. L. (2004). Decreased mechanical stiffness in LMNA-/- cells is caused by defective nucleo-cytoskeletal integrity: implications for the development of laminopathies. *Human Molecular Genetics*, 13(21):2567–2580.
- [Burke and Stewart, 2002] Burke, B. and Stewart, C. (2002). Life at the edge: the nuclear envelope and human disease. *Nature reviews Molecular cell biology*.
- [Byfield et al., 2004] Byfield, F. J., Aranda-Espinoza, H., Romanenko, V. G., Rothblat, G. H., and Levitan, I. (2004). Cholesterol depletion increases membrane stiffness of aortic endothelial cells. *Biophysical Journal*, 87(5):3336–3343.
- [Caille et al., 1998] Caille, N., Tardy, Y., and Meister, J. J. (1998). Assessment of strain field in endothelial cells subjected to uniaxial deformation of their substrate. *Annals of biomedical engineering*, 26(3):409–416.
- [Caille et al., 2002a] Caille, N., Thoumine, O., Tardy, Y., and Meister, J. (2002a). Contribution of the nucleus to the mechanical properties of endothelial cells. *Journal of Biomechanics*, 35(2):177.
- [Caille et al., 2002b] Caille, N., Thoumine, O., Tardy, Y., and Meister, J.-J. (2002b). Contribution of the nucleus to the mechanical properties of endothelial cells. *Journal of Biomechanics*, 35(2):177–187.
- [Capell and Collins, 2006] Capell, B. C. and Collins, F. S. (2006). Human laminopathies: nuclei gone genetically awry. *Nature reviews Genetics*, 7(12):940–952.
- [Chandran and Barocas, 2006] Chandran, P. L. and Barocas, V. H. (2006). Affine versus non-affine fibril kinematics in collagen networks: theoretical studies of network behavior. *Journal of Biomechanical Engineering*, 128(2):259–270.
- [Chang and Goldman, 2004] Chang, L. and Goldman, R. D. (2004). Intermediate filaments mediate cytoskeletal crosstalk. *Nature reviews Molecular cell biology*, 5(8):601–613.
- [Cheng et al., 2006] Cheng, C., Tempel, D., van Haperen, R., van der Baan, A., Grosveld, F., Daemen, M. J. A. P., Krams, R., and de Crom, R. (2006). Atherosclerotic lesion size and vulnerability are determined by patterns of fluid shear stress. *Circulation*, 113(23):2744–2753.
- [Chowdhury et al., 2009] Chowdhury, F., Na, S., Li, D., Poh, Y., Tanaka, T., Wang, F., and Wang, N. (2009). Material properties of the cell dictate stress-induced spreading and differentiation in embryonic stem cells. *Nature materials*.
- [Claessens et al., 2006] Claessens, M. M. A. E., Bathe, M., Frey, E., and Bausch, A. R. (2006). Actin-binding proteins sensitively mediate F-actin bundle stiffness. *Nature materials*, 5(9):748–753.
- [Cohen et al., 2004] Cohen, D., Brennwald, P. J., Rodriguez-Boulan, E., and Müsch, A. (2004). Mammalian PAR-1 determines epithelial lumen polarity by organizing the microtubule cytoskeleton. *The Journal of cell biology*, 164(5):717–727.

- [Conrad et al., 2011] Conrad, C., Wünsche, A., Tan, T. H., Bulkescher, J., Sieckmann, F., Verissimo, F., Edelstein, A., Walter, T., Liebel, U., Pepperkok, R., and Ellenberg, J. (2011). Micropilot: automation of fluorescence microscopy-based imaging for systems biology. *Nature methods*, 8(3):246–249.
- [Costa et al., 2006] Costa, K. D., Sim, A. J., and Yin, F. C.-P. (2006). Non-Hertzian approach to analyzing mechanical properties of endothelial cells probed by atomic force microscopy. *Journal of Biomechanical Engineering*, 128(2):176–184.
- [Cremer and Cremer, 2001] Cremer, T. and Cremer, C. (2001). Chromosome territories, nuclear architecture and gene regulation in mammalian cells. *Nature reviews Genetics*, 2(4):292–301.
- [Cremer et al., 2006] Cremer, T., Cremer, M., Dietzel, S., Müller, S., Solovei, I., and Fakan, S. (2006). Chromosome territories—a functional nuclear landscape. *Current Opinion in Cell Biology*, 18(3):307–316.
- [Crisp and Burke, 2008] Crisp, M. and Burke, B. E. (2008). The nuclear envelope as an integrator of nuclear and cytoplasmic architecture. *FEBS Letters*, 582(14):2023–2032.
- [Crocker and Hoffman, 2007] Crocker, J. C. and Hoffman, B. D. (2007). Multiple-particle tracking and two-point microrheology in cells. *Methods in cell biology*, 83:141–178.
- [Cukierman et al., 2001] Cukierman, E., Pankov, R., Stevens, D. R., and Yamada, K. M. (2001). Taking cell-matrix adhesions to the third dimension. *Science (New York, NY)*, 294(5547):1708–1712.
- [Dahl, 2005] Dahl, K. N. (2005). Power-Law Rheology of Isolated Nuclei with Deformation Mapping of Nuclear Substructures. *Biophysical Journal*, 89(4):2855–2864.
- [Dahl et al., 2004] Dahl, K. N., Kahn, S., Wilson, K., and Discher, D. E. (2004). The nuclear envelope lamina network has elasticity and a compressibility limit suggestive of a . . . . *Journal of cell science*.
- [de Vries et al., 2007] de Vries, A. H. B., Krenn, B. E., Van Driel, R., Subramaniam, V., and Kanger, J. S. (2007). Direct observation of nanomechanical properties of chromatin in living cells. *Nano letters*, 7(5):1424–1427.
- [Decaens et al., 2008] Decaens, C., Durand, M., Grosse, B., and Cassio, D. (2008). Which in vitro models could be best used to study hepatocyte polarity? *Biology of the Cell*, 100(7):387.
- [Dechat et al., 2008] Dechat, T., Pflieger, K., Sengupta, K., Shimi, T., Shumaker, D. K., Solimando, L., and Goldman, R. D. (2008). Nuclear lamins: major factors in the structural organization and function of the nucleus and chromatin. *Genes & development*, 22(7):832–853.
- [Dellaire and Bazett-Jones, 2004] Dellaire, G. and Bazett-Jones, D. P. (2004). PML nuclear bodies: dynamic sensors of DNA damage and cellular stress. *BioEssays : news and reviews in molecular, cellular and developmental biology*, 26(9):963–977.
- [Dufort et al., 2011] Dufort, C. C., Paszek, M. J., and Weaver, V. M. (2011). Balancing forces: architectural control of mechanotransduction. *Nature Publishing Group*, 12(5):308–319.

- [Dundr and Misteli, 2001] Dundr, M. and Misteli, T. (2001). Functional architecture in the cell nucleus. *The Biochemical journal*, 356(Pt 2):297–310.
- [Dupin et al., 2011] Dupin, I., Sakamoto, Y., and Etienne-Manneville, S. (2011). Cytoplasmic intermediate filaments mediate actin-driven positioning of the nucleus. *Journal of cell science*, 124(6):865–872.
- [Eckl and Bresgen, 2003] Eckl, P. and Bresgen, N. (2003). The cultured primary hepatocyte and its application in toxicology. *Journal of Applied Biomedicine*, 1:117–126.
- [Engler et al., 2006] Engler, A. J., Sen, S., Sweeney, H. L., and Discher, D. E. (2006). Matrix elasticity directs stem cell lineage specification. *Cell*, 126(4):677–689.
- [Fernández et al., 2006] Fernández, P., Pullarkat, P. A., and Ott, A. (2006). A master relation defines the nonlinear viscoelasticity of single fibroblasts. *Biophysical Journal*, 90(10):3796–3805.
- [Fletcher and Mullins, 2010] Fletcher, D. A. and Mullins, R. D. (2010). Cell mechanics and the cytoskeleton. *Nature*, 463(7280):485–492.
- [Fraser and Bickmore, 2007] Fraser, P. and Bickmore, W. (2007). Nuclear organization of the genome and the potential for gene regulation. *Nature*, 447(7143):413–417.
- [Friedl et al., 2010] Friedl, P., Wolf, K., and Lammerding, J. (2010). Nuclear mechanics during cell migration. *Current Opinion in Cell Biology*, pages 1–10.
- [Gall, 2000] Gall, J. G. (2000). The centennial of the Cajal body. *Science (New York, NY)*, 290:1567–1570.
- [Gardel et al., 2004] Gardel, M. L., Shin, J. H., MacKintosh, F. C., Mahadevan, L., Matsudaira, P., and Weitz, D. A. (2004). Elastic behavior of cross-linked and bundled actin networks. *Science (New York, NY)*, 304(5675):1301–1305.
- [Gavara et al., 2008] Gavara, N., Roca-Cusachs, P., Sunyer, R., Farré, R., and Navajas, D. (2008). Mapping cell-matrix stresses during stretch reveals inelastic reorganization of the cytoskeleton. *Biophysical Journal*, 95(1):464–471.
- [Gilchrist et al., 2007] Gilchrist, C., Witvoet-Braam, S., Guilak, F., and Setton, L. (2007). Measurement of intracellular strain on deformable substrates with texture correlation. *Journal of Biomechanics*, 40(4):786–794.
- [Gladilin and Eils, 2008] Gladilin, E. and Eils, R. (2008). Nonlinear elastic model for image registration and soft tissue simulation based on piecewise St. Venant-Kirchhoff material approximation. *Proceedings of SPIE*, 6914:69142O.
- [Gladilin et al., 2007] Gladilin, E., Micoulet, A., Hosseini, B., Rohr, K., Spatz, J. P., and Eils, R. (2007). 3D finite element analysis of uniaxial cell stretching: from image to insight. *Physical Biology*, 4(2):104–113.
- [Gladilin et al., 2010] Gladilin, E., Schulz, M., Kappel, C., and Eils, R. (2010). Contactless determination of nuclear compressibility using 3D image- and model-based analysis of drug-induced cellular deformation. *Journal of Microscopy*, 240(3):216–226.

- [Godoy et al., 2009] Godoy, P., Hengstler, J., Ilkavets, I., Meyer, C., Bachmann, A., Müller, A., Tuschl, G., Mueller, S., and Dooley, S. (2009). Extracellular matrix modulates sensitivity of hepatocytes to fibroblastoid dedifferentiation and transforming growth factor  $\beta$ -induced apoptosis. *Hepatology (Baltimore, Md)*, 49(6):2031–2043.
- [Goldman et al., 1996] Goldman, R. D., Khuon, S., Chou, Y. H., Opal, P., and Steinert, P. M. (1996). The function of intermediate filaments in cell shape and cytoskeletal integrity. *The Journal of cell biology*, 134(4):971–983.
- [Gonzalez, 2008] Gonzalez, P. (2008). *Nuclear mechanics of lamin mutants*. PhD thesis, University of Heidelberg.
- [Gonzalez et al., 2009] Gonzalez, P., Gladilin, E., Reichenzeller, M., and Eils, R. (2009). Contactless investigation of nuclear mechanics of normal and lamin mutant cells using a 3D image- and model-based framework. *Proceedings of the ASME 2009 Summer Bioengineering Conference*.
- [González Avalos et al., 2011] González Avalos, P., Reichenzeller, M., Eils, R., and Gladilin, E. (2011). Probing compressibility of the nuclear interior in wild-type and lamin deficient cells using microscopic imaging and computational modeling. *Journal of Biomechanics*, 44(15):2642–2648.
- [Gotzmann et al., 2006] Gotzmann, J., Fischer, A., Zojer, M., Mikula, M., Proell, V., Huber, H., Jechlinger, M., Waerner, T., Weith, A., and Beug, H. (2006). A crucial function of PDGF in TGF- $\beta$ -mediated cancer progression of hepatocytes. *Oncogene*, 25(22):3170–3185.
- [Grabowska et al., 2011] Grabowska, I., Szeliga, A., Moraczewski, J., Czaplicka, I., and Brzóška, E. (2011). Comparison of satellite cell-derived myoblasts and C2C12 differentiation in two- and three-dimensional cultures: changes in adhesion protein expression. *Cell biology international*, 35(2):125–133.
- [Griffith and Swartz, 2006] Griffith, L. G. and Swartz, M. A. (2006). Capturing complex 3D tissue physiology in vitro. *Nature reviews Molecular cell biology*, 7(3):211–224.
- [Gruenbaum et al., 2005] Gruenbaum, Y., Margalit, A., Goldman, R. D., Shumaker, D. K., and Wilson, K. L. (2005). The nuclear lamina comes of age. *Nature reviews Molecular cell biology*, 6(1):21–31.
- [Grünert et al., 2003] Grünert, S., Jechlinger, M., and Beug, H. (2003). Diverse cellular and molecular mechanisms contribute to epithelial plasticity and metastasis. *Nature reviews Molecular cell biology*, 4(8):657–665.
- [Guck et al., 2005] Guck, J., Schinkinger, S., Lincoln, B., Wottawah, F., Ebert, S., Romeyke, M., Lenz, D., Erickson, H. M., Ananthakrishnan, R., Mitchell, D., Käs, J., Ulvick, S., and Bilby, C. (2005). Optical deformability as an inherent cell marker for testing malignant transformation and metastatic competence. *Biophysical Journal*, 88(5):3689–3698.
- [Guilak, 1995] Guilak, F. (1995). Compression-induced changes in the shape and volume of the chondrocyte nucleus. *Journal of Biomechanics*, 28(12):1529–1541.

- [Guilak et al., 2000] Guilak, F., Tedrow, J., and Burgkart, R. (2000). Viscoelastic Properties of the Cell Nucleus. *Biochemical and biophysical research communications*.
- [Hall, 2009] Hall, A. (2009). The cytoskeleton and cancer. *Cancer metastasis reviews*, 28(1-2):5–14.
- [Heidemann and Wirtz, 2004] Heidemann, S. and Wirtz, D. (2004). Towards a regional approach to cell mechanics. *Trends in cell biology*.
- [Herrmann et al., 2007] Herrmann, H., Bär, H., Kreplak, L., Strelkov, S. V., and Aebi, U. (2007). Intermediate filaments: from cell architecture to nanomechanics. *Nature reviews Molecular cell biology*, 8(7):562–573.
- [Herrmann et al., 2009] Herrmann, H., Strelkov, S., Burkhard, P., and Aebi, U. (2009). Intermediate filaments: primary determinants of cell architecture and plasticity.
- [Hochmuth, 2000] Hochmuth, R. (2000). Micropipette aspiration of living cells. *Journal of Biomechanics*, 33(1):15–22.
- [Hoffman et al., 2011] Hoffman, B. D., Grashoff, C., and Schwartz, M. A. (2011). Dynamic molecular processes mediate cellular mechanotransduction. *Nature*, 475(7356):316–323.
- [Hornberger et al., 2005] Hornberger, T. A., Armstrong, D. D., Koh, T. J., Burkholder, T. J., and Esser, K. A. (2005). Intracellular signaling specificity in response to uniaxial vs. multiaxial stretch: implications for mechanotransduction. *American Journal of Physiology- Cell Physiology*, 288(1):C185–94.
- [Huang et al., 2010] Huang, L., Mathieu, P. S., and Helmke, B. P. (2010). A stretching device for high-resolution live-cell imaging. *Annals of biomedical engineering*, 38(5):1728–1740.
- [Hutchison, 2002] Hutchison, C. J. (2002). Lamins: building blocks or regulators of gene expression? *Nature reviews Molecular cell biology*, 3(11):848–858.
- [Hutchison and Worman, 2004] Hutchison, C. J. and Worman, H. J. (2004). A-type lamins: guardians of the soma? *Nature cell biology*, 6(11):1062–1067.
- [Hwang et al., 2006] Hwang, N. S., Varghese, S., Zhang, Z., and Elisseeff, J. (2006). Chondrogenic Differentiation of Human Embryonic Stem Cell-Derived Cells in Arginine-Glycine-Aspartate-Modified Hydrogels. *Tissue engineering*, 12(9):2695–2706.
- [Jaalouk and Lammerding, 2009] Jaalouk, D. E. and Lammerding, J. (2009). Mechanotransduction gone awry. *Nature reviews Molecular cell biology*, 10(1):63–73.
- [Janmey et al., 2007] Janmey, P. A., Georges, P. C., and Hvidt, S. (2007). Basic rheology for biologists. *Methods in cell biology*, 83:3–27.
- [Jean et al., 2004] Jean, R., Gray, D., Spector, A., and Chen, C. S. (2004). Characterization of the Nuclear Deformation Caused by Changes in Endothelial Cell Shape. *Journal of Biomechanical Engineering*, 126:552.

- [Kerssemakers et al., 2006] Kerssemakers, J. W. J., Munteanu, E. L., Laan, L., Noetzel, T. L., Janson, M. E., and Dogterom, M. (2006). Assembly dynamics of microtubules at molecular resolution. *Nature*, 442(7103):709–712.
- [Klein-Nulend et al., 2003] Klein-Nulend, J., Bacabac, R. G., Veldhuijzen, J. P., and Van Loon, J. J. W. A. (2003). Microgravity and bone cell mechanosensitivity. *Advances in space research : the official journal of the Committee on Space Research (COSPAR)*, 32(8):1551–1559.
- [Kole et al., 2004] Kole, T. P., Tseng, Y., Huang, L., Katz, J. L., and Wirtz, D. (2004). Rho kinase regulates the intracellular micromechanical response of adherent cells to rho activation. *Molecular biology of the cell*, 15(7):3475–3484.
- [Korf, 2008] Korf, B. (2008). Hutchinson-Gilford Progeria Syndrome, Aging, and the Nuclear Lamina. *New England Journal of Medicine*.
- [Kumar and Weaver, 2009] Kumar, S. and Weaver, V. M. (2009). Mechanics, malignancy, and metastasis: the force journey of a tumor cell. *Cancer metastasis reviews*, 28(1-2):113–127.
- [Lakes, 1987] Lakes, R. (1987). Foam Structures with a Negative Poisson's Ratio. *Science (New York, NY)*, 235(4792):1038–1040.
- [Lammerding, 2004] Lammerding, J. (2004). Lamin A/C deficiency causes defective nuclear mechanics and mechanotransduction. *Journal of Clinical Investigation*, 113(3):370–378.
- [Lammerding, 2005] Lammerding, J. (2005). Abnormal nuclear shape and impaired mechanotransduction in emerin-deficient cells. *The Journal of cell biology*, 170(5):781–791.
- [Lammerding et al., 2007] Lammerding, J., Dahl, K. N., Discher, D. E., and Kamm, R. D. (2007). Nuclear mechanics and methods. *Methods in cell biology*, 83:269–294.
- [Lammerding et al., 2006] Lammerding, J., Fong, L., Ji, J., Reue, K., and Stewart, C. L. (2006). Lamins A and C but Not Lamin B1 Regulate Nuclear Mechanics. *Journal of Biological Chemistry*.
- [Lammerding and Lee, 2009] Lammerding, J. and Lee, R. (2009). Mechanical properties of interphase nuclei probed by cellular strain application. *Methods Mol. Biol*, 464:13–26.
- [Lamond and Sleeman, 2003] Lamond, A. I. and Sleeman, J. E. (2003). Nuclear substructure and dynamics. *Current biology : CB*, 13(21):R825–8.
- [Lamond and Spector, 2003] Lamond, A. I. and Spector, D. L. (2003). Nuclear speckles: a model for nuclear organelles. *Nature reviews Molecular cell biology*, 4(8):605–612.
- [Le Bellego et al., 2006] Le Bellego, F., Plante, S., Chakir, J., Hamid, Q., and Ludwig, M. (2006). Differences in MAP kinase phosphorylation in response to mechanical strain in asthmatic fibroblasts. *Respiratory Research*, 7:68.
- [Lee et al., 2007] Lee, J. S. H., Hale, C. M., Panorchan, P., Khatau, S. B., George, J. P., Tseng, Y., Stewart, C. L., Hodzic, D., and Wirtz, D. (2007). Nuclear lamin A/C deficiency induces defects in cell mechanics, polarization, and migration. *Biophysical Journal*, 93(7):2542–2552.

- [Leipzig and Athanasiou, 2008] Leipzig, N. D. and Athanasiou, K. A. (2008). Static compression of single chondrocytes catabolically modifies single-cell gene expression. *Biophysical Journal*, 94(6):2412–2422.
- [Lekka et al., 1999] Lekka, M., Laidler, P., Gil, D., Lekki, J., Stachura, Z., and Hryniewicz, A. Z. (1999). Elasticity of normal and cancerous human bladder cells studied by scanning force microscopy. *European Biophysics Journal*, 28(4):312–316.
- [Levental et al., 2006] Levental, I., Georges, P. C., and Janmey, P. A. (2006). Soft biological materials and their impact on cell function. *Soft Matter*.
- [Li et al., 2007] Li, G. N., Livi, L. L., Gourd, C. M., Dewerd, E. S., and Hoffman-Kim, D. (2007). Genomic and Morphological Changes of Neuroblastoma Cells in Response to Three-Dimensional Matrices. *Tissue engineering*, 13(5):1035–1047.
- [Lieber et al., 2004] Lieber, S. C., Aubry, N., Pain, J., Diaz, G., Kim, S.-J., and Vatner, S. F. (2004). Aging increases stiffness of cardiac myocytes measured by atomic force microscopy nanoindentation. *American journal of physiology. Heart and circulatory physiology*, 287(2):H645–51.
- [Lippincott-Schwartz et al., 2001] Lippincott-Schwartz, J., Snapp, E., and Kenworthy, A. (2001). Studying protein dynamics in living cells. *Nature reviews Molecular cell biology*, 2(6):444–456.
- [Lombardi and Lammerding, 2010] Lombardi, M. and Lammerding, J. (2010). Altered Mechanical Properties of the Nucleus in Disease. *Methods in cell biology*, 98:121–141.
- [Lombardi et al., 2011a] Lombardi, M. L., Jaalouk, D. E., Shanahan, C. M., Burke, B., Roux, K. J., and Lammerding, J. (2011a). The interaction between nesprins and sun proteins at the nuclear envelope is critical for force transmission between the nucleus and cytoskeleton. *Journal of Biological Chemistry*, 286(30):26743–26753.
- [Lombardi et al., 2011b] Lombardi, M. L., Zwerger, M., and Lammerding, J. (2011b). Biophysical Assays to Probe the Mechanical Properties of the Interphase Cell Nucleus: Substrate Strain Application and Microneedle Manipulation. *Journal of Visualized Experiments*, (55).
- [Luby-Phelps, 2000] Luby-Phelps, K. (2000). Cytoarchitecture and physical properties of cytoplasm: volume, viscosity, diffusion, intracellular surface area. *International review of cytology*, 192:189–221.
- [Mahaffy et al., 2004] Mahaffy, R., Park, S., Gerde, E., Kas, J., and Shih, C. (2004). Quantitative Analysis of the Viscoelastic Properties of Thin Regions of Fibroblasts Using Atomic . . . . *Biophysical Journal*.
- [Mammoto and Ingber, 2010] Mammoto, T. and Ingber, D. E. (2010). Mechanical control of tissue and organ development. *Development (Cambridge, England)*, 137(9):1407–1420.
- [Maniotis et al., 1997] Maniotis, A. J., Chen, C. S., and Ingber, D. E. (1997). Demonstration of mechanical connections between integrins, cytoskeletal filaments, and nucleoplasm . . . . *Proceedings of the National Academy of Sciences*.



- [Manju et al., 2006] Manju, K., Muralikrishna, B., and Parnaik, V. K. (2006). Expression of disease-causing lamin A mutants impairs the formation of DNA repair foci. *Journal of cell science*, 119(Pt 13):2704–2714.
- [Maraldi et al., 2011] Maraldi, N. M., Capanni, C., Cenni, V., Fini, M., and Lattanzi, G. (2011). Laminopathies and lamin-associated signaling pathways. *Journal of Cellular Biochemistry*, 112(4):979–992.
- [Martins et al., 2012] Martins, R. P., Finan, J. D., Farshid, G., and Lee, D. A. (2012). Mechanical Regulation of Nuclear Structure and Function. *Annual review of biomedical engineering*, 14(1):431–455.
- [McGarry et al., 2005] McGarry, J., Murphy, B., and McHugh, P. (2005). Computational mechanics modelling of cell-substrate contact during cyclic substrate deformation. *Journal Of The Mechanics And Physics Of Solids*, 53(12):2597–2637.
- [Méjat and Misteli, 2010] Méjat, A. and Misteli, T. (2010). LINC complexes in health and disease. *Nucleus*, 1(1):40.
- [Meshel et al., 2005] Meshel, A. S., Wei, Q., Adelstein, R. S., and Sheetz, M. P. (2005). Basic mechanism of three-dimensional collagen fibre transport by fibroblasts. *Nature cell biology*, 7(2):157–164.
- [Mills et al., 2004] Mills, J. P., Qie, L., Dao, M., Lim, C. T., and Suresh, S. (2004). Nonlinear elastic and viscoelastic deformation of the human red blood cell with optical tweezers. *Mechanics & chemistry of biosystems : MCB*, 1(3):169–180.
- [Nagayama et al., 2006] Nagayama, K., Nagano, Y., Sato, M., and Matsumoto, T. (2006). Effect of actin filament distribution on tensile properties of smooth muscle cells obtained from rat thoracic aortas. *Journal of Biomechanics*, 39(2):293–301.
- [Nakamura et al., 2003] Nakamura, T., Kato, Y., Fuji, H., Horiuchi, T., Chiba, Y., and Tanaka, K. (2003). E-cadherin-dependent intercellular adhesion enhances chemoresistance. *International journal of molecular medicine*, 12(5):693–700.
- [Naumanen et al., 2008] Naumanen, P., Lappalainen, P., and Hotulainen, P. (2008). Mechanisms of actin stress fibre assembly. *Journal of Microscopy*, 231(3):446–454.
- [Nekrasova et al., 2011] Nekrasova, O. E., Mendez, M. G., Chernoiivanenko, I. S., Tyurin-Kuzmin, P. A., Kuczmarski, E. R., Gelfand, V. I., Goldman, R. D., and Minin, A. A. (2011). Vimentin intermediate filaments modulate the motility of mitochondria. *Molecular biology of the cell*, 22(13):2282–2289.
- [Ofek et al., 2009] Ofek, G., Natoli, R. M., and Athanasiou, K. A. (2009). In situ mechanical properties of the chondrocyte cytoplasm and nucleus. *Journal of Biomechanics*, 42(7):873–877.
- [Page et al., 2012] Page, H., Flood, P., and Reynaud, E. G. (2012). Three-dimensional tissue cultures: current trends and beyond. *Cell and Tissue Research*.

- [Pajeroski et al., 2007] Pajeroski, J., Dahl, K., Zhong, F., Sammak, P., and Discher, D. (2007). Physical plasticity of the nucleus in stem cell differentiation. *Proceedings of the National Academy of Sciences*, 104(40):15619.
- [Panorchan et al., 2006] Panorchan, P., Lee, J. S. H., Kole, T. P., Tseng, Y., and Wirtz, D. (2006). Microrheology and ROCK signaling of human endothelial cells embedded in a 3D matrix. *Biophysical Journal*, 91(9):3499–3507.
- [Park et al., 2005] Park, S., Koch, D., Cardenas, R., Kas, J., and Shih, C. K. (2005). Cell motility and local viscoelasticity of fibroblasts. *Biophysical Journal*, 89(6):4330–4342.
- [Pathak and Kumar, 2011] Pathak, A. and Kumar, S. (2011). Biophysical regulation of tumor cell invasion: moving beyond matrix stiffness. *Integrative Biology*, 3(4):267.
- [Pedersen and Swartz, 2005] Pedersen, J. A. and Swartz, M. A. (2005). Mechanobiology in the Third Dimension. *Annals of biomedical engineering*, 33(11):1469–1490.
- [Pederson, 2000] Pederson, T. (2000). Half a Century of "The Nuclear Matrix". *Molecular biology of the cell*, 11(3):799.
- [Peeters et al., 2005] Peeters, E. A. G., Oomens, C. W. J., Bouten, C. V. C., Bader, D. L., and Baaijens, F. P. T. (2005). Viscoelastic properties of single attached cells under compression. *Journal of Biomechanical Engineering*, 127(2):237–243.
- [Peretz et al., 2007] Peretz, H., Talpalar, A. E., and Vago, R. (2007). Superior survival and durability of neurons and astrocytes on 3-dimensional aragonite biomatrices. *Tissue engineering*.
- [Richard et al., 2007] Richard, M. N., Deniset, J. F., Kneesh, A. L., Blackwood, D., and Pierce, G. N. (2007). Mechanical stretching stimulates smooth muscle cell growth, nuclear protein import, and nuclear pore expression through mitogen-activated protein kinase activation. *The Journal of biological chemistry*, 282(32):23081–23088.
- [Rowat et al., 2008] Rowat, A. C., Lammerding, J., Herrmann, H., and Aebi, U. (2008). Towards an integrated understanding of the structure and mechanics of the cell nucleus. *BioEssays: news and reviews in molecular, cellular and developmental biology*, 30(3):226–236.
- [Rowat et al., 2006] Rowat, A. C., Lammerding, J., and Ipsen, J. H. (2006). Mechanical properties of the cell nucleus and the effect of emerin deficiency. *Biophysical Journal*, 91(12):4649–4664.
- [Schenk and Guest, 2011] Schenk, M. and Guest, S. D. (2011). Origami folding: A structural engineering approach. page 291.
- [Stroka et al., 2012] Stroka, K. M., Vaitkus, J. A., and Aranda-Espinoza, H. (2012). Endothelial cells undergo morphological, biomechanical, and dynamic changes in response to tumor necrosis factor- $\alpha$ . *European Biophysics Journal*.
- [Sullivan et al., 1999] Sullivan, T., Escalante-Alcalde, D., Bhatt, H., Anver, M., Bhat, N., Nagashima, K., Stewart, C. L., and Burke, B. E. (1999). Loss of A-type lamin expression compromises nuclear envelope integrity leading to muscular dystrophy. *The Journal of cell biology*, 147(5):913–920.

- [Suresh, 2007] Suresh, S. (2007). Biomechanics and biophysics of cancer cells. *Acta Materialia*.
- [Takai et al., 2005] Takai, E., Costa, K. D., Shaheen, A., Hung, C. T., and Guo, X. E. (2005). Osteoblast elastic modulus measured by atomic force microscopy is substrate dependent. *Annals of biomedical engineering*, 33(7):963–971.
- [Tan et al., 2008] Tan, W., Scott, D., Belchenko, D., Qi, H. J., and Xiao, L. (2008). Development and evaluation of microdevices for studying anisotropic biaxial cyclic stretch on cells. *Biomedical microdevices*, 10(6):869–882.
- [Trickey et al., 2006] Trickey, W., Baaijens, F., and Laursen, T. (2006). Determination of the Poisson’s ratio of the cell: recovery properties of chondrocytes after release . . . . *Journal of Biomechanics*.
- [Trickey et al., 2004] Trickey, W. R., Vail, T. P., and Guilak, F. (2004). The role of the cytoskeleton in the viscoelastic properties of human articular chondrocytes. *Journal of orthopaedic research : official publication of the Orthopaedic Research Society*, 22(1):131–139.
- [Tseng et al., 2004] Tseng, Y., Lee, J. S. H., Kole, T. P., Jiang, I., and Wirtz, D. (2004). Microorganization and visco-elasticity of the interphase nucleus revealed by particle nanotracking. *Journal of cell science*, 117(Pt 10):2159–2167.
- [Tsukada and Phillips, 1993] Tsukada, N. and Phillips, M. J. (1993). Bile canalicular contraction is coincident with reorganization of pericanalicular filaments and co-localization of actin and myosin-II. *The journal of histochemistry and cytochemistry : official journal of the Histochemistry Society*, 41(3):353–363.
- [Vaziri and Gopinath, 2007] Vaziri, A. and Gopinath, A. (2007). Cell and biomolecular mechanics in silico. *Nature materials*.
- [Vaziri et al., 2006] Vaziri, A., Lee, H., and Kaazempur Mofrad, M. (2006). Deformation of the cell nucleus under indentation: Mechanics and mechanisms. *Journal of Materials Research*.
- [Verstraeten et al., 2008] Verstraeten, V. L. R. M., Ji, J. Y., Cummings, K. S., Lee, R. T., and Lammerding, J. (2008). Increased mechanosensitivity and nuclear stiffness in Hutchinson–Gilford progeria cells: effects of farnesyltransferase inhibitors. *Aging Cell*, 7(3):383–393.
- [Verstraeten and Lammerding, 2008] Verstraeten, V. L. R. M. and Lammerding, J. (2008). Experimental techniques for study of chromatin mechanics in intact nuclei and living cells. *Chromosome Research*.
- [Walker and Brugge, 2006] Walker, S. J. and Brugge, J. S. (2006). SePARating polarity and proliferation in ErbB2 oncogenesis. *Nature cell biology*, 8(11):1220–1222.
- [Wall et al., 2007] Wall, M., Weinhold, P., Siu, T., Brown, T., and Banes, A. (2007). Comparison of cellular strain with applied substrate strain in vitro. *Journal of Biomechanics*, 40(1):173–181.
- [Weihs et al., 2006] Weihs, D., Mason, T. G., and Teitell, M. A. (2006). Bio-microrheology: a frontier in microrheology. *Biophysical Journal*, 91(11):4296–4305.

## References

---

- [Wendt et al., 2009] Wendt, M., Allington, T., and Schiemann, W. (2009). Mechanisms of the epithelial-mesenchymal transition by TGF- $\beta$ . *Future Oncol.*, 5(8):1145–1168.
- [Wiche, 1998] Wiche, G. (1998). Role of plectin in cytoskeleton organization and dynamics. *Journal of cell science*, 111 ( Pt 17):2477–2486.
- [Wirtz et al., 2011] Wirtz, D., Konstantopoulos, K., and Searson, P. C. (2011). The physics of cancer: the role of physical interactions and mechanical forces in metastasis. pages 1–11.
- [Yamada and Cukierman, 2007] Yamada, K. M. and Cukierman, E. (2007). Modeling tissue morphogenesis and cancer in 3D. *Cell*, 130(4):601–610.
- [Yu et al., 2011] Yu, H., Mouw, J. K., and Weaver, V. M. (2011). Forcing form and function: biomechanical regulation of tumor evolution. *Trends in cell biology*, 21(1):47–56.

# Appendix 1: Example of ImageJ Plugin

```
1 //
  

---



---


2 // ImageJ Plugin to open, filter and segment complete image
  time series
3 // PGA – October 2009
4 //
  

---



---


5
6 class ImageNameFilter_ implements FilenameFilter {
7 public boolean accept(java.io.File f, java.lang.String name) {
8 return (name.endsWith(".tif")|name.endsWith(".pgm"));
9 }
10 }
11
12 public class Open_Filter_Bin_Stretcher implements PlugIn {
13
14 public void run(String arg) {
15
16 //Stuff needed to get files from a desired directory
17
18 final Frame f = new Frame();
19 final JFileChooser chooser = new JFileChooser();
20 String path= "";
21 String name= "";
22 File file = null;
23 String timepoint = "t";
24 String imgname = "";
25 Opener o = new Opener();
26
27 chooser.setFileHidingEnabled(true);
28 chooser.setMultiSelectionEnabled(false);
29 chooser.setSelectionMode(JFileChooser.DIRECTORIES_ONLY);
30
31 chooser.setDialogType(JFileChooser.OPEN_DIALOG);
```

---

```

32
33  int state = chooser.showDialog(f, "Select_Directory");    //
      select time series directory
34
35  if (state == JFileChooser.APPROVE_OPTION )
36  {
37    file = chooser.getSelectedFile ();
38  }
39  path = file.getAbsolutePath ();          // save the path of
      the directory as string
40  name = file.getName ();                // save the name of the
      directory as string e.g. "MEFko_1"
41  IJ.write(path);                        // check if you have the correct
      path
42  String[] dirs = file.list ();          // get the list of the
      files&folders and save as a string
43  for (int i =0; i< (dirs.length); i++){ // loop for each
      file & folder
44    if (dirs[i].substring(0,1).equals(timepoint)) { // only if
      the directory starts with a "t" (the timepoint folders)
45    IJ.write("processing..." + dirs[i]); // print out the
      names of the time point, that is being analysed
46    //String tppath = path + "/" + dirs[i]; //save the
      complete path of the time point folder as String
47    String rawpath = path + "/" + dirs[i]+ "/" +"Raw"+ "/" + "
      Nucleus"; //save the complete path of the "Raw" folder ,
      containing the images
48
49    File tp = new File(rawpath);        //make the Raw Folder into
      a Java File
50    //String[] rfiles = tp.list ();     //extract the list of
      images inside the folder (as list of strings)
51
52
53    FilenameFilter filter = new ImageNameFilter_(); //extract
      the list of images (= files which end in tif or pgm)
      inside the folder (as list of strings)
54
55    String[] rimages = tp.list(filter);
56
57    imgname = rawpath + "/" +rimages[0]; //create a new
      empty stack , with the properties of the first image (

```

```

    size + type)
58 ImagePlus imp = o.openImage(ingname);
59 ImageStack rawstack = imp.createEmptyStack();
60
61 for (int k = 0; k<(rimages.length);k++) {           // add
    each image to the empty stack
62
63 ingname = rawpath + "/" +rimages[k];           // get the
    full path of the images
64 ImagePlus imps = o.openImage(ingname);           // use the path
    to open the images as a new image plus
65 ImageProcessor ip = imps.getProcessor(); // get processor
66 String label = imps.getTitle(); // get label
67 rawstack.addSlice(label, ip); // add it to the stack
68
69 } // loop for the images
70
71
72 ImagePlus raw = new ImagePlus(name +"_"+ dirs[i], rawstack);
73 //raw.show(); // show the stack
74 new StackConverter(raw).convertToGray8(); // run
    processing steps on raw image stack
75 //IJ.getImage();
76 IJ.run(raw, "Stack_Normalizer", "minimum=0_maximum=255");
77 IJ.run(raw, "Anisotropic_Diffusion_2D", "number=10_
    smoothings=1_a1=0.40_a2=0.90_dt=20_edge=5");
78
79 ImagePlus filt = IJ.getImage(); //recover the processed
    image stack as image plus (i.e. filtered image stack)
80 ImageStack fstack = filt.getImageStack(); //save it as a
    stack
81 int fsize = fstack.getSize(); //get stack size
82
83 String[] fimages = rimages; //create a new array of
    strings to store the names of the filtered images
84 for (int n = 0; n<(rimages.length);n++) {
85     fimages[n] = rimages[n].replace("tif","pgm");
86 }
87
88 try {
89     final FileWriter fr = new FileWriter(path + "/" + dirs[i] +
        "/" +"Filtered"+"/" + "Nucleus" + "/" + dirs[i] + ".

```

---

```

        txt", true); // create txt file with image paths
90  String apath = "../Data" + "/" + name + "/" + dirs[i] + "/"
        + "Filtered" + "/" + "Nucleus" + "/";
91
92  for (int j = 0; j < (fsize); j++) { //store slices of
        the image stack as pgm images
93  ImageProcessor fimagep = fstack.getProcessor(j+1); //
        comment, slice number starts at 1
94  ImagePlus fimage = new ImagePlus("fimagep",fimagep);
95  final FileSaver filtFile = new FileSaver(fimage);
96  final String fpathname = path + "/" + dirs[i]+ "/" +
        Filtered" + "/" + "Nucleus" + "/" + fimages[j];
97  fr.write(apath + fimages[j] + "\n");
98  filtFile.saveAsPgm(fpathname);
99  }
100
101  fr.close();
102
103  } catch (IOException e) {
104  IJ.error("IOException_exception");
105  }
106
107  // here, code to binarize!
108
109  IJ.run(filt, "Mean...", "radius=3_stack");
110  IJ.run("Auto_Threshold", "method=Li_ignore_black_ignore_white
        _white_stack_use_stack_histogram");
111  IJ.run(filt, "Dilate", "stack");
112  IJ.run(filt, "Fill_Holes", "stack");
113  IJ.run(filt, "Erode", "stack");
114  IJ.run(filt, "Open", "stack");
115
116  // save now binary image
117  ImagePlus bin = IJ.getImage();
118  ImageStack bstack = bin.getImageStack(); //save it as a
        stack
119
120  for (int j = 0; j<fsize; j++) { //store slices of the
        image stack as pgm images
121  ImageProcessor bimagep = bstack.getProcessor(j+1); //
        comment, slice number starts at 1
122  ImagePlus bimage = new ImagePlus("bimagep",bimagep);

```



```
123 final FileSaver binFile = new FileSaver(bimage);
124 final String bpathname = path + "/" + dirs[i]+ "/" +"Binary"
    + "/"+"Nucleus" + "/" + fimages[j];
125 binFile.saveAsPgm(bpathname);
126
127 }
128
129 filt.changes = false;
130 filt.close();
131
132 } // if folder == timepoint
133 } //loop for the timepoints
134 } //run
135 } // Plugin
```



## Appendix 2: Examples of Matlab Scripts

```
1 function [InterpolationErrors] = InterpolatePointsonTet (  
    Coord_t1, Displacements)  
2  
3 %load Coord_t1;  
4 %load Displacements;  
5  
6 %Coord_t1 = t1;  
7 %Displacements = titot2;  
8  
9 hits=0;  
10 SMesh=DelaunayTri(Coord_t1);  
11 tetramesh(SMesh, 'Facecolor', 'white', 'FaceAlpha', 0, 'EdgeColor'  
    ', 'black', 'EdgeAlpha', 0.01);  
12 hold on  
13 %plot3(Coord_t1(:,1), Coord_t1(:,2), Coord_t1(:,3), 'o', '  
    MarkerEdgeColor', [0.49 1 0.4], 'MarkerFaceColor', [0.49 1  
    0.4], 'MarkerSize', 6);  
14  
15 [PointsLoc, OutsidePoints]=InsidePoints(Coord_t1); %Returns  
    Logic Array, with point location: 1->Hull, 0-> Inside  
16  
17 InterpolationErrors=zeros(6, length(Coord_t1)-length(  
    OutsidePoints)); %OutsidePoints crows from "InsidePoints"  
    Function  
18 InsidePointsCoord=zeros(3, length(Coord_t1)-length(OutsidePoints  
    ));  
19  
20  
21  
22 i=1;  
23 for i=1:length(Coord_t1)  
24  
25     %Remove Point from Point cloud  
26  
27     if PointsLoc(i,1)==0  
28
```

---

```

29     %plot3 (Coord_t1(i,1),Coord_t1(i,2),Coord_t1(i,3), 'o', '
        MarkerEdgeColor', 'cyan', 'MarkerFaceColor', 'cyan', '
        MarkerSize', 6);
30     hits=hits+1;
31
32     if i<=1
33         NewCoor_t1=Coord_t1(2:end,:);
34
35         NewDisp=Displacements(2:end,:);
36
37     else
38         NewCoor_t1=[Coord_t1(1:i-1,:);Coord_t1(i+1:end,:)];
39
40         NewDisp=[Displacements(1:i-1,:);Displacements(i+1:
            end,:)];
41     end
42
43
44
45 % Generate new Tet mesh without Point
46
47     NewMesh=DelaunayTri(NewCoor_t1);
48     TetLocation=pointLocation(NewMesh,Coord_t1(i,:));
49
50     x1=NewCoor_t1(NewMesh.Triangulation(TetLocation,1),:);
51     x2=NewCoor_t1(NewMesh.Triangulation(TetLocation,2),:);
52     x3=NewCoor_t1(NewMesh.Triangulation(TetLocation,3),:);
53     x4=NewCoor_t1(NewMesh.Triangulation(TetLocation,4),:);
54
55     dx1=NewDisp(NewMesh.Triangulation(TetLocation,1),:);
56     dx2=NewDisp(NewMesh.Triangulation(TetLocation,2),:);
57     dx3=NewDisp(NewMesh.Triangulation(TetLocation,3),:);
58     dx4=NewDisp(NewMesh.Triangulation(TetLocation,4),:);
59
60     SubMeshPoints = [x1;x2;x3;x4];
61     SubMesh = DelaunayTri(SubMeshPoints);
62     SubMeshDis = [dx1;dx2;dx3;dx4];
63     Endpoints = SubMeshPoints+SubMeshDis;
64
65
66 %Jaccobi Matrix + Inverse + Determinant
67

```

```

68 JaccobiTet=CalculateJacobian (x1 , x2 , x3 , x4 );
69
70 invJaccobi=inv (JaccobiTet); %Out bc slow and inaccurate , V/
    Jaccobi instead
71
72 DetJaccobiTet=det (JaccobiTet );
73
74 %Compute "Shape Function" for point P. P = Coord_t1(i , :)
75
76 P = Coord_t1 (i , : );
77
78 V=P-x1;
79
80 V = [V(1);V(2);V(3)];
81
82 S=invJaccobi V; %Multiplies the Inverted Matrix , equals V inv
    (Jaccobi)
83
84 Intdp=dx1+(dx2-dx1) S (1)+(dx3-dx1) S (2)+(dx4-dx1) S (3);
85
86 %Calculate error on displacements differences
87
88 dp=Displacements (i , : );
89
90 d0=sqrt (dp (1)^2+dp (2)^2+dp (3)^2);
91
92 d=sqrt ((dp (1)-Intdp (1))^2+(dp (2)-Intdp (2))^2+(dp (3)-Intdp (3))
    ^2);
93
94 pEndpoint = P + dp;
95 pEndpointInt = P + Intdp;
96
97 InterpolationError=d 100/ d0;
98
99 InterpolationErrors (1 , hits)=i;
100 InterpolationErrors (2 , hits)=InterpolationError;
101 InterpolationErrors (3 , hits)=NewMesh. Triangulation (TetLocation
    ,1);
102 InterpolationErrors (4 , hits)=NewMesh. Triangulation (TetLocation
    ,2);
103 InterpolationErrors (5 , hits)=NewMesh. Triangulation (TetLocation
    ,3);

```

---

```

104 InterpolationErrors(6,hits)=NewMesh.Triangulation(TetLocation
      ,4);
105
106 InsidePointsCoord(1,hits)= P(1);
107 InsidePointsCoord(2,hits)= P(2);
108 InsidePointsCoord(3,hits)= P(3);
109
110 if InterpolationError >= 5
111     plot3(Coord_t1(i,1),Coord_t1(i,2),Coord_t1(i,3), 'o','
      MarkerEdgeColor',[0.9 0 0.16],'MarkerFaceColor',[0.9 0
      0.16],'MarkerSize',6);
112     plot3(SubMeshPoints(:,1),SubMeshPoints(:,2),SubMeshPoints
      (:,3),'o','MarkerFaceColor',[1 0.4 0],'MarkerEdgeColor
     ',[1 0.4 0],'MarkerSize',6);
113 end
114
115 end
116 end
117 %meanError = mean(InterpolationErrors(2,:))
118 InterpolationErrors
119 figure
120 bar(InterpolationErrors(1,:),InterpolationErrors(2,:),'r')

1 function [LinearStrainTensor, NonlinearTerms] =
      CalculateStrainTensor(DisGradient)
2
3 LinearStrainTensor = zeros(3);
4 NonlinearTerms = zeros(3);
5 dg = DisGradient;
6
7 %calculate linear terms
8
9 for i=1:3
10     for j=1:3
11         LinearStrainTensor(i,j) = 0.5 (dg(i,j)+dg(j,i));
12     end
13 end
14
15 %LinearStrainTensor(1,1) = 0.5 (dg(1,1) dg(1,1));
16 %LinearStrainTensor(1,2) = 0.5 (dg(1,2) dg(2,1));
17 %LinearStrainTensor(1,3) = 0.5 (dg(1,3) dg(3,1));
18

```

```

19
20 %Calculate nonlinear terms
21
22 %NonlinearTerms(1,1) = 0.5 (dg(1,1) dg(1,1)) + 0.5 (dg(2,1) dg
    (2,1)) 0.5 (dg(3,1) dg(3,1));
23 %NonlinearTerms(1,1) = 0.5 (dg(1,1) dg(1,1)) + 0.5 (dg(2,1) dg
    (2,1)) 0.5 (dg(3,1) dg(3,1));

1 function [Strain] = StrainforMesh(Coord_t1,Displacements)
2
3 TetMesh=DelaunayTri(Coord_t1);
4 figure
5 tetramesh(TetMesh, 'Facecolor', 'white', 'FaceAlpha',0.01, '
    EdgeColor', 'black', 'EdgeAlpha',0.01)
6 hold on
7
8 Strain = zeros(1,length(TetMesh(:,1)));
9
10 for i=1:length(TetMesh(:,1))
11
12     x1=Coord_t1(TetMesh.Triangulation(i,1),:);
13     x2=Coord_t1(TetMesh.Triangulation(i,2),:);
14     x3=Coord_t1(TetMesh.Triangulation(i,3),:);
15     x4=Coord_t1(TetMesh.Triangulation(i,4),:);
16
17     dx1=Displacements(TetMesh.Triangulation(i,1),:);
18     dx2=Displacements(TetMesh.Triangulation(i,2),:);
19     dx3=Displacements(TetMesh.Triangulation(i,3),:);
20     dx4=Displacements(TetMesh.Triangulation(i,4),:);
21
22     SubMeshPoints = [x1;x2;x3;x4];
23     SubMesh = DelaunayTri(SubMeshPoints);
24     SubMeshDis = [dx1;dx2;dx3;dx4];
25     Endpoints = SubMeshPoints+SubMeshDis;
26
27 Strain(i) = StrainTensor(SubMeshPoints,SubMeshDis);
28
29 end
30 figure
31     bar(Strain, 'FaceColor', 'k')
32     ylim([0 100])
33

```

---

```

34 end

1 function [Surface , SurfacePointsCoord , boundarydis] =
    MapStrainOnMesh(SCoordinates , SDisplacements , Mt1nodes ,
    Mt1face)
2
3 %%%% Make Tetraheder Mesh from beads point cloud = Substrate
    Mesh
4
5 Surface = Mt1face;
6
7 SMesh=DelaunayTri(SCoordinates);
8
9 SurfacePoints = unique(Mt1face);
10 SurfacePoints = SurfacePoints(2:end);
11 boundarydis = zeros(length(SurfacePoints) ,3);
12 SurfacePointsCoord = zeros(length(SurfacePoints) ,3);
13
14 tetramesh(SMesh, 'Facecolor', 'white', 'FaceAlpha',0, 'EdgeColor
    ', 'black', 'EdgeAlpha', 0.01)
15 hold on
16 plotmesh(Mt1nodes, Mt1face, 'Facecolor', 'white', 'FaceAlpha'
    ,0.01, 'EdgeColor', 'black', 'EdgeAlpha', 0.1 )
17
18 for i=1:length(SurfacePoints)
19     %i
20     P = Mt1nodes(SurfacePoints(i) ,:);
21     SurfacePointsCoord(i ,:) = P;
22
23     %%Find point in Substrate Tetreahedrons
24     Stet = pointLocation(SMesh,P);
25     Stetpoints = SCoordinates(SMesh.Triangulation(Stet ,1:4) ,:);
26     Stetdis = SDisplacements(SMesh.Triangulation(Stet ,1:4) ,:);
27
28     %%Calculate strain for Tetreahedron and assign it to point
29
30     boundarydis(i ,:) = InterpolateSinglePointInTet(P, Stetpoints
        , Stetdis);
31
32     %% Write out surface with new point coordinates
33
34 for j=1:length(Mt1face)

```



```
35     if Mt1face(j,1) == SurfacePoints(i)
36         Surface(j,1) = i;
37     end
38     if Mt1face(j,2) == SurfacePoints(i)
39         Surface(j,2) = i;
40     end
41     if Mt1face(j,3) == SurfacePoints(i)
42         Surface(j,3) = i;
43     end
44 end
45 %%%%%%%%%% Plot strain magnitude of substrate ON surface!
46
47 %SubMesh = DelaunayTri(Stetpoints);
48 StetStrain = boundarydis(i);
49
50 %% plotting [...]
51 end
```



# List of Figures

1.1	Forces in cellular biology . . . . .	2
1.2	Geometrical meaning and scales of relevant mechanical properties for biology . . . . .	5
1.3	Structures defining the mechanical properties of the cell . . . . .	9
1.4	Structural differences of cells cultured in 2D and 3D substrates . . .	15
2.1	Overview of methods . . . . .	28
2.2	Principle of image- and model-based framework for determination of nuclear compressibility . . . . .	39
2.3	Example tetrahedron for point interpolation. . . . .	41
3.1	Nuclear compressibility experimental workflow . . . . .	47
3.2	Influence of image gradients magnitude and orientation in the cal- culation of $\nu$ . . . . .	50
3.3	Testing the influence of image gradient geometry on the accuracy in the calculation of $\nu$ . . . . .	52
3.4	Bleaching patterns on fluorescently stained nuclei . . . . .	53
3.5	Nuclear compressibility in 3D . . . . .	54
3.6	Development of the substrate stretcher experimental setup . . . . .	56
3.7	Live cell imaging and stretching in 3D . . . . .	59
3.8	Stainings for live cell imaging at the 3D stretcher . . . . .	60
3.9	Volumetric surface reconstruction from cellular structures . . . . .	62
3.10	Detection and sorting of beads between adjacent time points . . . . .	64
3.11	Assessing local substrate homogeneity through interpolation of beads in substrate . . . . .	66
3.12	Example of heterogeneity in local strains . . . . .	67
3.13	Mapping substrate strain on cell surface . . . . .	68
3.14	Interpolation of cell and nucleus with substrate displacement . . . . .	69
3.15	Cellular and nuclear geometry of wild type and LMNA <sup>-/-</sup> cells and nuclei . . . . .	70
3.16	Nuclear compressibility of wild type and LMNA <sup>-/-</sup> nuclei . . . . .	72

3.17	Primary mouse hepatocytes in 2D and 3D substrates . . . . .	74
3.18	Morphology changes after TGF- $\beta$ treatment . . . . .	76
3.19	Changes in the pmHCs cytoskeleton organization after TGF- $\beta$ treatment . . . . .	78
3.20	Decrease of the compressibility of the nuclear interior after TGF- $\beta$	79
3.21	pmHCs on the 3D stretcher . . . . .	80

# List of Tables

1.1	Experimental methods to study cellular mechanical properties . . .	18
1.2	Experimental methods to study nuclear mechanical properties . . .	22
2.1	Plasmids used for cell transfection . . . . .	30
2.2	Overview of fluorophores used for confocal microscopy . . . . .	31
2.3	Materials, equipment, software . . . . .	43